Boundary conditions and applications of WENO finite difference schemes for hyperbolic problems

by

Sirui Tan

B.S., Tsinghua University, Beijing, P.R. China, 2007

M.S., Brown University, Providence, RI, 2009

A dissertation submitted in partial fulfillment of the
requirements for the degree of Doctor of Philosophy
in the Division of Applied Mathematics at Brown University

PROVIDENCE, RHODE ISLAND

May 2012

This dissertation by Sirui Tan is accepted in its present form
by the Division of Applied Mathematics as satisfying the
dissertation requirement for the degree of Doctor of Philosophy.

Date_____ _____

Chi-Wang Shu, Ph.D., Advisor

Recommended to the Graduate Council

Date_____ _____

Johnny Guzmán, Ph.D., Reader

Date_____ _____

Jan S. Hesthaven, Ph.D., Reader

Approved by the Graduate Council

Date_____ _____

Peter M. Weber, Dean of the Graduate School

Vitae

Biographical Information

Born on June 9, 1985 in Beijing, P.R. China

Education

Brown University
Ph.D. in Applied Mathematics, May 2012 (expected)
Dissertation Title: Boundary conditions and applications of WENO finite difference schemes for hyperbolic problems
Advisor: Chi-Wang Shu

Brown University
M.S. in Applied Mathematics, May 2009

Tsinghua University, Beijing, P.R. China
B.S. in Pure and Applied Mathematics, July 2007

Research Interests

- High order numerical methods for convection dominated problems, including WENO methods and discontinuous Galerkin methods
- Computational fluid dynamics
- Numerical methods for seismic wave simulation and seismic inversion
- Numerical methods for semiconductor device simulation

Research Experience

- Ph.D. Dissertation, Brown University, September 2008–present

  - Developed a numerical boundary condition for solving hyperbolic equations on Cartesian grids, while the physical domain can be arbitrarily shaped. It was applied to simulate interactions between compressible inviscid (inert or reactive) flows and rigid (static or moving) bodies with complex geometries. The method is stable, high order accurate, easy to implement, and capable of treating shock/detonation waves.
  - Modeled organic photovoltaic cells by adaptation of drift-diffusion models.

- Summer Internship, ExxonMobil Research and Engineering Company, June–September 2010 and June–August 2011
  - Worked on forward modeling of seismic waves in the Full Waveform Inversion Team in both summers.
  - Developed a hybrid finite-difference/finite element method for elastic waves.
  - Developed a high order accurate point source insertion for finite-difference modeling of seismic waves.
  - Investigated high order accurate free-surface boundary conditions for finite-difference modeling of elastic waves.

Publications

Publications in Refereed Journals

1. S. Tan, C. Wang, C.-W. Shu and J. Ning, Efficient implementation of high order inverse Lax-Wendroff boundary treatment for conservation laws, *Journal of Computational Physics*, 231 (2012), 2510–2527.

2. S. Tan and C.-W. Shu, A high order moving boundary treatment for compressible inviscid flows, *Journal of Computational Physics*, 230 (2011), 6023–6036.

3. S. Tan and C.-W. Shu, Inverse Lax-Wendroff procedure for numerical boundary conditions of conservation laws, *Journal of Computational Physics*, 229 (2010), 8144–8166.

Publications in Refereed Proceedings

1. S. Tan and C.-W. Shu, Inverse Lax-Wendroff procedure for numerical boundary conditions of hyperbolic equations: survey and new developments, submitted to *Fields Institute Communications Series Volume "Advances in Applied Mathematics, Mathematical Modeling and Computational Science"*.

2. J.W. Jerome, M.A. Ratner, J.D. Servaites, C.-W. Shu and S. Tan, Simulation of the Buxton-Clarke model for organic photovoltaic cells, in *Proceedings of the 14th International Workshop on Computational Electronics*, IWCE, 26–29 October, 2010, Pisa, Italy. Pisa University Press, 195–198.

Presentations

- "Inverse Lax-Wendroff procedure for numerical boundary conditions of hyperbolic equations", AMS-SIAM Special Session on Mathematics of Computation, Joint Mathematics Meetings, Boston, MA, January 4–7, 2012.
- "Inverse Lax-Wendroff procedure for numerical boundary conditions of conservation laws", The Seventh International Conference on Computational Physics, Beijing, China, May 17–20, 2010.
- "Inverse Lax-Wendroff type procedure for numerical boundary conditions of conservation laws", Applied Math Days, Rensselaer Polytechnic Institute, Troy, NY, March 19–20, 2010.

Honors and Awards

- University Research Assistantship, Brown University, 2009–present
- University Teaching Assistantship, Brown University, 2008
- University Fellowship, Brown University, 2007
- Outstanding Graduate (top 2%), Tsinghua University, 2007

Teaching Experience

Teaching Assistant, Brown University

- Methods of Applied Mathematics II, Spring 2009
- Methods of Applied Mathematics I, Fall 2008

Acknowledgements

I am heartily thankful to my academic advisor and mentor, Prof. Chi-Wang Shu, whose encouragement, guidance and support enabled me to develop an understanding of the subject, to think creatively and critically, to work under pressure, and finally to enjoy doing scientific research. I become a stronger, wiser, and happier person during my Ph.D. study because of him.

I am indebted to Prof. Jan Hesthaven and Prof. Johnny Guzmán for spending time serving on my dissertation committee and providing invaluable feedback. Moreover, I am grateful for their great classes and career advices.

It is an honor for me to work with Prof. Joseph Jerome, Dr. Jon Servaites and Brett Savoie on the modeling of organic solar cells. Without their knowledge and insights, the second part of the dissertation would not have been possible. My gratitude goes to Prof. Cheng Wang for collaboration on detonation problems, which greatly enriches the content of the dissertation.

I would like to thank my group members Dr. Xiangxiong Zhang, Dr. Yinhua Xia, Dr. Wei Wang, Dr. Yanlai Chen, Prof. Chunwu Wang, Dr. Wei Liu, Dr. Ishani Roy, Jacob Middag, and Xinghui Zhong for numerous discussions and helping me with computers.

I would like to show my gratitude to Dr. Martin-Daniel Lacasse, Dr. Laurent

White, Dr. Alex Kanevsky, Dr. Volkan Akcelik, Dr. Huseyin Denli, and Dr. Dimitar Trenev. I spent two wonderful summers with them at ExxonMobil Research and Engineering Company as an intern. They introduced me to seismic inversion and trained me for making effective presentations.

Words cannot express my love and gratitude to my parents, Dr. Baosheng Tan and Jian Guo, my wife Jiesi Zhang, and my parents-in-law, Dr. Boxu Zhang and He Liu. They support me in my triumphs and provide a shoulder when there are losses. They nurture my growth, yet allow me my independence. This dissertation would certainly not have existed without them.

Abstract of "Boundary conditions and applications of WENO finite difference schemes for hyperbolic problems" by Sirui Tan, Ph.D., Brown University, May 2012

This dissertation presents two topics concerning weighted essentially non-oscillatory (WENO) finite difference schemes for solving hyperbolic problems.

In the first part, we develop a high order accurate numerical boundary condition for solving hyperbolic problems on fixed Cartesian grids, while the physical domain can be arbitrarily shaped and moving. Compared with body-fitted meshes, the biggest advantage of Cartesian grids is that the grid generation is trivial. The challenge is however that the physical boundary does not usually coincide with grid lines. The wide stencil of WENO schemes makes a stable boundary treatment even harder to realize. There are two main ingredients of our method. The first one is an inverse Lax-Wendroff procedure for inflow boundary conditions and the other one is a robust and high order accurate extrapolation for outflow boundary conditions. Our method is high order accurate, stable under standard CFL conditions determined by the interior WENO schemes, and easy to implement. It has been successfully applied to simulate interactions between compressible inviscid flows and rigid (static or moving) bodies with complex geometries.

In the second part, we apply WENO finite difference schemes to solve the updated Buxton-Clarke model for organic photovoltaic cells. The model is represented by a system of convection-diffusion-reaction equations coupled to a Poisson's equation. The solution usually contains sharp gradients. WENO schemes successfully resolve the physical quantities on a relatively coarse mesh. The numerical simulations quantify the effect of material properties on device performance.

Contents

List of Tables

List of Figures

Chapter One

Introduction

Weighted essentially non-oscillatory (WENO) schemes have recently gained rapid popularity in numerical solutions of hyperbolic problems. WENO schemes are high order accurate schemes especially suitable for problems containing both strong discontinuities and complex smooth solution features. The essential idea lies at the approximation level, where a nonlinear adaptive procedure is used to automatically choose the locally smoothest stencil for reconstruction.

The first WENO scheme is introduced by Liu et al. [43], in which a third order accurate finite volume WENO scheme is developed. Jiang and Shu [33] provide a general framework to construct arbitrarily high order accurate finite difference WENO schemes, which are more efficient for multidimensional problems. We refer the reader to [59] for an extensive review of the algorithm design, analysis, implementation, and application of WENO schemes.

The main advantage of WENO schemes are their capability to achieve arbitrarily high order formal accuracy in smooth regions while maintaining stable, non-oscillatory, and sharp discontinuity transitions. Compared with the so-called high resolution schemes, represented by MUSCL schemes [67], TVD schemes [27], and PPM schemes [11], high order WENO schemes are more efficient for many application problems because of its high accuracy and resolution power [59].

In this dissertation, we present two topics concerning *finite difference* WENO schemes:

- High order accurate numerical boundary conditions for solving hyperbolic problems on Cartesian grids
- Simulation of the updated Buxton-Clarke model for organic photovoltaic cells

The first topic addresses the challenge of accurately imposing boundary conditions for problems involving complex static or moving geometries. For such problems, finite element type methods based on body-fitted meshes which conform to the geometries of physical domains are often used. However, mesh generation could be difficult for geometrically complicated domains in 3D and could also be very time-consuming for moving geometries in Eulerian approaches. Our boundary treatment is based on *fixed* Cartesian grids so that the grid generation is trivial. It is stable, high order accurate, easy to implement, and capable of treating shock waves and detonation waves. In the second topic, we apply finite difference WENO schemes to solve the updated Buxton-Clarke model for organic photovoltaic cells. The model is represented by a system of convection-diffusion-reaction equations coupled to a Poisson's equation. The solution usually contains sharp gradients, although it is continuous. WENO schemes successfully resolve the physical quantities on a relatively coarse mesh.

Chapter Two

Finite difference WENO schemes

In this chapter, we give a brief review of the fifth order accurate finite difference WENO scheme in the framework developed by Jiang and Shu [33]. See [59] for an extensive review. Generally speaking, WENO schemes are based on the method of lines. Namely, the partial differential equations (PDEs) are first discretized in space in a WENO fashion. The resulting ordinary differential equation (ODE) system is then solved by time discretization methods.

We first consider 1D scalar conservation laws. The numerical flux is obtained by a WENO reconstruction procedure. For systems of conservation laws, we do a local characteristic decomposition and use the flux evaluation techniques for the scalar equations. Generalizing the approximation to multiple space dimensions is straightforward for finite difference schemes. Finally, we discuss time discretization methods that are suitable for hyperbolic problems.

2.1 1D scalar conservation laws

We consider 1D scalar conservation laws in the form

$$u_t + f(u)_x = 0. \tag{2.1}$$

We use a uniform mesh $x_i = i\Delta x$ and the half points $x_{i+1/2} = (x_i + x_{i+1})/2$. A finite difference scheme approximates (2.1) in conservation form

$$\frac{d}{dt}u_i + \frac{1}{\Delta x}\left(\hat{f}_{i+1/2} - \hat{f}_{i-1/2}\right) = 0,$$

where the numerical flux

$$\hat{f}_{i+1/2} = \hat{f}(u_{i-p_1}, \ldots, u_{i+p_2})$$

is consistent with the physical flux $\hat{f}(u, \ldots, u) = f(u)$ and is Lipschitz continuous with respect to all its arguments. The scheme is fifth order accurate if

$$\frac{1}{\Delta x}\left(\hat{f}_{i+1/2} - \hat{f}_{i-1/2}\right) = f(u)_x\Big|_{x=x_i} + O(\Delta x^5), \tag{2.2}$$

when u is smooth in the stencil. The following lemma by Shu and Osher [61] establishes the relationship between reconstruction and finite difference approximation.

Lemma 2.1.1. *If $h(x) = h_{\Delta x}(x)$ is implicitly defined as*

$$\frac{1}{\Delta x}\int_{x-\Delta x/2}^{x+\Delta x/2} h(\xi)d\xi = f(u(x)), \tag{2.3}$$

then

$$\frac{1}{\Delta x}\left(h(x_{i+1/2}) - h(x_{i-1/2})\right) = f(u)_x\Big|_{x=x_i}.$$

This lemma implies that we can take the numerical flux as

$$\hat{f}_{i+1/2} = h(x_{i+1/2}) + O(\Delta x^5), \tag{2.4}$$

to ensure fifth order accuracy. Notice that the $O(\Delta x^5)$ term in (2.4) is usually smooth in practice, hence (2.2) holds. Due to the definition (2.3) of $h(x)$,

$$\bar{h}_i = \frac{1}{\Delta x}\int_{x_{i-1/2}}^{x_{i+1/2}} h(\xi)d\xi = f(u_i)$$

is known. Therefore, we are given the cell averages $\bar{h}_i$ of the function $h(x)$ and we

would like to approximate its point values $h(x_{i+1/2})$ to obtain the numerical flux $\hat{f}_{i+1/2}$. This is called reconstruction problem and is discussed in detail in the next section.

For the purpose of stability, the finite difference procedure described above is applied to $f^+(u)$ and $f^-(u)$ separately, where $f^\pm(u)$ are obtained by the Lax-Friedrichs flux splitting

$$f^\pm(u) = \frac{1}{2}\left(f(u) \pm \alpha u\right),$$

with

$$\alpha = \max_u |f'(u)|.$$

Notice that

$$\frac{d}{du} f^+(u) \geq 0, \quad \frac{d}{du} f^-(u) \leq 0$$

correspond to the right-going and left-going characteristics respectively. Therefore, the reconstruction for $f^+(u)$ should use a biased stencil with one more point to the left, and that for $f^-(u)$ should use a biased stencil with one more point to the right, to ensure correct upwinding.

2.2 WENO reconstruction

Assuming the cell averages $\bar{h}_i$ of a function $h(x)$ over the intervals $I_i = (x_{i-1/2}, x_{i+1/2})$ are known, we would like to find an approximation of $h(x)$ at the half points $x_{i+1/2}$. We can find a unique polynomial of degree at most two, denoted by $p_1(x)$, which reconstructs the function $h(x)$ over the stencil $S_1 = \{I_{i-2}, I_{i-1}, I_i\}$ in the sense that

$$(\bar{p}_1)_j = \frac{1}{\Delta x} \int_{x_{j-1/2}}^{x_{j+1/2}} p_1(x)dx = \bar{u}_j, \quad j = i-2,\, i-1,\, i.$$

Then $h^{(1)}_{i+1/2} \equiv p_1(x_{i+1/2})$ is a third order approximation to the value $h(x_{i+1/2})$ if the function $h(x)$ is smooth in the stencil S_1. An explicit formula is

$$h^{(1)}_{i+1/2} = \frac{1}{3}\bar{h}_{i-2} - \frac{7}{6}\bar{h}_{i-1} + \frac{11}{6}\bar{h}_i.$$

Similarly, we have different third order accurate approximations

$$h^{(2)}_{i+1/2} = p_2(x_{i+1/2}) = -\frac{1}{6}\bar{h}_{i-1} + \frac{5}{6}\bar{h}_i + \frac{1}{3}\bar{h}_{i+1},$$
$$h^{(3)}_{i+1/2} = p_3(x_{i+1/2}) = \frac{1}{3}\bar{h}_i + \frac{5}{6}\bar{h}_{i+1} - \frac{1}{6}\bar{h}_{i+2},$$

in stencil $S_2 = \{I_{i-1}, I_i, I_{i+1}\}$ and $S_3 = \{I_i, I_{i+1}, I_{i+2}\}$ respectively.

If we use the large stencil $S = \{I_{i-2}, I_{i-1}, I_i, I_{i+1}, I_{i+2}\} = S_1 \cup S_2 \cup S_3$, then we are able to obtain a fifth order accurate approximation

$$h_{i+1/2} = \frac{1}{30}\bar{h}_{i-2} - \frac{13}{60}\bar{h}_{i-1} + \frac{47}{60}\bar{h}_i + \frac{9}{20}\bar{h}_{i+1} - \frac{1}{20}\bar{h}_{i+2}.$$

An important observation is that the fifth order approximation $h_{i+1/2}$ can be written as a linear convex combination of the three third order approximations $h^{(1)}_{i+1/2}$, $h^{(2)}_{i+1/2}$, $h^{(3)}_{i+1/2}$. Namely,

$$h_{i+1/2} = \gamma_1 h^{(1)}_{i+1/2} + \gamma_2 h^{(2)}_{i+1/2} + \gamma_3 h^{(3)}_{i+1/2},$$

where the constants $\gamma_1 = 1/10$, $\gamma_2 = 3/5$, and $\gamma_3 = 3/10$ are called linear weights.

The WENO idea is to choose the final approximation as a convex combination of the three third order approximations $h^{(1)}_{i+1/2}$, $h^{(2)}_{i+1/2}$, $h^{(3)}_{i+1/2}$

$$h_{i+1/2} = \omega_1 h^{(1)}_{i+1/2} + \omega_2 h^{(2)}_{i+1/2} + \omega_3 h^{(3)}_{i+1/2}, \tag{2.5}$$

where ω_j are nonlinear weights. We would like to design the nonlinear weights such that

- $\omega_j = \gamma_j + O(\Delta x^2)$ for all j if $h(x)$ is smooth in the big stencil S;
- $\omega_j \approx 0$ if $h(x)$ has a discontinuity in the stencil S_j but is smooth in at least one of the other two stencils.

The first requirement ensures the fifth order accuracy of the WENO approximation $h_{i+1/2}$ if $h(x)$ is smooth in S. The second requirement guarantees a non-oscillatory and at least third order accurate WENO approximation $h_{i+1/2}$ given by (2.5) in the second case above.

According to Jiang and Shu [33], the nonlinear weights ω_j take the following form

$$\omega_j = \frac{\tilde{\omega}_j}{\tilde{\omega}_1 + \tilde{\omega}_2 + \tilde{\omega}_3}, \text{ with } \tilde{\omega}_j = \frac{\gamma_j}{(\varepsilon + \beta_j)^2}.$$

Here $\varepsilon = 10^{-6}$ is a small positive number to prevent the denominator vanishing. β_j are the so-called smoothness indicators defined as

$$\beta_j = \sum_{l=1}^{2} \Delta x^{2l-1} \int_{x_{i-1/2}}^{x_{i+1/2}} \left(\frac{d^l}{dx^l} p_j(x) \right)^2 dx.$$

The explicit formula is

$$\begin{aligned}
\beta_1 &= \frac{13}{12} \left(\bar{h}_{i-2} - 2\bar{h}_{i-1} + \bar{h}_i \right)^2 + \frac{1}{4} \left(\bar{h}_{i-2} - 4\bar{h}_{i-1} + 3\bar{h}_i \right)^2, \\
\beta_2 &= \frac{13}{12} \left(\bar{h}_{i-1} - 2\bar{h}_i + \bar{h}_{i+1} \right)^2 + \frac{1}{4} \left(\bar{h}_{i-1} - \bar{h}_{i+1} \right)^2, \\
\beta_3 &= \frac{13}{12} \left(\bar{h}_i - 2\bar{h}_{i+1} + \bar{h}_{i+2} \right)^2 + \frac{1}{4} \left(3\bar{h}_i - 4\bar{h}_{i+1} + \bar{h}_{i+2} \right)^2.
\end{aligned}$$

2.3 1D systems of conservation laws and multidimensional problems

We consider $m \times m$ hyperbolic systems

$$\mathbf{U}_t + \mathbf{F}(\mathbf{U})_x = 0. \tag{2.6}$$

The Jacobian matrix $\frac{\partial \mathbf{F}(\mathbf{U})}{\partial \mathbf{U}}$ has m real eigenvalues $\lambda_1 \leq \ldots \leq \lambda_m$ and a complete set of eigenvectors $\mathbf{r}_1, \ldots, \mathbf{r}_m$ which forms a right eigenmatrix $\mathbf{R} = (\mathbf{r}_1, \ldots, \mathbf{r}_m)$. Then clearly $\mathbf{R}^{-1}\frac{\partial \mathbf{F}(\mathbf{U})}{\partial \mathbf{U}}\mathbf{R} = \mathbf{\Lambda}$, where $\mathbf{\Lambda}$ is the diagonal matrix with $\lambda_1, \ldots, \lambda_m$ on the diagonal.

An easy way to solve (2.6) is to apply the WENO schemes in a component by component fashion. It is straightforward and cost effective. However, for some demanding test problems, there might be oscillations. We need the more costly, but much more robust characteristic decomposition. The idea can be illustrated by considering a simple example $\mathbf{F}(\mathbf{U}) = \mathbf{A}\mathbf{U}$ and $\mathbf{A}$ is a constant matrix. We define a characteristic variable $\mathbf{V} = \mathbf{R}^{-1}\mathbf{U}$. Then (2.6) is decoupled to m scalar equations

$$\frac{\partial \mathbf{V}}{\partial t} + \mathbf{\Lambda}\frac{\partial \mathbf{V}}{\partial x} = 0.$$

We can apply the WENO schemes to each scalar equation.

For general nonlinear systems, all the matrices involved are dependent on $\mathbf{U}$. We have to "freeze" them locally in order to carry out the characteristic decomposition. For Euler equations, the matrices are evaluated at the Roe average [52] $\mathbf{U}_{i+1/2}$

determined by the mean value property

$$\mathbf{F}(\mathbf{U}_{i+1}) - \mathbf{F}(\mathbf{U}_i) = \left.\frac{\partial \mathbf{F}(\mathbf{U})}{\partial \mathbf{U}}\right|_{\mathbf{U}=\mathbf{U}_{i+1/2}} (\mathbf{U}_{i+1} - \mathbf{U}_i).$$

We finally consider 2D hyperbolic systems

$$\mathbf{U}_t + \mathbf{F}(\mathbf{U})_x + \mathbf{G}(\mathbf{U})_y = 0.$$

The finite difference WENO schemes approximate the PDE in a dimension by dimension fashion

$$\frac{d}{dt}\mathbf{U}_{i,j}(t) = -\frac{1}{\Delta x}\left(\hat{\mathbf{F}}_{i+1/2,j} - \hat{\mathbf{F}}_{i-1/2,j}\right) - \frac{1}{\Delta y}\left(\hat{\mathbf{G}}_{i,j+1/2} - \hat{\mathbf{G}}_{i,j-1/2}\right). \tag{2.7}$$

The numerical flux $\hat{\mathbf{F}}_{i+1/2,j}$ can be computed from $\mathbf{U}_{i,j}$ with fixed j in exactly the same way as in the 1D case, and likewise for $\hat{\mathbf{G}}_{i,j+1/2}$.

2.4 Time discretization methods

The semi-discrete problem (2.7) can be discretized by an ODE solver. For hyperbolic problems with discontinuous solutions, it is important to maintain stability in the total variation seminorm of the first order forward Euler method with the same spatial discretization. A popular method satisfying such property is proposed by Shu and Osher [60]

$$\begin{aligned}
\mathbf{U}_{i,j}^{(1)} &= \mathbf{U}_{i,j}^{n} + \Delta t \mathcal{L}\left(\mathbf{U}_{i,j}^{n}\right), \\
\mathbf{U}_{i,j}^{(2)} &= \frac{3}{4}\mathbf{U}_{i,j}^{n} + \frac{1}{4}\mathbf{U}_{i,j}^{(1)} + \frac{1}{4}\Delta t \mathcal{L}\left(\mathbf{U}_{i,j}^{(1)}\right), \\
\end{aligned} \tag{2.8}$$

$$\mathbf{U}_{i,j}^{n+1} = \frac{1}{3}\mathbf{U}_{i,j}^{n} + \frac{2}{3}\mathbf{U}_{i,j}^{(2)} + \frac{2}{3}\Delta t\mathcal{L}\left(\mathbf{U}_{i,j}^{(2)}\right),$$

where $\mathcal{L}(\cdot)$ is the operator defined by the right-hand side of (2.7). It is the so-called third order total variation diminishing (TVD) Runge-Kutta (RK) method. More time discretization methods having this stability property can be found in [23, 58].

Chapter Three

Inverse Lax-Wendroff procedure for numerical boundary conditions

This chapter focuses on numerical boundary conditions for finite difference WENO schemes solving hyperbolic problems involving complex static or moving geometries. We assume the problems are posed on a finite domain so that no far field boundary condition is involved.

3.1 Introduction

For problems involving complex geometries, body-fitted meshes which conform to the geometry are often used due to the ease of imposing boundary conditions. In finite difference methods, body-fitted grids are usually generated by a curvilinear transformation that maps the physical domain to a computational domain. However, grid generation could be difficult for geometrically complicated domains and could also be very time-consuming for moving geometries in Eulerian approaches, since the grids have to be updated every few time steps. On the other hand, fixed Cartesian grids can be used to discretize the physical domain regardless of its geometry. The advantage is that the grid generation is trivial and the numerical schemes are usually more efficient than those on body-fitted grids. The biggest challenge with Cartesian grids is however to accurately impose the boundary conditions while retaining the stability under the standard CFL conditions determined by the interior schemes. The challenge mainly results from two facts. First, the physical boundary does not usually coincide with grid lines and can intersect the Cartesian grids in an arbitrary fashion. Secondly, a high order interior scheme, such as WENO scheme, needs a suitable treatment of *several* ghost points near the boundary because of its wide numerical stencil.

There are many successful numerical methods based on Cartesian grids. For

example, the immersed boundary method (IBM) introduced by Peskin [50] is widely used to solve incompressible flows in complicated time-varying geometries. See also [46] for an overview of the method and its applications. The IBM is extended for compressible viscous flows in [12, 13, 20]. An immersed interface method (IIM) is developed for elliptic equations in [40, 41] and for streamfunction-vorticity equations in [39]. We would like to emphasize that high order numerical boundary conditions for hyperbolic equations are somewhat more difficult than elliptic or convection-diffusion type equations mentioned above in the sense that there may be strong discontinuities near the boundaries. The boundary treatment should be robust for such cases when strong shock waves reflect off rigid boundaries.

The most popular way to impose boundary conditions at rigid boundaries for compressible flows is the reflection technique, where extra rows of ghost points are added. All interior solution components are reflected symmetrically to ghost states except for the normal velocity which is negated. This method works well when the rigid boundary is straight and positioned at half points. It might lead to large errors otherwise. The inaccuracy of the approach when applied to curved geometries is demonstrated by Moretti [47].

To solve hyperbolic equations in complex static or moving geometries with Cartesian grids, most methods in the literature are based on finite volume schemes. The difficulty mainly comes from the "small-cell" problem. Namely, one obtains irregular cut cells near the boundary, which may be orders of magnitude smaller than the regular grid cells, leading to a severe time step restriction. The so-called h-box method [5, 29] is developed to overcome this problem. The basic idea is to approximate numerical fluxes at the interface of a small cell based on initial values specified over regions of a regular length h. For one-dimensional advection equations, the h-box method is shown to be conservative and stable on arbitrary irregular grids

in [5]. Numerical results confirm the same conclusion for Euler equations in [29]. Another method to avoid the small-cell problem for Euler equations is to maintain cut boundary cells as whole (ghost) cells and obtain ghost cell values by reflecting locally the flow field around the boundary which is approximated by straight lines [17]. This method is stable and applicable to any finite volume method, but conservation at the boundary is violated although this error may be relatively small. For Euler equations involving moving geometries, an idea similar to [17] is developed in [16] but the ghost cell values are obtained by a mirror flow extrapolation. A cell merging technique combined with dimension splitting is developed by Falcovitz et al. [15]. Shyue [62] proposes a moving-boundary tracking algorithm based on finite volume wave-propagation method. The methods is stable even if there are very small cut cells near the tracked interface. Arienti et al. [2] develop an Eulerian-Lagrangian coupling scheme. Hu et al. [30] develop a conservative interface method based on the level set technique. In terms of accuracy, all the finite volume schemes mentioned above are at most second order. In particular, the errors at the boundaries sometimes fall short of second order, see numerical examples in [2, 17, 30].

For methods based on the finite difference formulation, a second order accurate Cartesian embedded boundary method is developed to solve the wave equations with Dirichlet or Neumann boundary conditions in [34, 35, 36] and to solve hyperbolic conservation laws in [63]. The basic idea is to assign values to ghost points *outside* the domain by using extrapolation. To avoid oscillations near shock waves, slope limiters are combined with extrapolation in [63]. The method in [63] is essentially based on a three point interior scheme so that only points just outside the boundary are ghost points. The feasibility and effectiveness to generalize this method to higher order remain to be demonstrated. Recently, Appelö and Petersson [1] modify the embedded boundary method in [34, 35, 36] by assigning values to boundary points

inside the domain via interpolation. This method is fourth order accurate and is based on a compact finite difference scheme.

A Lax-Wendroff type boundary condition procedure is introduced by Huang et al. [31] for solving static Hamilton-Jacobi equations with a third order finite difference method. It is extended to fifth order in [70] and to discontinuous Galerkin method in [71] for the same type of problems. The idea is to repeatedly use the partial differential equations (PDEs) to write the normal derivatives to the inflow boundary in terms of the tangential derivatives of the given boundary condition. With these normal derivatives, we can obtain accurate values of ghost points by a Taylor expansion from a point located on the boundary. In this chapter, we systematically extend this procedure to solve time dependent hyperbolic equations involving complex static or moving geometries with finite difference WENO schemes. For time dependent problems, the boundary treatment procedure is in essence repeatedly using the PDEs to convert normal spatial derivatives to time and tangential derivatives of the given boundary condition. It is in some sense an inverse to the standard Lax-Wendroff procedure [38], in which the PDEs are repeatedly used to convert time derivatives to spatial derivatives when discretizing the PDEs in time with high order accuracy. We therefore refer to our method as the inverse Lax-Wendroff procedure (ILW). This procedure is first proposed by Goldberg and Tadmor [21, 22] for analyzing numerical boundary conditions of linear hyperbolic equations in one dimension with boundaries aligned with grid lines. Lombard et al. [44] apply a similar idea to arbitrary-shaped free boundaries in finite difference schemes for linear elastic waves. Thus our work can also be regarded as an extension of [21, 22, 44] to nonlinear hyperbolic problems. In particular, strong discontinuities near the boundaries, which are absent in linear elastic waves, are handled by a high order WENO type extrapolation to prevent overshoot or undershoot. Moreover, we propose a simplified and improved imple-

mentation, which uses the relatively complicated ILW procedure only for the evaluation of the first order normal derivatives. High order WENO type extrapolation is used for all other derivatives, regardless of the direction of the local characteristics and the smoothness of the solution. This makes the implementation of a very high order boundary treatment practical for 2D nonlinear systems with source terms. For no-penetration boundary condition of compressible inviscid flows, a further simplification is discussed, in which the evaluation of the tangential derivatives involved in the ILW procedure is avoided.

This chapter is organized as follows. We first describe the initial-boundary-value problem of hyperbolic equations and the interior WENO schemes in Section 3.2. Then we briefly review the well-posedness theory of the problem in Section 3.3. It guides us in the design of stable numerical boundary conditions. Our boundary treatment technique for static geometries is developed in Section 3.4. We start with 1D scalar equations and proceed to 2D nonlinear systems. Extensive numerical examples are provided to demonstrate the performance of our high order boundary treatment. In Section 3.5, we consider compressible inviscid flows involving complex moving geometries. Concluding remarks, including future work, are given in Section 3.6.

3.2 Problem description and interior schemes

We consider hyperbolic conservation laws possibly with source terms for $\mathbf{U} = \mathbf{U}(x, y, t) \in \mathbb{R}^2$

$$\begin{cases} \mathbf{U}_t + \mathbf{F}(\mathbf{U})_x + \mathbf{G}(\mathbf{U})_y = \mathbf{S}(\mathbf{U}) & (x, y) \in \Omega(t), \quad t > 0, \\ \mathbf{U}(x, y, 0) = \mathbf{U}_0(x, y) & (x, y) \in \bar{\Omega}(t), \end{cases} \tag{3.1}$$

on a bounded domain $\Omega(t)$ with "appropriate" boundary conditions prescribed on $\Gamma(t) = \partial\Omega(t)$ at time t. The exact meaning of "appropriate" is explained in Section 3.3 for linear hyperbolic problems with constant coefficients.

We assume we always have an analytical expression for the geometry of $\Gamma(t)$. $\Omega(t)$ is covered by a uniform Cartesian mesh with mesh size $\Delta x = \Delta y = h$, but the boundary $\Gamma(t)$ does not need to coincide with any grid lines. The semi-discrete approximation of (3.1) is given by

$$\begin{aligned} \frac{d}{dt}\mathbf{U}_{i,j}(t) = &-\frac{1}{h}\left(\hat{\mathbf{F}}_{i+1/2,j} - \hat{\mathbf{F}}_{i-1/2,j}\right) \\ &-\frac{1}{h}\left(\hat{\mathbf{G}}_{i,j+1/2} - \hat{\mathbf{G}}_{i,j-1/2}\right) + \mathbf{S}\left(\mathbf{U}_{i,j}(t)\right), \end{aligned} \tag{3.2}$$

where $\hat{\mathbf{F}}_{i+1/2,j}$ and $\hat{\mathbf{G}}_{i,j+1/2}$ are the numerical fluxes. We use the third order TVD RK method (2.8) to integrate the system of ordinary differential equations (3.2) in time.

Special care must be taken when we impose a *time dependent* boundary condition $\mathbf{g}(t)$ in the two intermediate stages of the RK method (2.8). Numerical experiments show that the traditional match of time

$$\begin{aligned} \mathbf{U}^n &\sim \mathbf{g}(t_n), \\ \mathbf{U}^{(1)} &\sim \mathbf{g}(t_{n+1}), \\ \mathbf{U}^{(2)} &\sim \mathbf{g}(t_n + \Delta t/2), \end{aligned}$$

decreases the accuracy of our boundary treatment to second order. Following the idea in [9], we can easily show that for the hyperbolic equations (3.1) with source terms the following match of time levels at the boundary maintains the third order

accuracy of (2.8)

$$\begin{aligned} \mathbf{U}^n &\sim \mathbf{g}(t_n), \\ \mathbf{U}^{(1)} &\sim \mathbf{g}(t_n) + \Delta t \mathbf{g}'(t_n), \\ \mathbf{U}^{(2)} &\sim \mathbf{g}(t_n) + \frac{1}{2}\Delta t \mathbf{g}'(t_n) + \frac{1}{4}\Delta t^2 \mathbf{g}''(t_n). \end{aligned} \tag{3.3}$$

For simplicity, we denote the boundary conditions for all three stages at time level $t = t_n$ by $\mathbf{g}(t_n)$, although $\mathbf{g}(t_n)$ is actually different for each stage according to (3.3).

We use the fifth order finite difference WENO scheme with the Lax-Friedrichs flux splitting to form the numerical fluxes $\hat{\mathbf{F}}_{i+1/2,j}$ and $\hat{\mathbf{G}}_{i,j+1/2}$ in (3.2). The scheme requires a seven point stencil in both x and y directions. Near $\Gamma(t)$ where the numerical stencil is partially outside of $\Omega(t)$, up to three ghost points are needed in each direction. In some cases of moving boundaries, up to four ghost points may be needed in each direction. We concentrate on how to define the values of the ghost points at time level $t = t_n$ in Section 3.4 and Section 3.5 for static and moving geometries respectively.

3.3 Well-posedness of initial-boundary-value (IBV) problems

To explain what are the "appropriate" boundary conditions mentioned for the hyperbolic equations (3.1), we briefly review the well-posedness theory of IBV problems for linear hyperbolic equations with constant coefficients. We refer the reader to Chapter 9 and 10 of [25] for detailed discussions, including proofs of the theorem. The well-posedness theory would give us a lot of insight into the design of *stable*

numerical boundary conditions.

3.3.1 Characteristics and boundary conditions for 1D hyperbolic systems

We start with the scalar wave equation

$$u_t + a u_x = 0, \tag{3.4}$$

in the domain $0 \le x \le 1$, $t \ge 0$. Here a is a constant. At $t = 0$, we have the initial data

$$u(x, 0) = f(x).$$

In general, we need to specify boundary condition to solve for $u(x, t)$ on $0 \le x \le 1$, $t \ge 0$. The question is to determine what type of boundary conditions should we specify so that the IBV problem is well-posed.

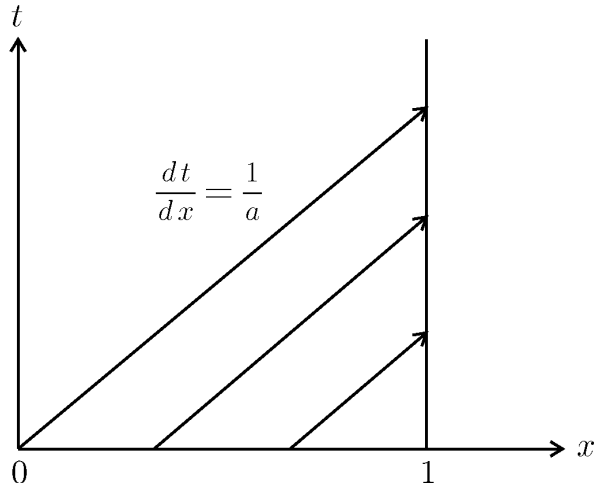

Figure 3.1: Characteristics of the equation (3.4) for $a > 0$.

We consider the characteristics along which the solution is a constant. If $a > 0$,

then the characteristic goes from left to right, see Figure 3.1. We thus need to specify a boundary condition at the left boundary $x = 0$

$$u(0, t) = g(t).$$

At the right boundary, the solution may uniquely be determined by the initial data. As a result, no boundary condition is necessary. Similarly, if $a < 0$, we need to specify a boundary condition at the right boundary $x = 1$. If $a = 0$, we do not need any boundary condition because $u_t \equiv 0$ implies $u(x, t) \equiv f(x)$.

The idea of characteristics can be extended to strongly hyperbolic system with constant coefficients

$$\frac{\partial \mathbf{U}}{\partial t} + \mathbf{A}\frac{\partial \mathbf{U}}{\partial x} = 0, \quad 0 \le x \le 1, \quad t \ge 0, \tag{3.5}$$

where $\mathbf{U} \in \mathbb{R}^m$ and $\mathbf{A}$ is a $m \times m$ matrix. We do the characteristic decomposition as we did in Section 2.3. Let $\mathbf{R}$ be the right eigenmatrix of $\mathbf{A}$. Then

$$\mathbf{R}^{-1}\mathbf{A}\mathbf{R} = \mathbf{\Lambda} = \begin{pmatrix} \mathbf{\Lambda}^I & & \\ & \mathbf{\Lambda}^{II} & \\ & & \mathbf{\Lambda}^{III} \end{pmatrix},$$

where

$$\mathbf{\Lambda}^I = \begin{pmatrix} \lambda_1 & & & \\ & \lambda_2 & & \\ & & \ddots & \\ & & & \lambda_r \end{pmatrix} < 0,$$

$$\mathbf{\Lambda}^{II} = \begin{pmatrix} \lambda_{r+1} & & & \\ & \lambda_{r+2} & & \\ & & \ddots & \\ & & & \lambda_{m-s} \end{pmatrix} > 0, \quad \mathbf{\Lambda}^{III} = 0$$

are diagonal matrices.

Under the transformation induced by $\mathbf{R}$, we obtain the equivalent system

$$\frac{\partial}{\partial t} \begin{pmatrix} \mathbf{V}^I \\ \mathbf{V}^{II} \\ \mathbf{V}^{III} \end{pmatrix} + \begin{pmatrix} \mathbf{\Lambda}^I & & \\ & \mathbf{\Lambda}^{II} & \\ & & \mathbf{\Lambda}^{III} \end{pmatrix} \frac{\partial}{\partial x} \begin{pmatrix} \mathbf{V}^I \\ \mathbf{V}^{II} \\ \mathbf{V}^{III} \end{pmatrix} = 0,$$

where the characteristic variable

$$\mathbf{V} = \begin{pmatrix} \mathbf{V}^I \\ \mathbf{V}^{II} \\ \mathbf{V}^{III} \end{pmatrix} = \mathbf{R}\mathbf{U}.$$

Now the hyperbolic system is decoupled into independent scalar equations. Using the previous argument, we need to specify boundary conditions

$$\mathbf{V}^I(1,t) = \mathbf{g}^I(t), \quad \mathbf{V}^{II}(0,t) = \mathbf{g}^{II}(t).$$

We can generalize the boundary condition to

$$\mathbf{V}^I(1,t) = \mathbf{R}^{II}\mathbf{V}^{II}(1,t) + \mathbf{g}^I(t),$$
$$\mathbf{V}^{II}(0,t) = \mathbf{R}^I\mathbf{V}^I(0,t) + \mathbf{g}^{II}(t),$$

where $\mathbf{R}^I$ and $\mathbf{R}^{II}$ are rectangular matrices that may depend on t.

An important observation is that the number of boundary conditions at the left boundary $x = 0$ is equal to $m - s - r$, the number of positive eigenvalues of $\mathbf{\Lambda}$, or, equivalently, the number of characteristics entering the domain. At the right boundary $x = 1$, the number of boundary conditions is equal to r, the number of negative eigenvalues of $\mathbf{\Lambda}$. No boundary condition corresponds to zero eigenvalues.

Back to the original variable $\mathbf{U}$, the boundary conditions are in general

$$\mathbf{L}_0\mathbf{U}(0,t) = \mathbf{g}_0(t), \tag{3.6}$$

$$\mathbf{L}_1\mathbf{U}(1,t) = \mathbf{g}_1(t), \tag{3.7}$$

where $\mathbf{L}_0$ is a $(m-s-r) \times m$ matrix with rank $m-s-r$ and $\mathbf{L}_1$ is a $r \times m$ matrix with rank r.

3.3.2 Well-posedness of 1D hyperbolic systems

With the help of characteristics, we have determined the type of boundary conditions should we specify. The following theorem states that the resulting IBV problem is strongly well-posed. It is proved by the energy method, which can be found in Chapter 9 of [25].

Theorem 3.3.1. *For 1D hyperbolic systems* (3.5) *with boundary conditions* (3.6) *and* (3.7)*, the IBV problem is strongly well-posed.*

3.3.3 Multidimensional hyperbolic systems

The analysis of the well-posedness of multidimensional hyperbolic systems involves Laplace transform techniques [25] and is omitted here. We would like to emphasize that a naive generalization of Theorem 3.3.1 to multiple space dimensions does *not* hold. An interesting counterexample from [25] is

$$\mathbf{U}_t + \begin{pmatrix} 1 & 0 \\ 0 & -1 \end{pmatrix} \mathbf{U}_x + \begin{pmatrix} 0 & -1 \\ -1 & 0 \end{pmatrix} \mathbf{U}_y = 0, \quad 0 \leq x < +\infty, \quad -\infty < y < +\infty,$$

where $\mathbf{U} = \begin{pmatrix} U_1 \\ U_2 \end{pmatrix}$ has two components. We consider the boundary condition at $x = 0$. The 1D theory implies that the boundary condition should be of the form

$$U_1(0, y, t) = \alpha U_2(0, y, t) + g(y, t),$$

where α is a constant. However, the IBV problem is strongly well-posed if and only if $|\alpha| \leq 1$. In other words, for 2D systems we *cannot* determine the well-posedness of the IBV problem only by the signs of the eigenvalues.

3.4 Numerical boundary conditions for static geometries

3.4.1 1D scalar conservation laws: smooth solutions

To illustrate the essential idea of the ILW procedure, we use 1D scalar conservation laws as an example

$$\begin{cases} u_t + f(u)_x = 0 & x \in (-1,1), \quad t > 0, \\ u(-1,t) = g(t) & t > 0, \\ u(x,0) = u_0(x) & x \in [-1,1]. \end{cases}$$

We assume $f'(u(-1,t)) \geq \alpha > 0$ and $f'(u(1,t)) \geq \alpha > 0$ for $t > 0$. This assumption guarantees the left boundary $x = -1$ is an inflow boundary where a boundary condition is needed and the right boundary $x = 1$ is an outflow boundary where no boundary condition is needed.

Let us discretize the interval $(-1,1)$ by a uniform mesh

$$-1 + h/2 = x_0 < x_1 < \ldots < x_N = 1 - h/2.$$

Notice that both x_0 and x_N are not located on the boundary, which is chosen this way on purpose since it is usually impossible to align boundary with grid points in a 2D domain with complex geometry. We assume $u_0, \ldots, u_N$ have been updated from time level t_{n-1} to time level t_n. Here we suppress the t_n dependence without causing any confusion.

The ILW procedure for inflow boundary conditions

At the inflow boundary $x = -1$, we construct a sth order approximation of ghost point values $u_{-3}, \ldots, u_{-1}$ by a Taylor expansion

$$u_j = \sum_{k=0}^{s-1} \frac{(x_j + 1)^k}{k!} u_L^{*(k)}, \quad j = -3, \ldots, -1, \tag{3.8}$$

where $u_L^{*(k)}$ is a $(s-k)$th order approximation of $\frac{\partial^k u}{\partial x^k}\Big|_{x=-1,\ t=t_n}$. We impose $u_L^{*(0)} = g(t_n)$. To obtain the approximation of the spatial derivative $\frac{\partial u}{\partial x}\big|_{x=-1,\ t=t_n}$, we utilize the PDE

$$u_t + f'(u)u_x = 0$$

and evaluate it at $x = -1$, $t = t_n$. We impose

$$\begin{aligned} u_L^{*(1)} &= -\frac{u_t(-1, t_n)}{f'(u(-1, t_n))} \\ &= -\frac{g'(t_n)}{f'(g(t_n))}, \end{aligned}$$

where $f'(g(t_n))$ is bounded away from zero by the assumption that $x = -1$ is an inflow boundary. Differentiating the PDE with respect to time yields

$$u_{tt} + f''(u)u_t u_x + f'(u)u_{xt} = 0. \tag{3.9}$$

The term u_{xt} can be written as

$$\begin{aligned} u_{xt} &= (u_t)_x \\ &= -(f'(u)u_x)_x \\ &= -f''(u)u_x^2 - f'(u)u_{xx}. \end{aligned}$$

Substituting it into (3.9), we obtain an equation for u_{xx}

$$u_{tt} + f''(u)u_t u_x - f'(u)f''(u)u_x^2 - f'(u)^2 u_{xx} = 0. \tag{3.10}$$

Solving (3.10) for u_{xx} and evaluating it at $x = -1$, $t = t_n$, we impose

$$\begin{aligned} u_L^{*(2)} &= \frac{g''(t_n) + f''(g(t_n))g'(t_n)u_x(-1,t_n) - f'(g(t_n))f''(g(t_n))u_x^2(-1,t_n)}{f'(g(t_n))^2} \\ &= \frac{f'(g(t_n))g''(t_n) - 2f''(g(t_n))g'(t_n)^2}{f'(g(t_n))^3}. \end{aligned}$$

Following the same procedure, we can impose values of $u_L^{*(k)}$, $k = 1, \ldots, s-1$.

The idea of converting time derivatives to spatial derivatives by repeatedly using the PDE comes from the original Lax-Wendroff scheme [38]. Since we convert spatial derivatives to time derivatives, our method is called *inverse* Lax-Wendroff procedure. We remark that this procedure is independent of the location of the boundary. The time derivatives can be obtained by either using the analytical derivatives of $g(t)$ if available or numerical differentiation. In the case of discontinuities going through the boundary, $g(t)$ is discontinuous. The stencil used for numerical differentiation should not contain any discontinuity. For example, an essentially non-oscillatory (ENO) procedure [28] or a WENO procedure [33] can be used for this numerical differentiation.

Lagrange extrapolation for outflow boundary conditions

At the outflow boundary $x = 1$, values of ghost points $u_{N+1}, \ldots, u_{N+3}$ are also approximated by a $(s-1)$th order Taylor expansion

$$u_j = \sum_{k=0}^{s-1} \frac{(x_j - 1)^k}{k!} u_R^{*(k)}, \quad j = N+1, \ldots, N+3,$$

where $u_R^{*(k)}$ is a $(s-k)$th order approximation of $\left.\frac{\partial^k u}{\partial x^k}\right|_{x=1,\ t=t_n}$. At the outflow boundary, $u_R^{*(k)}$ should be imposed by the values of the interior points, $u_0, \ldots, u_N$, because of the outgoing characteristics, even if a boundary condition is improperly prescribed. If $u(x)$ is smooth near the boundary, $u_R^{*(k)}$ can be easily obtained by

$$u_R^{*(k)} = \left.\frac{d^k p_{s-1}(x)}{dx^k}\right|_{x=1},$$

where $p_{s-1}(x)$ is a Lagrange polynomial of degree at most $s-1$ interpolating u_j, $j = N-s+1, \ldots, N$. An explicit formula for the values of ghost points is

$$\sum_{k=0}^{s} \frac{s!}{k!(s-k)!} (-1)^k u_{j-k} = 0, \quad j = N+1, \ldots, N+3. \tag{3.11}$$

For example, for $s = 5$

$$u_j = u_{j-5} - 5u_{j-4} + 10u_{j-3} - 10u_{j-2} + 5u_{j-1}, \quad j = N+1, \ldots, N+3.$$

Linear stability

The linear stability of the numerical boundary conditions with arbitrary order of accuracy described above has been proved by Goldberg and Tadmor [22] by using

the theory of Gustafsson, Kreiss, and Sundström [26] (henceforth GKS). Goldberg and Tadmor [22] also show that the time step restriction of solving the IBV problem with the boundary treatment is not more severe than the pure initial value problem, regardless of the location of the boundary.

A numerical example

Example 3.4.1. We test the Burgers equation

$$\begin{cases} u_t + \left(\frac{1}{2}u^2\right)_x = 0 & x \in (-1,1), \quad t > 0, \\ u(x,0) = 0.25 + 0.5\sin(\pi x) & x \in [-1,1], \\ u(-1,t) = g(t) & t > 0. \end{cases} \tag{3.12}$$

The boundary condition $g(t)$ is taken from the exact solution of the initial value problem on $(-1,1)$ with periodic boundary conditions. For all t, the left boundary $x = -1$ is an inflow boundary and the right boundary $x = 1$ is an outflow boundary. At $t = 0.3$, we have a smooth solution. We test our fifth order boundary treatment, i.e., $s = 5$. The errors are listed in Table 3.1. We achieve the designed fifth order accuracy.

Table 3.1: Errors of the Burgers equation (3.12). $\Delta t = O(h^{5/3})$ and $t = 0.3$. The outflow boundary condition is imposed by Lagrange extrapolation.

h	L^1 error	order	L^∞ error	order
1/40	3.10E-06		1.35E-05	
1/80	1.31E-07	4.57	6.51E-07	4.38
1/160	3.97E-09	5.05	2.68E-08	4.60
1/320	1.02E-10	5.29	8.34E-10	5.00
1/640	2.86E-12	5.15	2.62E-11	5.00
1/1280	1.04E-13	4.78	9.09E-13	4.85

3.4.2 1D scalar conservation laws: solutions containing discontinuities

We continue Example 3.4.1. At a later time $t = 1.1$, a shock is fully developed in the interior of the computational domain. A shock enters the inflow boundary at $t = 8$ and moves to $x = 0$ at $t = 12$. We can see from Figure 3.2 that the shock is well captured in both scenarios by our method. This example and later examples when shocks come from the boundary indicate that, even though the ILW procedure is based on the assumption of smoothness of the boundary data, its application to discontinuous but piecewise smooth boundary data coupled with a non-oscillatory internal scheme does not lead to spurious oscillations or instability.

Next we investigate the case that a shock is very close to the outflow boundary. Figure 3.3 shows the solutions at $t = 7.8$. We can clearly see that there is severe undershoot near the outflow boundary. This is not surprising because of the Gibbs phenomenon. In this situation, we prefer a possibly lower order accurate but more robust extrapolation. The fifth order WENO type extrapolation is developed for this purpose.

Fifth order WENO type extrapolation for outflow boundary conditions

We need to obtain $u_R^{*(k)}$, a $(5-k)$th order approximation of the kth order derivative of $u(x)$ at the boundary, using the grid point values in the interior of the domain u_j, $j = N-4, \ldots, N$. We consider the stencil $S_4 = \{x_{N-4}, \ldots, x_N\}$ as five candidate substencils $S_r = \{x_{N-r}, \ldots, x_N\}$, $r = 0, \ldots, 4$. On each substencil, we can easily construct a Lagrange polynomial $p_r(x)$ of degree at most r such that $p_r(x_j) = u_j$,

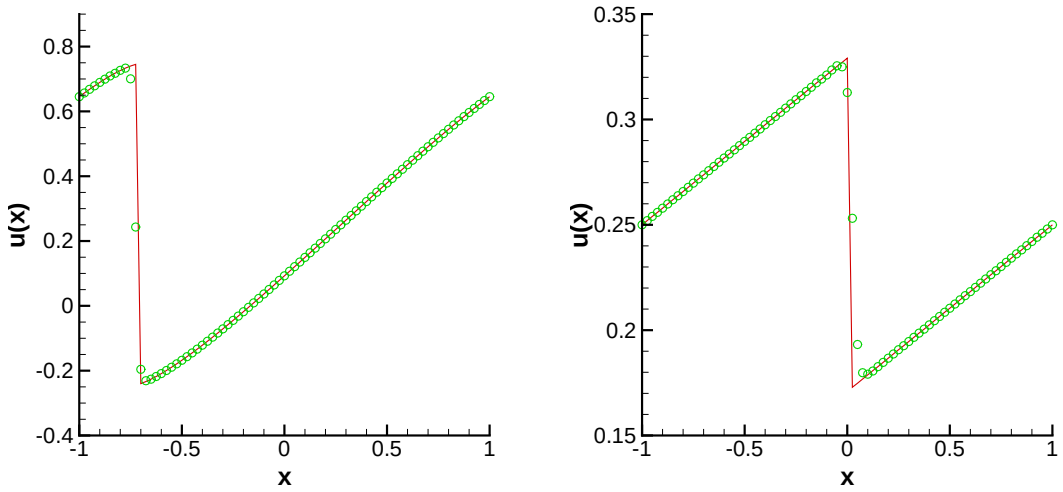

(a) $t = 1.1$ (b) $t = 12$

Figure 3.2: Burgers equation (3.12). $h = 1/40$ and CFL $= 0.6$. Solid line: exact solution; Symbols: numerical solution.

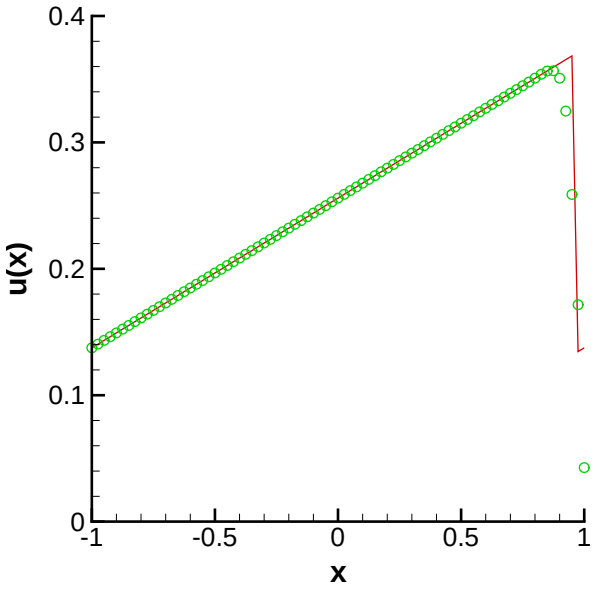

Figure 3.3: Burgers equation (3.12). $h = 1/40$, CFL $= 0.6$, and $t = 7.8$. The outflow boundary condition is imposed by Lagrange extrapolation. Solid line: exact solution; Symbols: numerical solution.

$j = N - r, \ldots, N$. Suppose u is smooth on S_4, $u_R^{*(k)}$ can be extrapolated by

$$u_R^{*(k)} = \sum_{r=0}^{4} \gamma_r \frac{d^k p_r(x)}{dx^k}\bigg|_{x=1},$$

where $\gamma_0 = h^4$, $\gamma_1 = h^3$, $\gamma_2 = h^2$, $\gamma_3 = h$, and $\gamma_4 = 1 - \sum_{r=0}^{3} \gamma_r$.

Borrowing the idea of WENO reconstruction discussed in Section 2.2, we look for WENO type extrapolation in the form

$$u_R^{*(k)} = \sum_{r=0}^{4} \omega_r \frac{d^k p_r(x)}{dx^k}\bigg|_{x=1}, \tag{3.13}$$

where ω_r are the nonlinear weights depending on the value of u_j. In the case that u is smooth in S_4, we would like to have

$$\omega_0 = O(h^4),\ \omega_1 = O(h^3),\ \omega_2 = O(h^2),\ \omega_3 = O(h) \text{ and } \omega_4 = 1 - \sum_{r=0}^{3} \omega_r \tag{3.14}$$

such that (3.13) is $(5-k)$th order accurate. The nonlinear weights ω_r are defined by

$$\omega_r = \frac{\tilde{\omega}_r}{\sum_{\nu=0}^{4} \tilde{\omega}_\nu}$$

with

$$\tilde{\omega}_r = \frac{\gamma_r}{(\varepsilon + \beta_r)^q}, \tag{3.15}$$

where $\varepsilon = 10^{-6}$, $q \geq 3$ is an integer, and β_r are the smoothness indicators determined by

$$\begin{aligned}
&\beta_0 = h^2, \\
&\beta_r = \sum_{l=1}^{r} \int_1^{1+h} h^{2l-1} \left(\frac{d^l}{dx^l} p_r(x) \right)^2 dx, \quad r = 1, \ldots, 4.
\end{aligned}$$

The explicit expressions for the smoothness indicators β_1 and β_2 are

$$\beta_1 = (u_{N-1} - u_N)^2,$$
$$\beta_2 = (61u_N^2 + 160u_{N-1}^2 + 74u_N u_{N-2} + 25u_{N-2}^2 - 196u_{N-1}u_N + 124u_{N-1}u_{N-2})/12.$$

The expressions for β_3 and β_4 are tedious but can be easily derived by symbolic computation softwares. The constant integer q is taken as $q = 3$ in all our 1D examples.

We can show that (3.14) holds if u is smooth in S_4. If S_r, $r \geq 1$, contains a discontinuity but S_{r-1} does not, we have $\omega_\nu = O(h^{r-1-\nu})$, $\nu = 0, \ldots, r-1$, and $\omega_\nu = O(h^{2q+r-1-\nu})$, $\nu = r, \ldots, 4$. Namely, $u_R^{*(0)}$ reduces to a rth order approximation and as $h \to 0$ the weights assigned to the non-smooth substencils $S_r, \ldots, S_4$ vanish. The proof is similar to that in Section 2 of [33] and is omitted here.

The undershoot is well-controlled by this more robust extrapolation, see Figure 3.4. Moreover, the fifth order accuracy of smooth solutions is maintained. The errors at $t = 0.3$ are almost the same as those in Table 3.1. Therefore, we use the more robust WENO type extrapolation from now on, regardless of the smoothness of the solution.

3.4.3 1D scalar conservation laws: efficient implementation

We recall that the spatial derivatives $u_L^{*(k)}$, $k \geq 1$, in the Taylor expansion (3.8) are obtained by repeated use of the PDE at the inflow boundary. Obviously, the algebra of converting derivatives of order higher than or equal to two can be very heavy if the PDE is complicated, which is usually the case if we consider 2D fully nonlinear

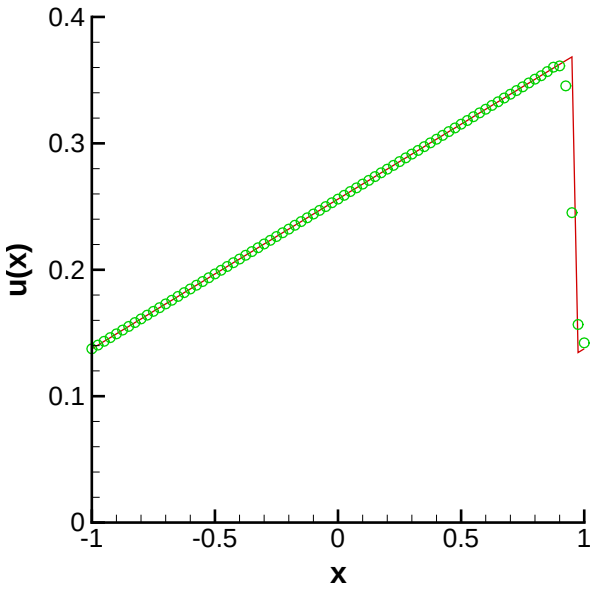

Figure 3.4: Burgers equation (3.12). $h = 1/40$, CFL $= 0.6$, and $t = 7.8$. The outflow boundary condition is imposed by WENO extrapolation. Solid line: exact solution; Symbols: numerical solution.

systems (3.1). The complicated algebra would prevent us from implementing higher than third order accurate boundary treatment for 2D Euler equations [64, 65], although our method is designed to achieve arbitrarily high order accuracy for general equations with source terms.

We investigate each term in the Taylor expansion (3.8) and find that only $u_L^{*(1)}$ is crucial to be implemented by the ILW procedure to ensure stability. In other words, $u_L^{*(k)}$, $k = 2, 3, 4$, can be simply obtained by extrapolation. This simplified algorithm significantly alleviates the complicated algebra in the ILW procedure, especially for 2D systems with source terms. A similar idea is proposed by Qiu and Shu for the Lax-Wendroff time discretization [51], in which they perform a WENO approximation only for the reconstruction of the fluxes to the first order time derivative to avoid spurious oscillations and use the inexpensive central difference approximation for the reconstruction of the higher order time derivatives. Notice that instability is observed

in our numerical experiments if the first order spatial derivative $u_L^{*(1)}$ is also obtained by extrapolation. Therefore, the ILW procedure is crucial to ensure stability. We finally remark that we observe no instability in our numerical experiments if the standard CFL conditions determined by the interior WENO schemes are used for the simplified algorithm.

We redo Example 3.4.1 with this efficient implementation, together with WENO type extrapolation. The errors in Table 3.2 are similar to those in Table 3.1. The shock profiles are also similar, see Figure 3.5. Therefore, we focus on the efficient implementation with WENO type extrapolation and extend it to solve systems of hyperbolic equations.

Table 3.2: Errors of the Burgers equation (3.12) solved by the efficient implementation. $\Delta t = O(h^{5/3})$ and $t = 0.3$.

h	L^1 error	order	L^∞ error	order
1/40	4.73E-06		5.88E-05	
1/80	1.46E-07	5.02	1.58E-06	5.21
1/160	3.48E-09	5.39	2.68E-08	5.89
1/320	7.56E-11	5.53	3.62E-10	6.21
1/640	1.89E-12	5.32	1.97E-11	4.20
1/1280	7.01E-14	4.76	8.00E-13	4.62

3.4.4 1D Euler equations

We consider 1D compressible Euler equations without a source term

$$\mathbf{U}_t + \mathbf{F}(\mathbf{U})_x = 0, \quad x \in (-1, 1), \quad t > 0,$$

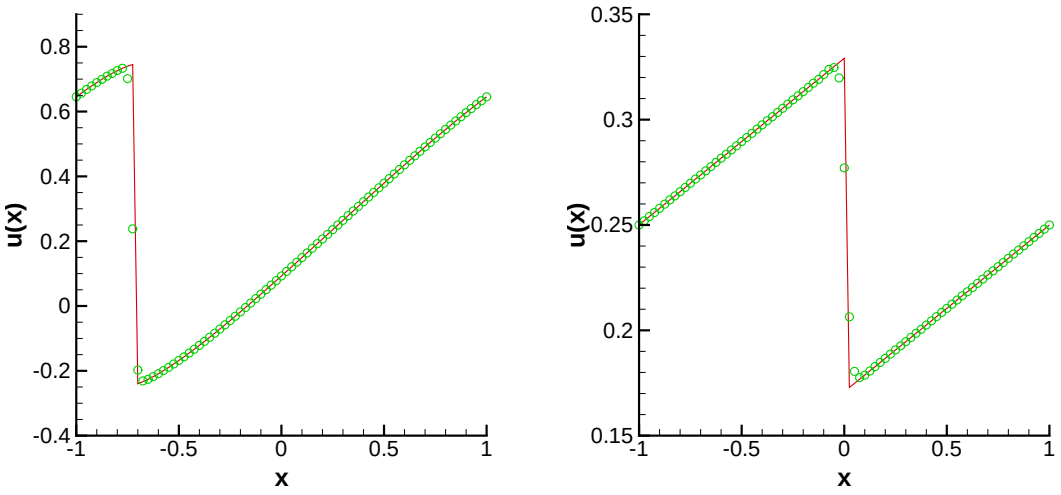

(a) $t = 1.1$ (b) $t = 12$

Figure 3.5: Burgers equation (3.12) solved by the efficient implementation. $h = 1/40$ and CFL $= 0.6$. Solid line: exact solution; Symbols: numerical solution.

with the conservative variables

$$\mathbf{U} = \begin{pmatrix} U_1 \\ U_2 \\ U_3 \end{pmatrix} = \begin{pmatrix} \rho \\ \rho u \\ E \end{pmatrix}$$

and the flux

$$\mathbf{F}(\mathbf{U}) = \begin{pmatrix} U_2 \\ (\gamma - 1)U_3 + \frac{3-\gamma}{2}\frac{U_2^2}{U_1} \\ \left(\gamma U_3 - \frac{\gamma-1}{2}\frac{U_2^2}{U_1}\right)\frac{U_2}{U_1} \end{pmatrix} = \begin{pmatrix} \rho u \\ \rho u^2 + p \\ u(E+p) \end{pmatrix}.$$

ρ, u, p, and E describe the density, velocity, pressure, and total energy, respectively. The equation of state has the form

$$E = \frac{p}{\gamma - 1} + \frac{1}{2}\rho u^2,$$

where γ is the (constant) specific heat ratio. The sound speed is $c = \sqrt{\gamma p/\rho}$. We consider a fifth order boundary treatment for the right boundary $x = 1$. The left boundary can be treated similarly.

Let us discretize the interval $(-1, 1)$ by a uniform mesh

$$-1 + h/2 = x_0 < x_1 < \ldots < x_N = 1 - h/2.$$

We assume $\mathbf{U}_0, \ldots, \mathbf{U}_N$ have been updated from time level t_{n-1} to time level t_n. We proceed as in scalar case to construct values of ghost points $\mathbf{U}_{N+1}, \ldots, \mathbf{U}_{N+3}$ by a fourth order Taylor expansion

$$(U_m)_j = \sum_{k=0}^{4} \frac{(x_j - 1)^k}{k!} U_m^{*(k)}, \quad m = 1, 2, 3, \quad j = N+1, \ldots, N+3, \tag{3.16}$$

where $U_m^{*(k)}$ is a $(5-k)$th order approximation of the spatial derivative $\left.\frac{\partial^k U_m}{\partial x^k}\right|_{x=1,\ t=t_n}$.

We first do a local characteristic decomposition to decide the inflow and outflow boundary conditions. Denote the Jacobian matrix of the flux near the boundary by

$$\mathbf{A}_\perp(\mathbf{U}_N) = \left.\frac{\partial \mathbf{F}(\mathbf{U})}{\partial \mathbf{U}}\right|_{\mathbf{U}=\mathbf{U}_N}.$$

$\mathbf{A}_\perp(\mathbf{U}_N)$ has three eigenvalues $\lambda_1 = u_N - c_N$, $\lambda_2 = u_N$, $\lambda_3 = u_N + c_N$ and a complete set of left eigenvectors $\mathbf{l}_1(\mathbf{U}_N)$, $\mathbf{l}_2(\mathbf{U}_N)$, $\mathbf{l}_3(\mathbf{U}_N)$ which forms a left eigenmatrix

$$\mathbf{L}(\mathbf{U}_N) = \begin{pmatrix} \mathbf{l}_1(\mathbf{U}_N) \\ \mathbf{l}_2(\mathbf{U}_N) \\ \mathbf{l}_3(\mathbf{U}_N) \end{pmatrix} = \begin{pmatrix} l_{1,1} & l_{1,2} & l_{1,3} \\ l_{2,1} & l_{2,2} & l_{2,3} \\ l_{3,1} & l_{3,2} & l_{3,3} \end{pmatrix}.$$

For definiteness, we assume $\lambda_1 < \lambda_2 < 0$ and $\lambda_3 > 0$. Thus two boundary conditions

are needed according to the well-posedness theory in Section 3.3. For example, we prescribe $U_m(1,t) = g_m(t)$, $m = 1, 2$. We define the local characteristic variables V_m at grid points near the boundary by

$$(V_m)_j = \mathbf{l}_m(\mathbf{U}_N)\mathbf{U}_j, \quad m = 1, 2, 3, \quad j = N-4, \ldots, N. \tag{3.17}$$

We extrapolate $(V_m)_j$ to the boundary with the fifth order WENO type extrapolation and denote the extrapolated kth order derivative of V_m at the boundary by $V_m^{*(k)}$, $k = 0, \ldots, 4$, $m = 1, 2, 3$.

We impose $U_1^{*(0)} = g_1(t_n)$ and $U_2^{*(0)} = g_2(t_n)$. Because of the signs of the corresponding eigenvalues, V_1, V_2 are the ingoing local characteristic variables and V_3 is outgoing. Therefore, for stability reason, $U_3^{*(0)}$ is solved by the extrapolation equation of V_3

$$l_{3,1}U_1^{*(0)} + l_{3,2}U_2^{*(0)} + l_{3,3}U_3^{*(0)} = V_3^{*(0)}. \tag{3.18}$$

Notice that the coefficient $l_{3,3} = \frac{\gamma-1}{2c_N^2}$ never vanishes. Next we find the first spatial derivatives $U_m^{*(1)}$ with the ILW procedure for U_1 and U_2, together with the extrapolation equation of V_3. Using the first two equations of the Euler system, we write the first time derivatives of U_1, U_2 as

$$\begin{aligned}
&\frac{\partial U_1}{\partial t} = -\frac{\partial U_2}{\partial x}, \\
&\frac{\partial U_2}{\partial t} = -(\gamma-1)\frac{\partial U_3}{\partial x} - \frac{3-\gamma}{2}\left(\frac{2U_2}{U_1}\frac{\partial U_2}{\partial x} - \frac{U_2^2}{U_1^2}\frac{\partial U_1}{\partial x}\right).
\end{aligned}$$

Notice that the left-hand side of the above equations is already known at the boundary. $U_m^{*(1)}$ can then be solved by the linear system

$$U_2^{*(1)} = -g_1'(t_n),$$

$$(\gamma-1)U_3^{*(1)}+\frac{3-\gamma}{2}\left[\frac{2U_2^{*(0)}}{U_1^{*(0)}}U_2^{*(1)}-\left(\frac{U_2^{*(0)}}{U_1^{*(0)}}\right)^2U_1^{*(1)}\right]=-g_2'(t_n), \tag{3.19}$$

$$l_{3,1}U_1^{*(1)}+l_{3,2}U_2^{*(1)}+l_{3,3}U_3^{*(1)}=V_3^{*(1)}.$$

Higher order derivatives $U_m^{*(k)}$, $k=2,3,4$, are simply obtained by extrapolation. Namely,

$$\mathbf{L}\left(\mathbf{U}_N\right)\begin{pmatrix}U_1^{*(k)}\\U_2^{*(k)}\\U_3^{*(k)}\end{pmatrix}=\begin{pmatrix}V_1^{*(k)}\\V_2^{*(k)}\\V_3^{*(k)}\end{pmatrix}. \tag{3.20}$$

In other words, the complicated ILW procedure is not needed for spatial derivatives of order higher than or equal to two, regardless of the direction of the local characteristic variables.

Before we summarize our algorithm, we turn to the issue of small eigenvalues. For simplicity, we assume λ_2 is close to zero. In this situation, the local characteristic variable V_2 can be considered either going into the boundary or going out of the boundary. On the one hand, if we assume an ingoing V_2, we still have the linear system (3.19), which is however ill-conditioned. The condition number will be larger and larger as λ_2 gets closer and closer to zero. To make the system well-conditioned, we may *add to* (3.19) the extrapolation equation of V_2

$$l_{2,1}U_1^{*(1)}+l_{2,2}U_2^{*(1)}+l_{2,3}U_3^{*(1)}=V_2^{*(1)}. \tag{3.21}$$

(3.19) and (3.21) form a system of four equations with three unknowns. We consider it as a linear least squares problem. The condition number of the 4×3 matrix is small. On the other hand, if only one boundary condition is prescribed, such as the case of no-penetration boundary condition $u=0$ at rigid walls, we have to assume an outgoing V_2. Now the second equation of (3.19) is *replaced by* (3.21) and the

resulting system is well-conditioned as well.

We summarize our fifth order boundary treatment at the right boundary $x = 1$ as follows, assuming that $\mathbf{U}_j$, $j = 0, \ldots, N$, have been updated from time level t_{n-1} to time level t_n.

1. Compute the eigenvalues $\lambda_m(\mathbf{U}_N)$ and left eigenvectors $\mathbf{l}_m(\mathbf{U}_N)$ of the Jacobian matrix $\mathbf{A}_\perp(\mathbf{U}_N)$ for $m = 1, 2, 3$. Decide the prescribed inflow boundary conditions $g_m(t)$ according to the signs of $\lambda_m(\mathbf{U}_N)$.

2. Form the local characteristic variables $(V_m)_j$, $j = N-4, \ldots, N$, as in (3.17). Obtain $V_m^{*(k)}$, which is a $(5-k)$th order approximation of the kth order derivative of V_m at the boundary, by the WENO type extrapolation.

3. Solve for $U_m^{*(0)}$, $m = 1, 2, 3$, by the prescribed boundary conditions and extrapolated values $V_m^{*(0)}$, such as (3.18).

4. Use the ILW procedure to write the first derivative of $g_m(t)$ as a linear combination of first spatial derivatives. Together with the extrapolation equations, form a linear system with $U_m^{*(1)}$ as unknowns (such as (3.19)) or a linear least squares problem (such as (3.19) and (3.21)). Solve for $U_m^{*(1)}$, $m = 1, 2, 3$.

5. For $k = 2, 3, 4$, solve for $U_m^{*(k)}$ by extrapolation equations (3.20). The ILW procedure is not needed in this step.

6. Impose the values of ghost points by the Taylor expansion (3.16).

3.4.5 2D reactive Euler equations

We consider 2D compressible reactive Euler equations in static geometries

$$\mathbf{U}_t + \mathbf{F}(\mathbf{U})_x + \mathbf{G}(\mathbf{U})_y = \mathbf{S}(\mathbf{U}), \quad (x, y) \in \Omega, \quad t > 0, \tag{3.22}$$

where

$$\mathbf{U} = \begin{pmatrix} U_1 \\ U_2 \\ U_3 \\ U_4 \\ U_5 \end{pmatrix} = \begin{pmatrix} \rho \\ \rho u \\ \rho v \\ E \\ \rho Y \end{pmatrix}, \quad \mathbf{F}(\mathbf{U}) = \begin{pmatrix} \rho u \\ \rho u^2 + p \\ \rho uv \\ u(E+p) \\ \rho uY \end{pmatrix},$$

$$\mathbf{G}(\mathbf{U}) = \begin{pmatrix} \rho v \\ \rho uv \\ \rho v^2 + p \\ v(E+p) \\ \rho vY \end{pmatrix}, \quad \mathbf{S}(\mathbf{U}) = \begin{pmatrix} 0 \\ 0 \\ 0 \\ 0 \\ \omega \end{pmatrix},$$

with "appropriate" boundary conditions and initial conditions. It is a system of conservation laws with source term representing chemical reactions. ρ, u, v, p, and E describe the density, x-velocity, y-velocity, pressure, and total energy, respectively. Y describes the reactant mass fraction and the source term is assumed to be in an Arrhenius form

$$\omega = -K_c \rho Y e^{-T^+/T},$$

where $T = p/\rho$ is the temperature, T^+ is the activation temperature and K_c is a constant. The equation of state has the form

$$E = \frac{p}{\gamma - 1} + \frac{1}{2}\rho(u^2 + v^2) + \rho QY, \tag{3.23}$$

where Q is the (constant) heat release due to the chemical reaction. Notice that if $Y \equiv 0$, then (3.22) reduces to the usual compressible Euler equations without source term.

General framework

We would like to extend our 1D boundary treatment technique to 2D problems. In Section 3.3 we give a counterexample showing that we cannot simply extend 1D well-posedness theory (Theorem 3.3.1) to 2D problems. Indeed, we have similar issues in designing numerical boundary conditions: a simple extension of our 1D boundary treatment may not be stable for 2D problems. However, the instability can be well-controlled by using least squares extrapolation for most problems of interest. In other words, although our methodology is somewhat ungrounded from the theoretical point of view, it usually gives stable and physically correct solutions in practice.

We proceed as for 1D problems. We assume the values of all the grid points inside Ω have been updated from time level t_{n-1} to time level t_n. For a ghost point $P = (x_i, y_j)$, we find a point $P_0 = (x_0, y_0) = \mathbf{x}_0$ on the boundary $\Gamma = \partial\Omega$ such that the normal $\mathbf{n}(\mathbf{x}_0)$ at P_0 goes through P. The sign of the normal $\mathbf{n}(\mathbf{x}_0)$ is chosen in such a way that it is positive if it points to the exterior of Ω. The point P_0 and the normal $\mathbf{n}(\mathbf{x}_0)$ can be obtained analytically, since we assume we have an explicit expression for the geometry of Γ. We set up a local coordinate system at P_0 by

$$\begin{pmatrix} \hat{x} \\ \hat{y} \end{pmatrix} = \begin{pmatrix} \cos\theta & \sin\theta \\ -\sin\theta & \cos\theta \end{pmatrix} \begin{pmatrix} x \\ y \end{pmatrix} = \mathbf{T} \begin{pmatrix} x \\ y \end{pmatrix}, \tag{3.24}$$

where θ is the angle between the normal $\mathbf{n}(\mathbf{x}_0)$ and the x-axis and $\mathbf{T}$ is a rotational

matrix. The $\hat{x}$-axis then points in the same direction as $\mathbf{n}(\mathbf{x}_0)$ and the $\hat{y}$-axis points in the tangential direction, see Figure 3.6.

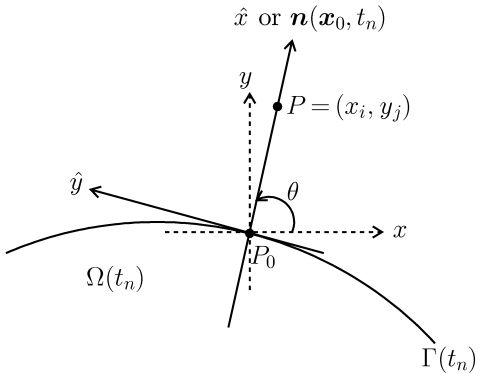

Figure 3.6: The local coordinate system (3.24). For static geometries, t_n dependence can be suppressed.

In this local coordinate system, the reactive Euler equations (3.22) are written as

$$\hat{\mathbf{U}}_t + \mathbf{F}(\hat{\mathbf{U}})_{\hat{x}} + \mathbf{G}(\hat{\mathbf{U}})_{\hat{y}} = \mathbf{S}(\hat{\mathbf{U}}), \tag{3.25}$$

where

$$\hat{\mathbf{U}} = \begin{pmatrix} \hat{U}_1 \\ \hat{U}_2 \\ \hat{U}_3 \\ \hat{U}_4 \\ \hat{U}_5 \end{pmatrix} = \begin{pmatrix} \rho \\ \rho\hat{u} \\ \rho\hat{v} \\ E \\ \rho Y \end{pmatrix}, \quad \begin{pmatrix} \hat{u} \\ \hat{v} \end{pmatrix} = \mathbf{T} \begin{pmatrix} u \\ v \end{pmatrix}.$$

For a fifth order boundary treatment, the value of the ghost point P is imposed by the Taylor expansion

$$(\hat{U}_m)_{i,j} = \sum_{k=0}^{4} \frac{\Delta^k}{k!} \hat{U}_m^{*(k)}, \quad m = 1, \ldots, 5, \tag{3.26}$$

where Δ is the $\hat{x}$-coordinate of P and $\hat{U}_m^{*(k)}$ is a $(5-k)$th order approximation of the normal derivative $\frac{\partial^k \hat{U}_m}{\partial \hat{x}^k}\Big|_{(x,y)=\mathbf{x}_0,\ t=t_n}$. We assume $\hat{\mathbf{U}}_0$ is the value of a grid point nearest to P_0 among all the grid points inside Ω. We denote the Jacobian matrix of the normal flux by

$$\mathbf{A}_\perp(\hat{\mathbf{U}}_0) = \left.\frac{\partial \mathbf{F}(\hat{\mathbf{U}})}{\partial \hat{\mathbf{U}}}\right|_{\hat{\mathbf{U}}=\hat{\mathbf{U}}_0}.$$

$\mathbf{A}_\perp(\hat{\mathbf{U}}_0)$ has five eigenvalues $\lambda_1 = \hat{u}_0 - c_0$, $\lambda_2 = \lambda_3 = \lambda_4 = \hat{u}_0$, $\lambda_5 = \hat{u}_0 + c_0$ and a complete set of left eigenvectors $\mathbf{l}_m(\hat{\mathbf{U}}_0)$, $m = 1, \ldots, 5$, which forms a left eigenmatrix

$$\mathbf{L}(\hat{\mathbf{U}}_0) = \begin{pmatrix} \mathbf{l}_1(\hat{\mathbf{U}}_0) \\ \mathbf{l}_2(\hat{\mathbf{U}}_0) \\ \mathbf{l}_3(\hat{\mathbf{U}}_0) \\ \mathbf{l}_4(\hat{\mathbf{U}}_0) \\ \mathbf{l}_5(\hat{\mathbf{U}}_0) \end{pmatrix} = \begin{pmatrix} l_{1,1} & l_{1,2} & l_{1,3} & l_{1,4} & l_{1,5} \\ l_{2,1} & l_{2,2} & l_{2,3} & l_{2,4} & l_{2,5} \\ l_{3,1} & l_{3,2} & l_{3,3} & l_{3,4} & l_{3,5} \\ l_{4,1} & l_{4,2} & l_{4,3} & l_{4,4} & l_{4,5} \\ l_{5,1} & l_{5,2} & l_{5,3} & l_{5,4} & l_{5,5} \end{pmatrix}.$$

For definiteness, we assume $\lambda_1 < 0$ and $\lambda_5 > \lambda_2 = \lambda_3 = \lambda_4 > 0$. Thus one boundary condition is needed at P_0 according to *1D* well-posedness theory. For example, the normal momentum is prescribed $\hat{U}_2(\mathbf{x}_0, t) = g_2(t)$.

The local characteristic variables V_m at grid points near P_0 are defined by

$$(V_m)_{\mu,\nu} = \mathbf{l}_m(\hat{\mathbf{U}}_0)\hat{\mathbf{U}}_{\mu,\nu}, \quad m = 1, \ldots, 5, \quad (x_\mu, y_\nu) \in \mathcal{E}_{i,j}, \tag{3.27}$$

where $\mathcal{E}_{i,j} \subset \Omega$ is a set of grid points used for extrapolation. We extrapolate $(V_m)_{\mu,\nu}$ to P_0 and denote the extrapolated kth order $\hat{x}$-derivative of V_m by $V_m^{*(k)}$, $k = 0, \ldots, 4$. The choice of $\mathcal{E}_{i,j}$ and the fifth order WENO type extrapolation in 2D will be described in detail in the next subsection. To stabilize the boundary treatment, the 2D WENO type extrapolation is composed of least squares extrapolation, instead of Lagrange extrapolation.

We solve $\hat{U}_m^{*(0)}$ by a linear system of equations

$$\begin{pmatrix} 0 & 1 & 0 & 0 & 0 \\ l_{2,1} & l_{2,2} & l_{2,3} & l_{2,4} & l_{2,5} \\ l_{3,1} & l_{3,2} & l_{3,3} & l_{3,4} & l_{3,5} \\ l_{4,1} & l_{4,2} & l_{4,3} & l_{4,4} & l_{4,5} \\ l_{5,1} & l_{5,2} & l_{5,3} & l_{5,4} & l_{5,5} \end{pmatrix} \begin{pmatrix} \hat{U}_1^{*(0)} \\ \hat{U}_2^{*(0)} \\ \hat{U}_3^{*(0)} \\ \hat{U}_4^{*(0)} \\ \hat{U}_5^{*(0)} \end{pmatrix} = \begin{pmatrix} g_2(t_n) \\ V_2^{*(0)} \\ V_3^{*(0)} \\ V_4^{*(0)} \\ V_5^{*(0)} \end{pmatrix}. \tag{3.28}$$

Here the first equation is the prescribed boundary condition. The other equations represent extrapolation of the four outgoing characteristic variables V_m, $m = 2, \ldots, 5$. Next, we use the ILW procedure for $\hat{U}_2$. The second equation of (3.25) gives us

$$\begin{aligned} \frac{\partial \hat{U}_2}{\partial t} &= -\left(\frac{\gamma-3}{2}\frac{\hat{U}_2^2}{\hat{U}_1^2} + \frac{\gamma-1}{2}\frac{\hat{U}_3^2}{\hat{U}_1^2} \right) \frac{\partial \hat{U}_1}{\partial \hat{x}} - (3-\gamma)\frac{\hat{U}_2}{\hat{U}_1}\frac{\partial \hat{U}_2}{\partial \hat{x}} \\ &\quad + (\gamma-1)\frac{\hat{U}_3}{\hat{U}_1}\frac{\partial \hat{U}_3}{\partial \hat{x}} - (\gamma-1)\frac{\partial \hat{U}_4}{\partial \hat{x}} + Q(\gamma-1)\frac{\partial \hat{U}_5}{\partial \hat{x}} - \frac{\partial}{\partial \hat{y}}\left(\frac{\hat{U}_2\hat{U}_3}{\hat{U}_1} \right). \end{aligned}$$

At the boundary, the left-hand side of the above equation is the known function $g_2'(t)$. The tangential derivative on the right-hand side can be computed by numerical differentiation, since we have obtained $\hat{U}_m^{*(0)}$ of all the ghost points. Thus $\hat{U}_m^{*(1)}$ can be solved by the linear system

$$\mathbf{A}^{*(0)} \begin{pmatrix} \hat{U}_1^{*(1)} \\ \hat{U}_2^{*(1)} \\ \hat{U}_3^{*(1)} \\ \hat{U}_4^{*(1)} \\ \hat{U}_5^{*(1)} \end{pmatrix} = \begin{pmatrix} -g_2'(t_n) - \frac{\partial}{\partial \hat{y}}\left(\frac{\hat{U}_2^{*(0)}\hat{U}_3^{*(0)}}{\hat{U}_1^{*(0)}} \right) \\ V_2^{*(1)} \\ V_3^{*(1)} \\ V_4^{*(1)} \\ V_5^{*(1)} \end{pmatrix}, \tag{3.29}$$

where

$$\mathbf{A}^{*(0)} = \begin{pmatrix} \frac{\gamma-3}{2}\left(\frac{\hat{U}_2^{*(0)}}{\hat{U}_1^{*(0)}}\right)^2 + \frac{\gamma-1}{2}\left(\frac{\hat{U}_3^{*(0)}}{\hat{U}_1^{*(0)}}\right)^2 & (3-\gamma)\frac{\hat{U}_2^{*(0)}}{\hat{U}_1^{*(0)}} & (1-\gamma)\frac{\hat{U}_3^{*(0)}}{\hat{U}_1^{*(0)}} & \gamma-1 & Q(1-\gamma) \\ l_{2,1} & l_{2,2} & l_{2,3} & l_{2,4} & l_{2,5} \\ l_{3,1} & l_{3,2} & l_{3,3} & l_{3,4} & l_{3,5} \\ l_{4,1} & l_{4,2} & l_{4,3} & l_{4,4} & l_{4,5} \\ l_{5,1} & l_{5,2} & l_{5,3} & l_{5,4} & l_{5,5} \end{pmatrix}.$$

Higher order derivatives $\hat{U}_m^{*(k)}$, $k = 2, 3, 4$, can be solved by extrapolation equations

$$\mathbf{L}(\hat{\mathbf{U}}_0) \begin{pmatrix} \hat{U}_1^{*(k)} \\ \hat{U}_2^{*(k)} \\ \hat{U}_3^{*(k)} \\ \hat{U}_4^{*(k)} \\ \hat{U}_5^{*(k)} \end{pmatrix} = \begin{pmatrix} V_1^{*(k)} \\ V_2^{*(k)} \\ V_3^{*(k)} \\ V_4^{*(k)} \\ V_5^{*(k)} \end{pmatrix}. \tag{3.30}$$

No-penetration boundary condition

The no-penetration boundary condition at rigid walls is $\hat{u} = 0$ or $\hat{U}_2 = 0$. In this case, the eigenvalues $\lambda_1 \approx -c_0 < 0$, $\lambda_5 \approx c_0 > 0$ and $\lambda_2 = \lambda_3 = \lambda_4 \approx 0$. Since only one boundary condition is prescribed, we consider V_m, $m = 2, \ldots, 5$, to be outgoing and V_1 to be ingoing, which falls into the same case as discussed above. (3.28) gives us $\hat{U}_2^{*(0)} = 0$. Then the first equation of (3.29) reduces to

$$\begin{aligned} & \frac{\gamma-1}{2}\left(\frac{\hat{U}_3^{*(0)}}{\hat{U}_1^{*(0)}}\right)^2 \hat{U}_1^{*(1)} + (1-\gamma)\frac{\hat{U}_3^{*(0)}}{\hat{U}_1^{*(0)}}\hat{U}_3^{*(1)} + (\gamma-1)\hat{U}_4^{*(1)} - Q(\gamma-1)\hat{U}_5^{*(1)} \\ = \; & \frac{\left(\hat{U}_3^{*(0)}\right)^2}{R\hat{U}_1^{*(0)}}, \end{aligned} \tag{3.31}$$

where R is the radius of curvature of $\partial\Omega$ at P_0. Notice that there is no tangential derivative in (3.31). Therefore, we do not need to do any numerical differentiation, which further simplifies the implementation.

(3.31) can also be derived by considering primitive variables, i.e., $\rho, \hat{u}, \hat{v}, p$ and Y, in the ILW procedure. At the rigid walls, we obtain

$$\frac{\partial p}{\partial \hat{x}} = \rho \frac{\hat{v}^2}{R},$$

which is equivalent to (3.31) because of the equation of state (3.23). In fact, it is sometimes more convenient to use primitive variables than to use conservative variables $\mathbf{U}$. For problems involving moving geometries, we can only use primitive variables because the boundary condition is prescribed in normal velocity. See Section 3.5 for details.

We now summarize our fifth order boundary treatment for the 2D problem (3.22). We assume the values of all the grid points inside Ω have been updated from time level t_{n-1} to time level t_n. Our goal is to impose the value of $(\hat{U}_m)_{i,j}$, $m = 1, \ldots, 5$, for each ghost point (x_i, y_j).

1. For each ghost point (x_i, y_j), we do the following three steps:

   - Decide the local coordinate system (3.24). Compute the eigenvalues $\lambda_m(\hat{\mathbf{U}}_0)$ and left eigenvectors $\mathbf{l}_m(\hat{\mathbf{U}}_0)$ of the Jacobian matrix $\mathbf{A}_\perp(\hat{\mathbf{U}}_0)$ for $m = 1, \ldots, 5$. Decide the prescribed inflow boundary conditions $g_m(t)$ according to the signs of $\lambda_m(\hat{\mathbf{U}}_0)$.

   - Form the local characteristic variables $(V_m)_{\mu,\nu}$, $(x_\mu, y_\nu) \in \mathcal{E}_{i,j}$, as in (3.27). Extrapolate $(V_m)_{\mu,\nu}$ to the boundary to obtain $V_m^{*(k)}$, $k = 0, \ldots, 4$, with fifth

order WENO type extrapolation. Details of the 2D extrapolation will be discussed in the next subsection.

- Solve for $\hat{U}_m^{*(0)}$, $m = 1, \ldots, 5$, by the prescribed boundary conditions and extrapolated values $V_m^{*(0)}$, such as (3.28).

2. For each ghost point (x_i, y_j), use the ILW procedure to write the first derivative of $g_m(t)$ as a linear combination of first normal derivatives plus tangential derivatives. Together with the extrapolation equations, form a linear system with $\hat{U}_m^{*(1)}$ as unknowns, such as (3.29). Solve for $\hat{U}_m^{*(1)}$, $m = 1, \ldots, 5$. For $k = 2, 3, 4$, solve for $\hat{U}_m^{*(k)}$ by extrapolation equations (3.30) where the ILW procedure is not needed.

3. Impose the values of the ghost points by the Taylor expansion (3.26).

If no-penetration boundary condition is considered at rigid walls, then the first equation of (3.29) is replaced by (3.31) in Step 2 with other steps unchanged. An alternative is to use primitive variables instead of conservative variables.

2D WENO type extrapolation

We return to the issue of 2D fifth order WENO type extrapolation. It is needed in the second bullet of Step 1 of the algorithm flowchart for 2D compressible Euler equations, regardless of the smoothness of the solution. For stability reason, we would like to use least squares extrapolation as building blocks. Namely, the number of points used to construct a 2D extrapolating polynomial is greater than the number of polynomial coefficients. In fact, Lagrange extrapolation sometimes leads to instability for 2D problems even with smooth solutions in our numerical experiments.

For a given ghost point (x_i, y_j), we aim to first construct a stencil $\mathcal{E} \subset \Omega$ for

extrapolation and then to obtain a $(5-k)$th order approximation of $\frac{\partial^k V}{\partial \hat{x}^k}\Big|_{(x,y)=\mathbf{x}_0}$, which is denoted by $V^{*(k)}$, $k = 0, \ldots, 4$. Compared with the notations used before, here we suppress the subscripts indicating the mth component of V and that the stencil $\mathcal{E}$ is for the ghost point (x_i, y_j). $\mathcal{E} = \bigcup_{r=0}^{4} \mathcal{E}_r$ consists of five substencils $\mathcal{E}_r$, $r = 0, \ldots, 4$, each of which is for constructing a least squares polynomial $p_r(x, y)$ in P^r, i.e.,

$$p_r(x, y) = \sum_{0 \le m+l \le r} a_{lm} x^l y^m$$

satisfying

$$p_r(x_\mu, y_\nu) = V_{\mu,\nu}, \text{ for all } (x_\mu, y_\nu) \in \mathcal{E}_r. \tag{3.32}$$

Notice that $p_r(x, y)$ has $(r+1)(r+2)/2$ degrees of freedom. We choose $\mathcal{E}_r$ such that it contains $(r+1)^2$ points and (3.32) holds in the sense of least squares if $r > 0$.

We take $r = 3$ as an example to show how to choose $\mathcal{E}_r$. $\mathcal{E}_3$ is composed of 16 square points sketched in Figure 3.7. It contains four 1D substencils $\mathcal{S}_l$, $l = 0, \ldots, 3$. Suppose the normal $\mathbf{n}(x_0)$ (or $\hat{x}$-axis) intersects the grid line $y = y_{n-l}$ at a point P_l^*. We denote the grid point on the horizontal line $y = y_{n-l}$ which is just to the left of P_l^* by (x_m^l, y_{n-l}). Then we set

$$\mathcal{S}_l = \{(x_{m-1}^l, y_{n-l}), (x_m^l, y_{n-l}), (x_{m+1}^l, y_{n-l}), (x_{m+2}^l, y_{n-l})\}, \quad l = 0, \ldots, 3,$$

and $\mathcal{E}_3 = \bigcup_{l=0}^{3} \mathcal{S}_l$. Notice that we have to shift $\mathcal{S}_0$ to the left by one grid point so that $\mathcal{S}_0$ lies in Ω.

On each $\mathcal{E}_r$, $r = 0, \ldots, 4$, $V^{*(k)}$ can be extrapolated by

$$V^{*(k)} = \frac{\partial^k}{\partial \hat{x}^k} p_r(x, y)\Big|_{(x,y)=\mathbf{x}_0}.$$

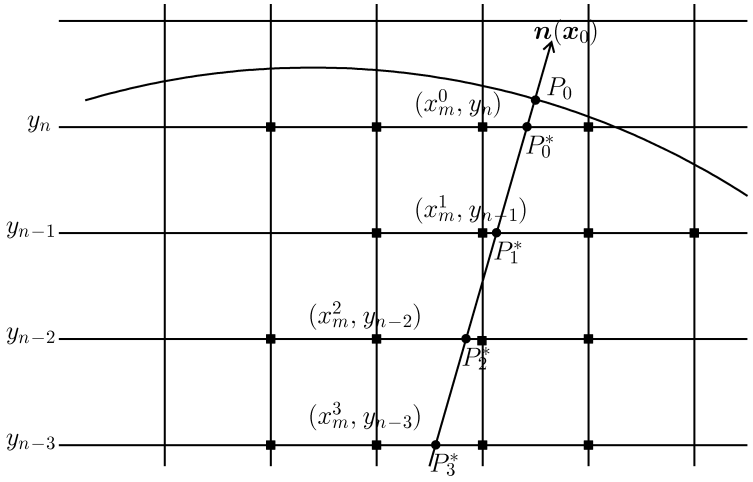

Figure 3.7: The choice of $\mathcal{E}_3$ (square points) for 2D WENO type extrapolation.

We seek WENO type extrapolation of the form

$$V^{*(k)} = \sum_{r=0}^{4} \omega_r \frac{\partial^k}{\partial \hat{x}^k} p_r(x,y)\bigg|_{(x,y)=\mathbf{x}_0}, \tag{3.33}$$

where ω_r are nonlinear weights. The nonlinear weights ω_r are defined by

$$\omega_r = \frac{\tilde{\omega}_r}{\sum_{\nu=0}^{4} \tilde{\omega}_\nu},$$

with

$$\tilde{\omega}_r = \frac{\gamma_r}{(\varepsilon + \beta_r)^q}, \tag{3.34}$$

where $\gamma_0 = 2h^4$, $\gamma_1 = 2h^3$, $\gamma_2 = 2h^2$, $\gamma_3 = 2h$, $\gamma_4 = 1 - \sum_{r=0}^{3} \gamma_r$, $\varepsilon = 10^{-6}$, and $q \geq 3$ is an integer. The constant integer $q \geq 3$ is determined on a case-by-case basis. Generally, the stronger the discontinuity, the larger q we need to stabilize the extrapolation. This is because a larger q leads to smaller nonlinear weights assigned to nonsmooth stencils. The smoothness indicators β_r are determined by

$$\begin{aligned}
&\beta_0 = 2h^2, \\
&\beta_r = \sum_{1 \leq |\alpha| \leq r} \int_K |K|^{|\alpha|-1} \left(D^\alpha p_r(x,y)\right)^2 dxdy, \quad r = 1, \ldots, 4,
\end{aligned}$$

where α is a multi-index and $K = [x_0 - h/2, x_0 + h/2] \times [y_0 - h/2, y_0 + h/2]$. We can show that (3.33) is $(5-k)$th order accurate if V is smooth in $\mathcal{E}$ and ω_r vanishes as $h \to 0$ if $\mathcal{E}_r$ contains a discontinuity.

Notice that the stencil $\mathcal{E}$ for the fifth order WENO type extrapolation contains at least 25 grid points. For most cases, it is eventually possible to fit the wide stencil in the computational domain by mesh refinement. However, in some special cases, we have to reduce the order of extrapolation, see Example 3.5.4.

3.4.6 Numerical examples

We test our fifth order boundary treatment with efficient implementation in this section. For accuracy tests, we take $\Delta t = O(h^{5/3})$ in the third order RK time integration (2.8) in order to have fifth order accuracy in time. For other cases, we take $\Delta t = O(h)$ and the CFL number as 0.6. The specific heat ratio γ in (reactive) Euler equations is taken as $\gamma = 1.4$ and the power q in (3.15) or (3.34) is taken as $q = 3$, unless otherwise indicated. The L^1 error and L^∞ error are defined as $h^2 \sum_{\{(i,j):(x_i,y_j)\in\mathcal{D}\}} |e_{i,j}|$ and $\max_{\{(i,j):(x_i,y_j)\in\mathcal{D}\}} |e_{i,j}|$ respectively. Here $e_{i,j}$ denotes the error at grid point (x_i, y_j) and $\mathcal{D}$ is the region where the errors are measured. $\mathcal{D} = \Omega$ unless otherwise indicated.

1D problems

Example 3.4.2. We start with the wave equation

$$\begin{cases} u_t + u_x = 0 & x \in (-1,1), \quad t > 0, \\ u(x,0) = 0.25 + 0.5\sin(\pi x) & x \in [-1,1], \\ u(-1,t) = g(t) & t > 0. \end{cases} \tag{3.35}$$

The left boundary $x = -1$ is an inflow boundary, where a boundary condition is prescribed. The right boundary $x = 1$ is an outflow boundary, where no boundary condition is needed.

We first take

$$g(t) = 0.25 - 0.5\sin\left[\pi(1+t)\right] \tag{3.36}$$

so that the IBV problem has a smooth exact solution

$$u(x,t) = 0.25 + 0.5\sin\left[\pi(x-t)\right].$$

The errors at $t = 1$ are listed in Table 3.3. We can clearly see the desired fifth order convergence.

Table 3.3: Errors of the wave equation (3.35) with boundary condition (3.36). $t = 1$.

h	L^1 error	order	L^∞ error	order
1/20	8.72E-05		3.94E-04	
1/40	9.45E-07	6.53	5.17E-06	6.25
1/80	1.56E-08	5.92	2.21E-08	7.87
1/160	4.93E-10	4.98	6.66E-10	5.05
1/320	1.55E-11	4.99	1.88E-11	5.15

Next, we take $g(t)$ as

$$g(t) = \begin{cases} 0.25 & t \leq 1, \\ -1 & t > 1. \end{cases} \tag{3.37}$$

The exact solution is then

$$u(x,t) = \begin{cases} -1 & x < t-2, \\ 0.25 & t-2 \leq x < t-1, \\ 0.25 + 0.5\sin\left[\pi(x-t)\right] & x \geq t-1. \end{cases}$$

For $t \leq 1$, the exact solution has a discontinuity in its first derivative, due to the definition of $g(t)$. For $t > 1$, a discontinuity enters the computational domain from the inflow boundary. We can observe from Figure 3.8 that both types of discontinuities are well captured by our method.

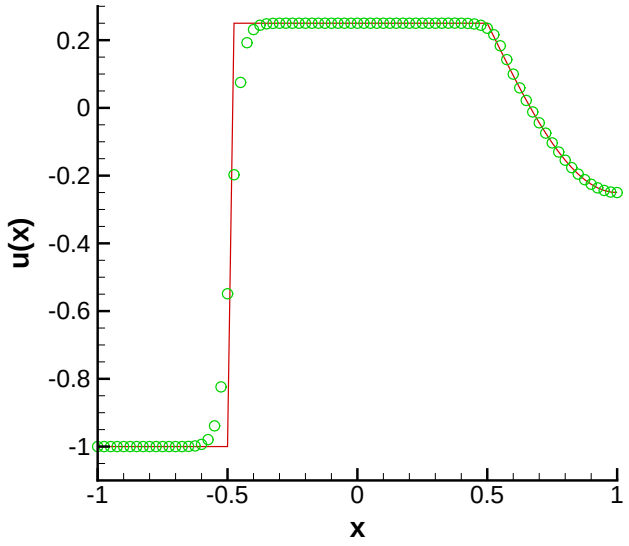

Figure 3.8: Wave equation (3.35) with boundary condition (3.37). $h = 1/40$ and $t = 1.5$. Solid line: exact solution; Symbols: numerical solution.

Example 3.4.3. We test 1D Euler equations with smooth solutions. The domain is $(-\pi, \pi)$ and the initial condition is

$$\rho(x,0) = 1 + 0.2\sin x,$$

$$u(x,0) = 1,$$

$$p(x,0) = 2.$$

We want to impose the boundary conditions such that the exact solution is simply a translation of the initial condition

$$p(x,t) = 1 + 0.2\sin(x-t),$$

$$u(x,t) = 1,$$

$$p(x,t) = 2.$$

At both boundaries, we have $\lambda_1 < 0$ and $\lambda_3 > \lambda_2 > 0$. We prescribe $\rho(-\pi,t)$, $u(-\pi,t)$ and $\rho(\pi,t)$. The density errors are listed in Table 3.4. We can clearly see the designed fifth order convergence.

Table 3.4: Density errors and convergence rates in Example 3.4.3. $h = 2\pi/N$ and $t = 2$.

N	L^1 error	Order	L^∞ error	Order
40	7.02E-05		5.84E-04	
80	2.82E-07	7.96	2.84E-06	7.69
160	3.16E-09	6.48	1.78E-08	7.31
320	9.89E-11	5.00	5.58E-10	5.00
640	3.06E-12	5.02	1.73E-11	5.01

Example 3.4.4. We test 1D Euler equations with shocks. We consider the interaction of two blast waves [69]. The initial data are

$$\mathbf{U}(x,0) = \begin{cases} \mathbf{U}_L & 0 < x < 0.1, \\ \mathbf{U}_M & 0.1 < x < 0.9, \\ \mathbf{U}_R & 0.9 < x < 1, \end{cases}$$

where $\rho_L = \rho_M = \rho_R = 1$, $u_L = u_M = u_R = 0$, $p_L = 10^3$, $p_M = 10^{-2}$, $p_R = 10^2$. There are rigid walls at both $x = 0$ and $x = 1$. This problem involves multiple re-

flections of shocks and rarefactions off the walls. There are also multiple interactions of shocks and rarefactions with each other and with contact discontinuities. The density profile at $t = 0.038$ is shown in Figure 3.9(a) with $h = 1/800$ and in Figure 3.9(b) with $h = 1/1600$. The reference solution is computed by the fifth order WENO scheme with $h = 1/16000$, together with the reflection technique at both boundaries. Our fifth order boundary treatment gives an excellent non-oscillatory resolution.

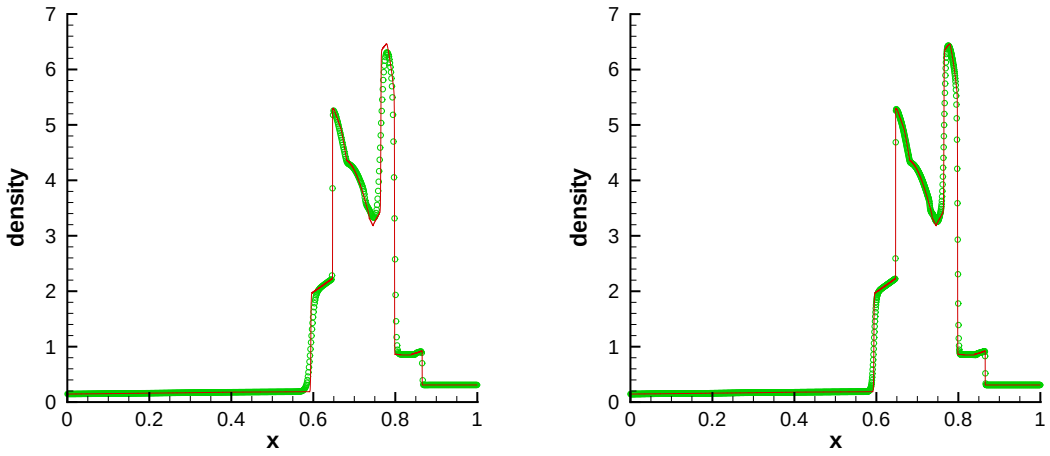

(a) $h = 1/800$ (b) $h = 1/1600$

Figure 3.9: The density profiles of the blast wave problem in Example 3.4.4. Solid lines: reference solution computed by the fifth order WENO scheme with $h = 1/16000$, together with the reflection technique at boundaries; Symbols: numerical solutions by our fifth order boundary treatment.

2D scalar equations

Example 3.4.5. We start our 2D examples with the wave equation on a disk

$$\begin{cases} u_t + u_x + u_y = 0 & (x,y) \in \Omega, \quad t > 0, \\ u(x,y,0) = 0.25 + 0.5\sin\left[\pi(x+y)\right] & (x,y) \in \bar{\Omega}, \\ u(x,y,t) = g(x,y,t) & (x,y) \in \Gamma_{\text{in}}, \quad t > 0, \end{cases} \tag{3.38}$$

where

$$\Omega = \{(x, y) : x^2 + y^2 < 0.5\},$$
$$\Gamma_{\text{in}} = \{(x, y) : x^2 + y^2 = 0.5 \text{ and } x + y \leq 0\}.$$

The domain is illustrated in Figure 3.10(a) with a coarse mesh. Notice that the grid points are not located on the boundary.

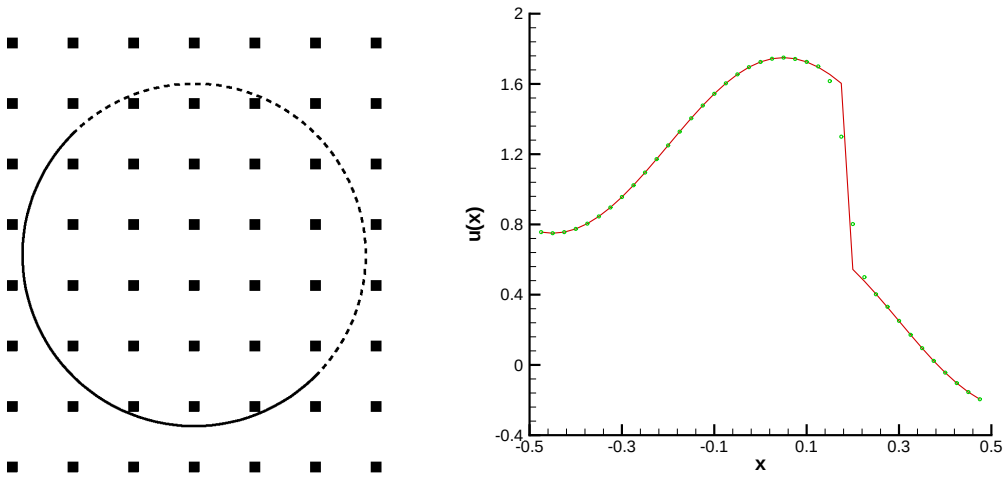

(a) computational domain (b) computational result

Figure 3.10: Left: Domain Ω of the 2D wave equation (3.38). Square points indicate some of the grid points. Solid lines: inflow boundary; Dashed lines: outflow boundary. Right: 2D wave equation (3.38) with boundary condition (3.40). $h = 1/40$ and $t = 0.8$. Cut along the diagonal. Solid line: exact solution; Symbols: numerical solution.

Special care must be taken when we impose the inflow boundary condition on a ghost point near the intersection of the inflow boundary and the outflow boundary, which is $(-0.5, 0.5)$ or $(0.5, -0.5)$ in our example. In this situation, the ILW procedure involves a small number divided by a small number, which ruins the accuracy or makes the scheme blow up. There are two ways to deal with this ill-conditioned problem. The first one is using the analytical expressions of time derivatives and tangential derivatives. The other one is adding an extrapolation equation to the

Table 3.5: Errors of the 2D wave equation (3.38) with boundary condition (3.39). $t = 0.8$.

h	L^1 error	order	L^∞ error	order
1/20	2.06E-04		6.28E-03	
1/40	6.17E-06	5.06	1.18E-04	5.73
1/80	6.01E-08	6.68	3.12E-07	8.57
1/160	1.82E-09	5.05	9.21E-09	5.08
1/320	5.74E-11	4.98	2.81E-10	5.03

equation obtained by the ILW procedure and solving a least squares problem. We use the former here because the analytical expressions are available. We use the latter in the next example.

We take

$$g(x, y, t) = 0.25 + 0.5 \sin\left[\pi(x + y - 2t)\right] \tag{3.39}$$

so that we have a smooth exact solution

$$u(x, y, t) = 0.25 + 0.5 \sin\left[\pi(x + y - 2t)\right].$$

The errors are listed in Table 3.5. We can clearly see fifth order convergence.

We next take a discontinuous boundary condition

$$g(x, y, t) = \begin{cases} 0.25 + 0.5 \sin \pi(x + y - 2t) & x + y - 2t > -1.23, \\ 1.25 + 0.5 \sin \pi(x + y - 2t) & x + y - 2t \leq -1.23. \end{cases} \tag{3.40}$$

Now we have a discontinuous exact solution. The numerical solution and exact solution along the diagonal are shown in Figure 3.10(b). We can see an excellent non-oscillatory resolution.

Table 3.6: Errors of the 2D Burgers equation (3.41). $t = 0.15$.

h	L^1 error	order	L^∞ error	order
1/20	3.05E-04		9.44E-03	
1/40	1.01E-05	4.92	6.18E-04	3.93
1/80	1.64E-07	5.94	1.28E-05	5.59
1/160	5.13E-09	5.00	5.22E-07	4.62
1/320	1.44E-10	5.15	2.97E-08	4.14

Example 3.4.6. We next test the 2D Burgers equation on a disk

$$\begin{cases} u_t + \frac{1}{2}\left(u^2\right)_x + \frac{1}{2}\left(u^2\right)_y = 0 & (x,y) \in \Omega, \quad t > 0, \\ u(x,y,0) = 0.75 + 0.5\sin\left[\pi(x+y)\right] & (x,y) \in \bar{\Omega}, \\ u(x,y,t) = g(x,y,t) & (x,y) \in \Gamma_{\text{in}}, \quad t > 0, \end{cases} \tag{3.41}$$

where

$$\Omega = \{(x,y) : x^2 + y^2 < 0.5\},$$
$$\Gamma_{\text{in}} = \{(x,y) : x^2 + y^2 = 0.5 \text{ and } x + y \leq 0\}.$$

Here $g(x,y,t) = w(x,y,t)$, where $w(x,y,t)$ is the exact solution of the initial value problem on $(-1,1) \times (-1,1)$ with periodic boundary conditions. At $t = 0.15$, we have a smooth solution. The errors are listed in Table 3.6. We achieve the designed fifth order accuracy in the L^1 norm. At $t = 0.55$, a shock is fully developed in the interior of Ω. A shock begins entering Ω from the inflow boundary at a later time and the shock front is located at the line $x + y = 0$ at $t = 6$. We can see from Figure 3.11 that the shock is well captured.

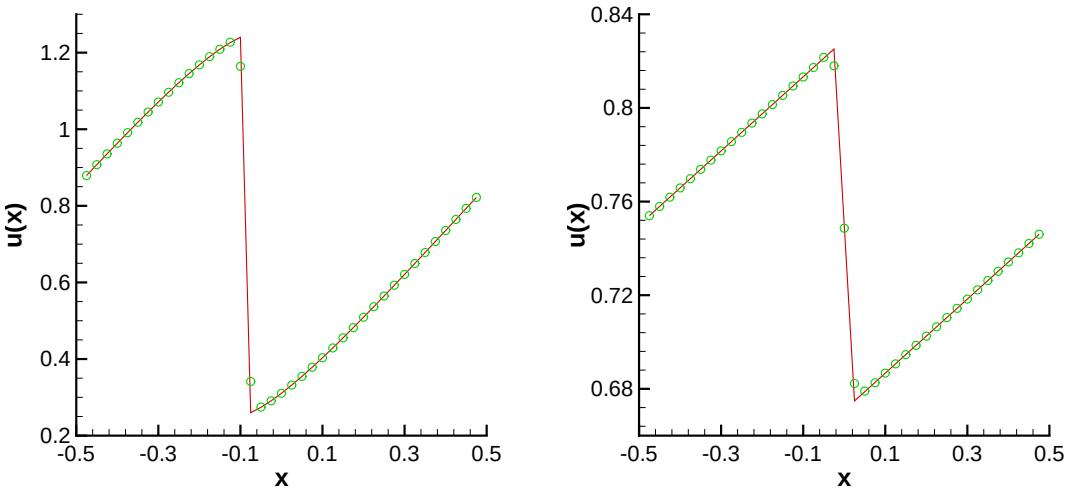

(a) $t = 0.55$ (b) $t = 6$

Figure 3.11: 2D Burgers equation (3.41). $h = 1/40$. Cut along the diagonal. Solid line: exact solution; Symbols: numerical solution.

2D Euler equations

Example 3.4.7. We test 2D Euler equations with smooth analytical solutions. We consider the vortex evolution problem on a disk $\Omega = \{(x, y) : x^2 + y^2 < 0.5\}$. The mean flow is $\rho = p = u = v = 1$. We add to this mean flow an isentropic vortex perturbation centered at $(x_0, y_0) = (0.3, 0.3)$ in (u, v) and in the temperature $T = p/\rho$, no perturbation in the entropy $S = p/\rho^\gamma$

$$
\begin{aligned}
(\delta u, \delta v) &= \frac{\epsilon}{2\pi} e^{0.5(1-r^2)}(-\bar{y}, \bar{x}), \\
\delta T &= -\frac{(\gamma - 1)\epsilon^2}{8\gamma\pi^2} e^{(1-r^2)}, \\
\delta S &= 0,
\end{aligned}
$$

where $(\bar{x}, \bar{y}) = (x - x_0, y - y_0)$, $r^2 = \bar{x}^2 + \bar{y}^2$ and the vortex strength is $\epsilon = 5$. We regard the exact solution $\mathbf{U}(x, y, t)$ as the passive convection of the vortex with the

mean velocity and take boundary conditions from $\mathbf{U}(x, y, t)$ according to 1D well-posedness theory. The number of boundary conditions is determined by the signs of the four eigenvalues λ_m which vary both in space and in time. The density errors are listed in Table 3.7. We can see that the designed fifth order convergence is achieved in the L^1 norm.

Table 3.7: Density errors of the vortex evolution problem on a disk in Example 3.4.7. $t = 0.1$.

h	L^1 error	Order	L^∞ error	Order
1/20	1.94E-07		2.55E-05	
1/40	3.66E-09	5.73	1.94E-07	7.04
1/80	1.22E-10	4.91	1.07E-08	4.17
1/160	4.26E-12	4.83	6.00E-10	4.16

Example 3.4.8. We test the double Mach reflection problem [69] which involves a rigid wall not aligned with the grid lines. This problem is initialized by sending a horizontally moving shock into a rigid wall inclined by a 30° angle. In order to impose the no-penetration boundary condition by the reflection technique, people usually solve an equivalent problem that puts the wall horizontal and puts the shock 60° angle inclined to the wall, see for example [33, 57]. We consider the solution of the equivalent problem as our reference solution. Another way to apply the reflection technique is to use a multidomain WENO method [54].

We are able to solve the original problem on a uniform mesh with our fifth order boundary treatment in conservative variables. The computational domain is sketched in Figure 3.12(a), together with some of the grid points near the wall indicating that the wall is not aligned with the grid lines. Initially a right-moving Mach 10 shock is positioned at $(0, 0)$ making an angle of 90° with the x-axis. At $y = 0$, the exact postshock condition is imposed. At the top boundary, the flow values are set to describe the exact motion of the Mach 10 shock. Supersonic inflow and outflow boundary conditions are used at the left and right boundary respectively. The power q in (3.34) is taken as $q = 20$ to stabilize our boundary treatment. Figure 3.12(b)

shows the density contour with $h = 1/320$ at $t = 0.2$. A zoomed-in region near the double Mach stem is shown in Figure 3.13(a). The region is rotated and translated for the ease of comparison. In Figure 3.13(b), we show the reference solution on a mesh with comparable size. Figures 3.13(c) and 3.13(d) show the density contours on a refined mesh. We can see that the results of our boundary treatment are very similar to those obtained by the reflection technique. The slight difference comes perhaps from the fact we impose the no-penetration condition strongly while the reflection technique imposes it weakly.

Example 3.4.9. This is an example involving a curved wall. The problem is initialized by a Mach 3 flow moving toward a circular cylinder of unit radius positioned at the origin on a x-y plane. In order to impose the no-penetration boundary condition at the surface of the cylinder by the reflection technique, a particular mapping from the unit square to the physical domain is used in [33]. Using our boundary treatment, we are able to solve this problem directly in the physical domain, which is shown in Figure 3.14(a), together with some of the grid points near the cylinder which indicate boundary cuts the grid in an arbitrary fashion. The computational domain is the upper half of the physical domain, due to the symmetry of this problem. At $y = 0$, the reflection technique is used. Supersonic inflow boundary condition is used at the left boundary $x = -3$; supersonic outflow boundary condition is used at the top boundary $y = 6$ and at the right boundary $x = 0$. Our fifth order boundary treatment in primitive variables with $q = 10$ in (3.34) is applied at the surface of the cylinder. Notice that although the initial condition is incompatible with the no-penetration boundary condition, we do not encounter any problem if using primitive variables, while difficulty arises if we use conservative variables as reported in [64].

The pressure contour at steady state is shown in Figure 3.15 with different mesh sizes. The bow shock is well-captured by our method. For a more quantitative veri-

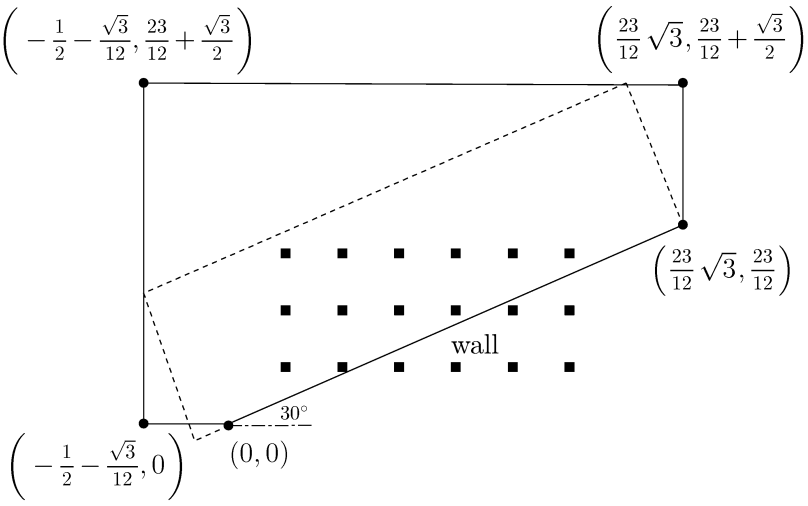

(a) computational domain

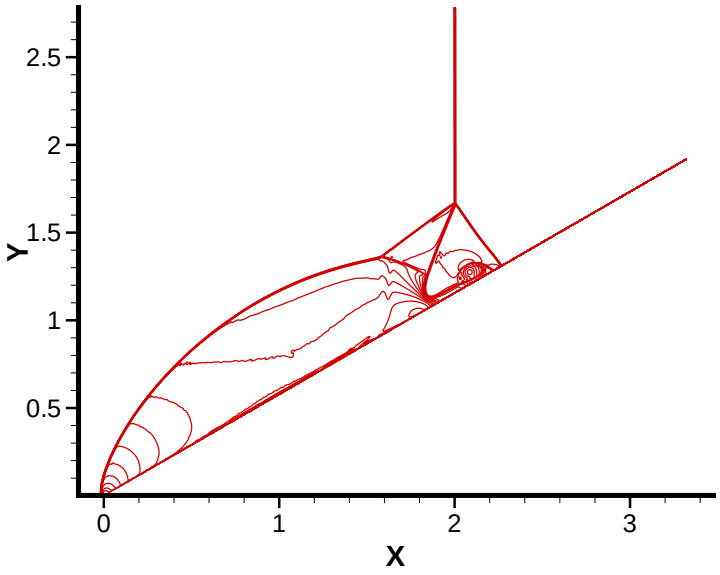

(b) density contour

Figure 3.12: Top: The computational domain (solid line) of the double Mach reflection problem in Example 3.4.8. The dashed line indicates the computational domain used in [33, 57]. The square points indicate some of the grid points near the wall. Illustrative graph, not to scale. Bottom: Density contour of double Mach reflection, 30 contour lines from 1.731 to 20.92. $h = 1/320$.

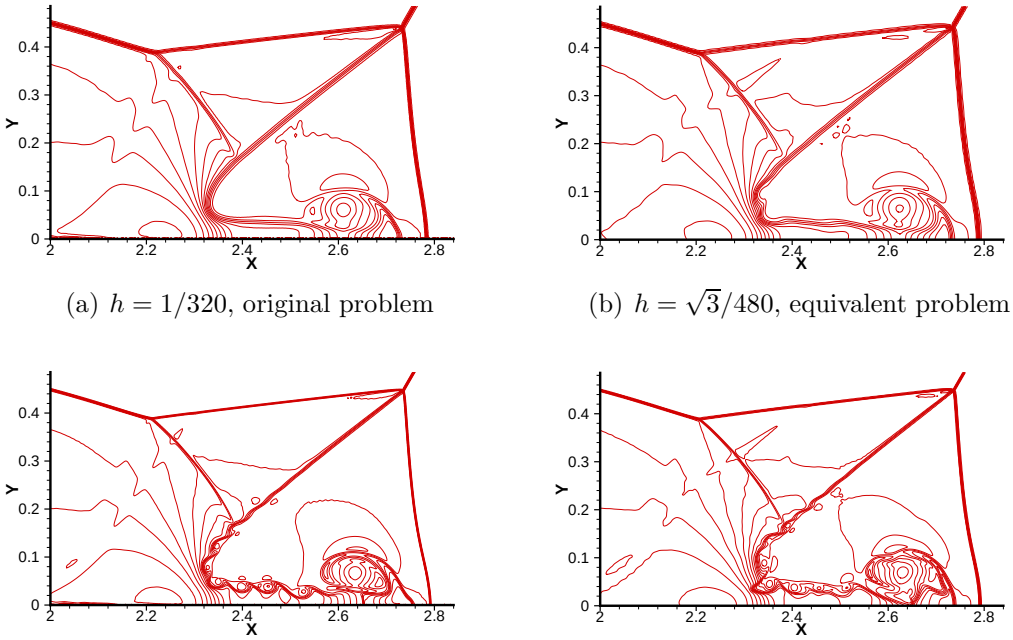

(a) $h = 1/320$, original problem

(b) $h = \sqrt{3}/480$, equivalent problem

(c) $h = 1/640$, original problem

(d) $h = \sqrt{3}/960$, equivalent problem

Figure 3.13: Density contours of double Mach reflection in Example 3.4.8, 30 contour lines from 1.731 to 20.92. Zoomed-in near the double Mach stem. The plots in the left column are rotated and translated for comparison.

fication, we take advantage of the entropy along the surface, which can be computed analytically by using the Rankine-Hugoniot conditions for the streamline normal to the bow shock at $y = 0$. Since there is usually no grid point located on the surface, we compute the entropy errors of the state $\hat{U}_m^{*(0)}$, $m = 1, \ldots, 4$, which is the constant term in the Taylor expansion (3.26), for all the ghost points. We can see superlinear convergence rates in Table 3.8. In other words, although the accuracy of our high order boundary treatment degenerates to first order near the shock, it is expected to be higher than first order in the smooth part of the solution.

Example 3.4.10. We consider shock reflection from a circular cylinder. The physical domain is $[-0.5, 0.5] \times [-0.5, 0.5]$. The cylinder is located at $(0, 0)$ and has a radius of 0.2. Initially a Mach 3 shock is located at $x = -0.3$. The state in front of the shock is $\rho = 1.4$, $u = v = 0$, $p = 1$. This problem is considered by Forrer and Jeltsch [17]. Helzel et al. [29] test the same problem but with a Mach 2 shock.

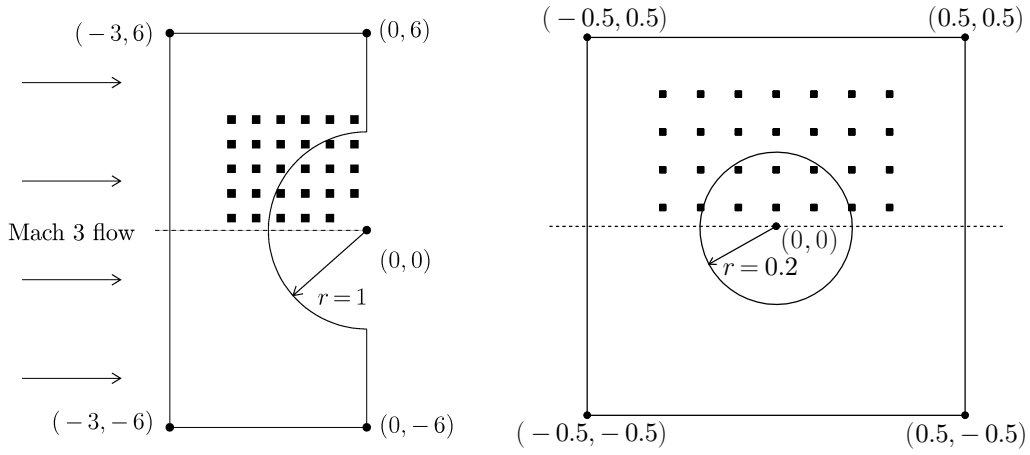

(a) Example 3.4.9 (b) Example 3.4.10

Figure 3.14: Left: Physical domain of flow past a cylinder in Example 3.4.9. Right: Physical domain of shock reflection from a cylinder in Example 3.4.10. In both figures, the square points indicate some of the grid points near the cylinder. Illustrative sketch, not to scale.

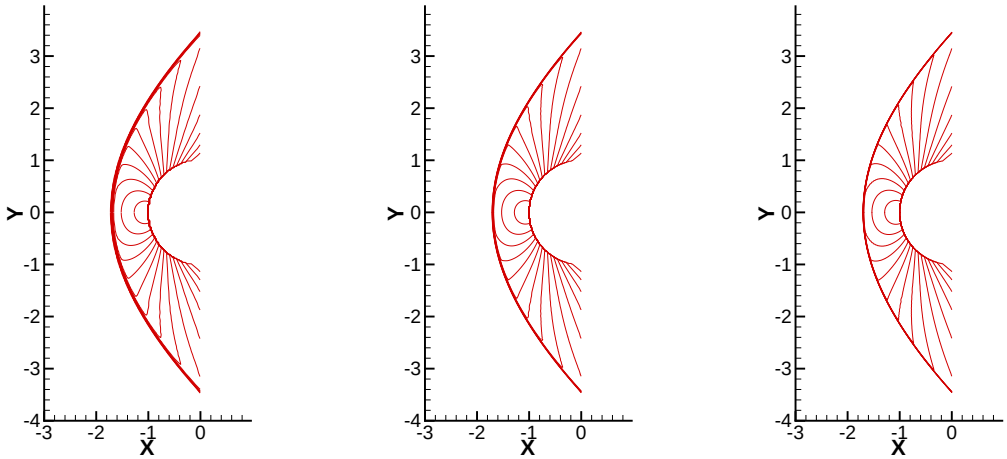

(a) $h = 1/40$ (b) $h = 1/80$ (c) $h = 1/160$

Figure 3.15: Pressure contours of flow past a cylinder in Example 3.4.9, 20 contour lines from 2 to 15.

Table 3.8: L^∞ entropy errors on the surface of the cylinder and rates of convergence in Example 3.4.9.

h	L^∞ error	Order
1/20	1.68E-02	
1/40	7.06E-03	1.25
1/80	1.88E-03	1.91
1/160	7.50E-04	1.33

The computational domain is the upper half of the physical domain due to the symmetry of the problem, see Figure 3.14(b). We apply our fifth order boundary treatment in primitive variables with $q = 20$ in (3.34) at the surface of the cylinder. Figure 3.16 shows the density contours at $t = 0.18$ with $h = 1/320$ and $h = 1/640$. The density contour plot with $h = 1/320$ in Figure 3.16(a) agrees well with the result computed on a mesh with $h = 1/300$ in Figure 11 of [17].

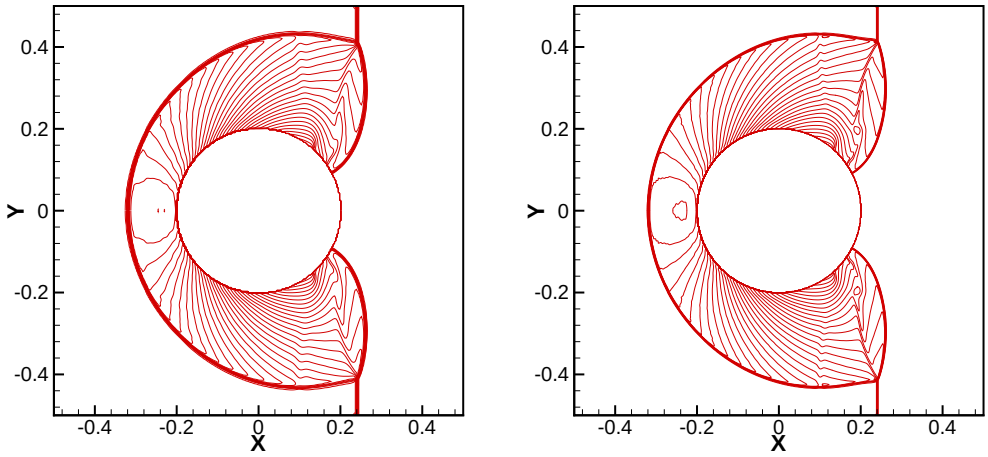

(a) $h = 1/320$ (b) $h = 1/640$

Figure 3.16: Density contours of shock reflection from a circular cylinder in Example 3.4.10. 39 contours from 0 to 13.

2D reactive Euler equations

Example 3.4.11. We would like to test the accuracy of our boundary treatment for 2D reactive Euler equations in this example. Unfortunately, it is difficult to construct an analytical solution with no-penetration boundary condition at rigid curved walls. We construct isentropic flows so that we are able to measure the entropy errors. We set the source term $\omega = 0$ in (3.22) such that isentropic flows can be maintained as long as the flows keep smooth. Namely, we only consider the transport of the chemical reactants. The heat release is set to $Q = 2$.

We consider a region $[-4,4]\times[-4,4]$ with all the boundaries as rigid walls. A circular cylinder with unit radius is centered at the origin. The computational domain is then $\Omega=[-4,4]\times[-4,4]\cap\{(x,y):x^2+y^2>1\}$. The initial conditions should be compatible with the no-penetration boundary condition at the rigid walls and at the surface of the cylinder. For this purpose, we set

$$\begin{aligned}
u(x,y,0)&=\lambda_1(x,y)u_1(x,y),\\
v(x,y,0)&=\frac{1}{2}\left[\lambda_1(x,y)v_1(x,y)+\lambda_2(x,y)v_2(x,y)\right],
\end{aligned}$$

where

$$\begin{aligned}
\lambda_1(x,y)&=\frac{\left(4\sqrt{2}-1\right)\left(\sqrt{x^2+y^2}-1\right)}{\left(\sqrt{16+y^2}-1\right)\left(\sqrt{16+x^2}-1\right)},\\
\lambda_2(x,y)&=\frac{\sqrt{x^2+y^2}(x^2-16)(y^2-16)}{\left(\frac{x^2}{x^2+y^2}-16\right)\left(\frac{y^2}{x^2+y^2}-16\right)},\\
u_1(x,y)&=\sin\left(\frac{\pi}{4}x\right)\sin^2\left(\frac{\pi}{4}y\right),\\
v_1(x,y)&=u_1(y,x),\\
v_2(x,y)&=\frac{1}{16}\left(x^2+y^2-1\right)\sin\left(\frac{\pi}{4}x\right).
\end{aligned}\tag{3.42}$$

The other initial conditions are $\rho(x,y,0)=p(x,y,0)=1$ and

$$Y(x,y,0)=\frac{1}{2}\left[1+\sin^2\left(\frac{\pi}{4}x\right)\sin^2\left(\frac{\pi}{4}y\right)\right].$$

We apply our fifth order boundary treatment in primitive variables at the surface of the cylinder and the reflection technique at the rigid walls. Figure 3.17 shows the density contour with $h=1/20$ at $t=0.5$. The entropy errors in the region $[-3,3]\times[-3,3]$ at the same time level are listed in Table 3.9. Fifth order convergence is achieved.

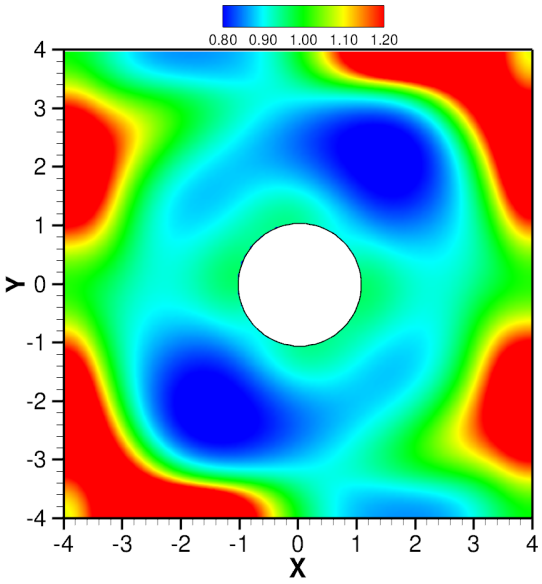

Figure 3.17: Density contour in Example 3.4.11. $h = 1/20$ and $t = 0.5$.

Table 3.9: Entropy errors in $[-3, 3] \times [-3, 3]$ and convergence rates in Example 3.4.11. $t = 0.5$.

h	L^1 error	Order	L^∞ error	Order
1/5	1.44E-03		5.67E-04	
1/10	5.00E-05	4.84	2.72E-05	4.38
1/20	8.66E-07	5.85	5.03E-07	5.76
1/40	2.26E-08	5.26	1.81E-08	4.80

Example 3.4.12. We start to consider problems involving detonations. It is a rapid regime of burning in which a strong shock ignites the combustible mixture of gases and the burning proceeds to equilibrium behind the shock, while the energy released continues to help to drive the shock [56]. The first problem is the reflection of detonation waves on a wedge, see [24, 66] for experiments and [49, 68] for numerical simulations. The computational domain is sketched in Figure 3.18(a). A Zeldovich, von Neumann and Doering (ZND) profile with $T^+ = 50$, $Q = 50$, $f = 1.0$, $\gamma = 1.2$ is initially located at $x = -118.2$. Here f is the overdrive factor defined by $f = D^2/D_{\rm CJ}^2$, where D is the detonation velocity and $D_{\rm CJ}$ is the velocity of the corresponding Chapman-Jouguet wave. The constant prestate is $(\rho, u, v, p, Y) = (1, 0, 0, 1, 1)$. See [6, 72] for details about the ZND profile. The density and pressure fields of this profile are perturbed so that the instability of the flow results in the development of triple points, whose trajectories form a cellular pattern [6, 18, 56]. The perturbation is in the region $[-117.0, -115.8] \times [0, 100]$ in which

$$\rho(x, y, 0) = p(x, y, 0) = \begin{cases} 1.8 & \text{if } y \in [20, 40] \cup [60, 80], \\ 0.2 & \text{otherwise.} \end{cases}$$

Supersonic inflow and outflow boundary conditions are used at $x = -120$ and at $x = 120$ respectively. The reflection technique is applied at $y = 0$ and at $y = 100$. Our fifth order boundary treatment in conservative variables with $q = 40$ in (3.34) is used at the surface of the wedge.

We first set the wedge angle $\theta = 19.3^\circ$. We run the code until $t = 28$ with $h = 0.15$. Figure 3.19(a) shows the cellular detonation pattern determined by recording the history of the maximum pressure. The cellular pattern is similar to the experimental results in Figures 5, 10, 11 of [24] and the numerical results in Figure 8 of [68]. From Figure 3.19(a), we can observe the main feature of the detonation

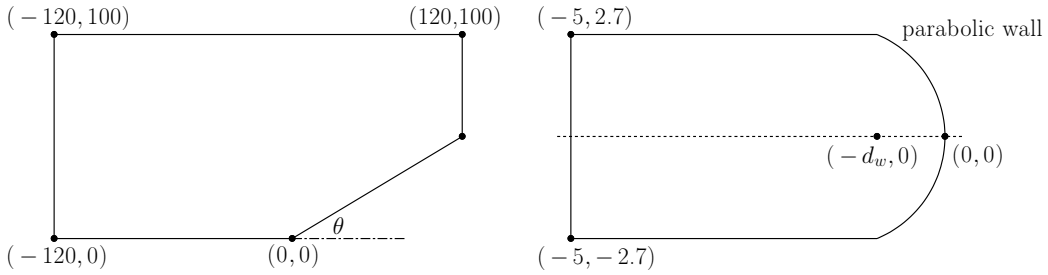

(a) Example 3.4.12 (b) Example 3.4.13

Figure 3.18: Left: Computational domain in Example 3.4.12. Right: Physical domain in Example 3.4.13. The computational domain is the upper half. Both are Illustrative sketches, not to scale.

wave reflection. There is a sharp dividing line, made up by a triple point trajectory, emerging near the tip of the wedge and extending downstream. The detonation cells below the line are smaller than those above the line and are distorted in shape.

Next, we increase the wedge angle to $\theta = 30^\circ$ and keep other parameters unchanged. The cellular pattern at $t = 30$ with $h = 0.15$ is shown in Figure 3.19(b). As the experimental results in Figure 1(d) of [66], Figure 7 of [24] and the numerical result in Figure 9 of [49], the cellular pattern is not clear in this case since the spatial scale of the region between the wedge and the reflection of transverse waves is small. However, the dividing line is still quite sharp.

Example 3.4.13. We consider the shock focusing problem. The physical domain is sketched in Figure 3.18(b). The curve represents a rigid wall with parabolic shape. A right-moving Mach 2.5 shock is initially positioned at $x = -d_w$, where d_w is the depth of the parabolic wall. The preshock state is $(\rho, u, v, p, Y) = (0.2, 0, 0, 0.2, 1)$. As the incident shock wave enters the cavity of the end-wall, there are local zones with elevated pressure and temperature. The formation of such hot zones causes self-ignition which is sometimes followed by detonation initiation. See [19] for experiments and [3] for numerical simulations.

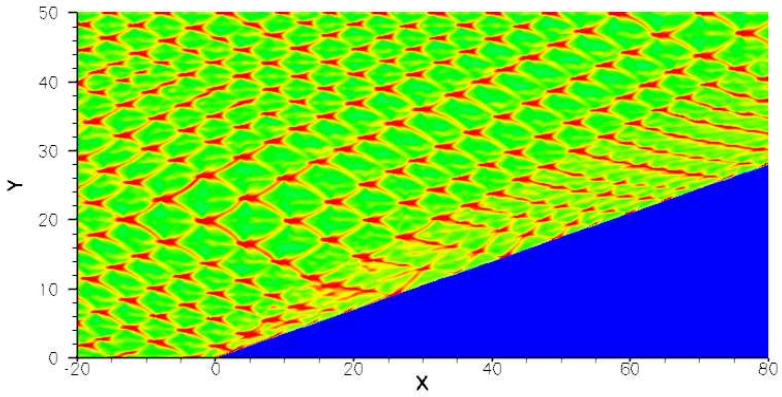

(a) $\theta = 19.3°$

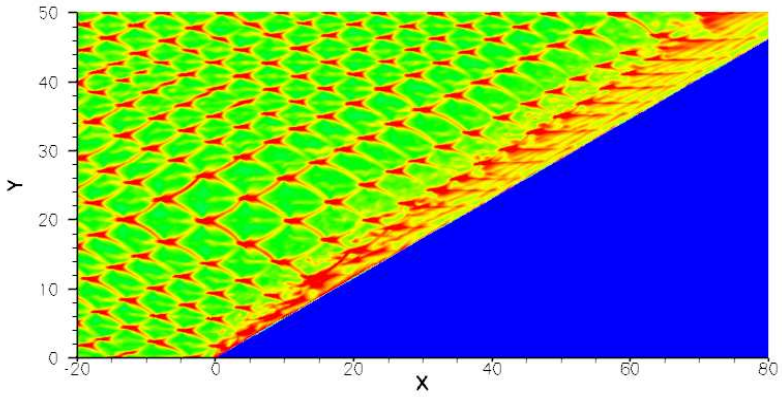

(b) $\theta = 30°$

Figure 3.19: Cellular patterns of detonation waves over a wedge of angle θ in Example 3.4.12.

We set $T^+ = 20$, $Q = 50$, and $K_c = 30$. The computational domain is the upper half of the physical domain due to the symmetry of this problem. The reflection technique is used at $y = 0$ and at $y = 2.7$. Supersonic inflow boundary condition is used at the left boundary $x = -5$. Our fifth order boundary treatment in primitive variables with $q = 40$ in (3.34) is applied at the parabolic wall.

In the first case, we consider a parabola $y^2 = -2.7x$ with $d_w = 2.7$. The temperature contours with $h = 1/160$ and $h = 1/320$ at different times are shown in Figure 3.20. At $t = 0.8$, a high temperature ignition zone is formed at the lateral surface near the Mach stem (see the top row of Figure 3.20), which shows that focusing induces exothermic reaction of combustible gases. The primary ignition starts and the developing detonation waves are focused around the center line (see the middle row). Similar structure persists until the detonation leaves the cavity of the end-wall (see the bottom row).

In the second case, we consider a shorter parabola $y^2 = -4.5x$ with $d_w = 1.62$. Other parameters are kept the same. The temperature contours with $h = 1/160$ and $h = 1/320$ at different times are shown in Figure 3.21. We again obtain convergent solutions with good resolutions.

3.5 Moving boundary treatment for compressible inviscid flows

The advantage of using *fixed* Cartesian mesh may best be shown by problems involving complex moving geometries. We consider Euler equations in moving geometries, i.e., the domain $\Omega(t)$ varies with time t. To describe the boundary conditions, we

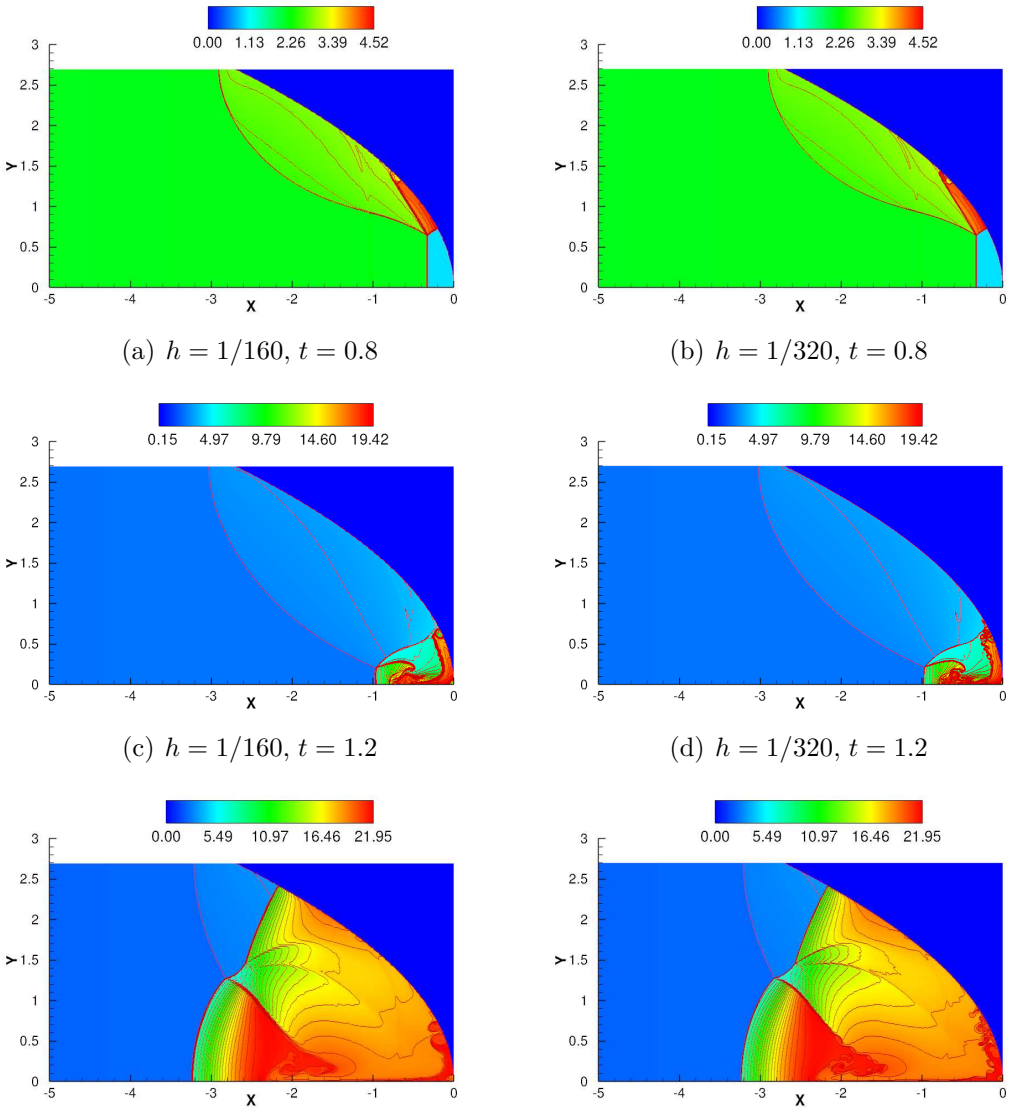

(a) $h = 1/160$, $t = 0.8$

(b) $h = 1/320$, $t = 0.8$

(c) $h = 1/160$, $t = 1.2$

(d) $h = 1/320$, $t = 1.2$

(e) $h = 1/160$, $t = 1.8$

(f) $h = 1/320$, $t = 1.8$

Figure 3.20: Temperature contours of the shock focusing problem in Example 3.4.13. 29 contour lines in the respective range. $d_w = 2.7$. The color outside the computational domain is not relevant.

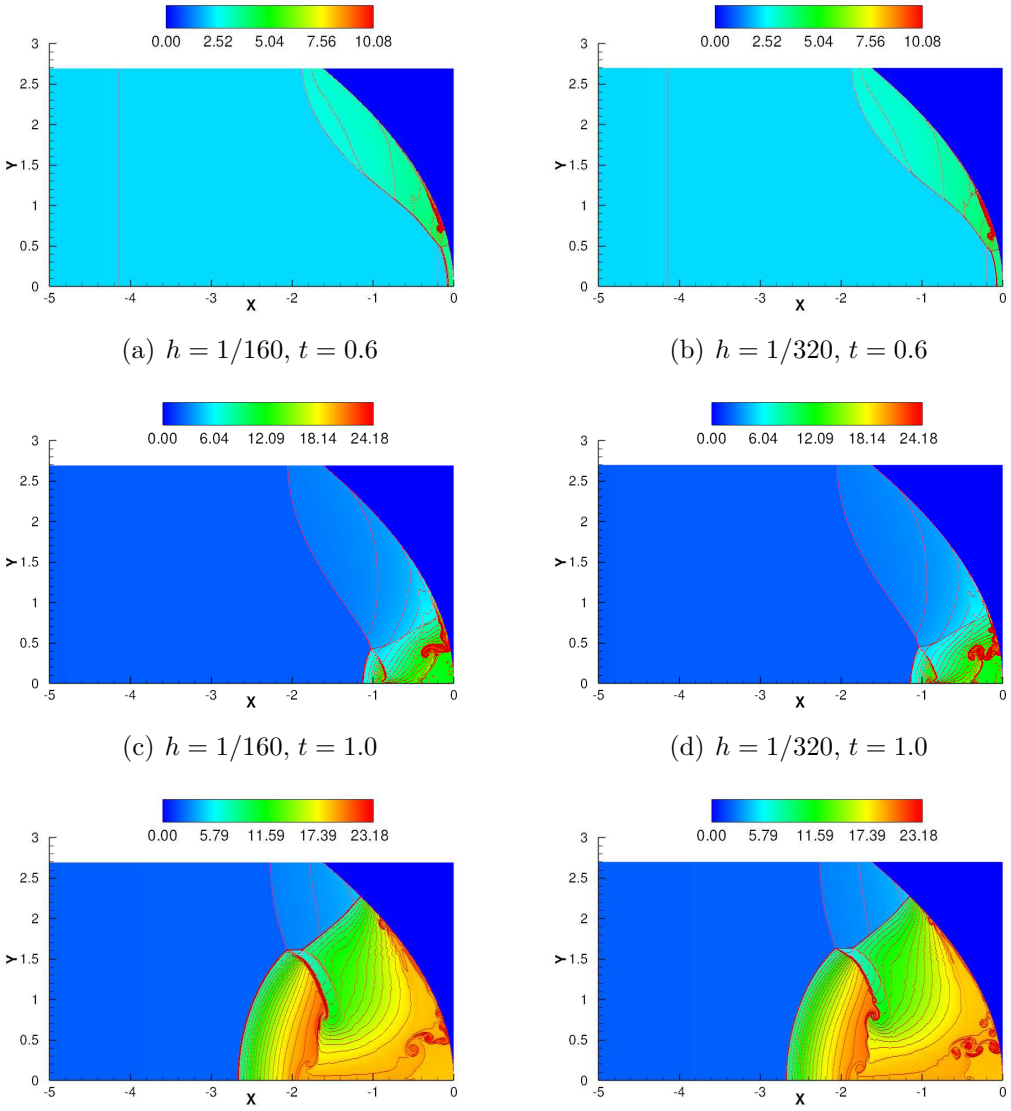

(a) $h = 1/160$, $t = 0.6$

(b) $h = 1/320$, $t = 0.6$

(c) $h = 1/160$, $t = 1.0$

(d) $h = 1/320$, $t = 1.0$

(e) $h = 1/160$, $t = 1.4$

(f) $h = 1/320$, $t = 1.4$

Figure 3.21: Temperature contours of the shock focusing problem in Example 3.4.13. 29 contour lines in the respective range. $d_w = 1.62$. The color outside the computational domain is not relevant.

let $\mathbf{X}_b(\mathbf{a}, t)$ represent the position vector (in Eulerian coordinates) of a point $\mathbf{a}$ on $\Gamma(t)$. Here $\mathbf{a}$ is the Lagrangian coordinate of the point determined by the condition $\mathbf{X}_b(\mathbf{a}, 0) = \mathbf{a}$. We mainly consider rigid bodies moving at a prescribed motion. Namely, $\mathbf{X}_b(\mathbf{a}, t)$ and thus $\Omega(t)$ are explicitly given. The no-penetration boundary condition for inviscid flows is then

$$\mathbf{u}(\mathbf{x}, t) \cdot \mathbf{n}(\mathbf{x}, t) = \mathbf{V}_b(t) \cdot \mathbf{n}(\mathbf{x}, t), \quad \text{for all } \mathbf{x} = \mathbf{X}_b(\mathbf{a}, t) \in \Gamma(t), \tag{3.43}$$

where $\mathbf{V}_b(t) = \frac{\partial \mathbf{X}_b}{\partial t}$ is the prescribed velocity. Notice that $\mathbf{V}_b(t)$ is independent of $\mathbf{a}$ for rigid bodies. The normal $\mathbf{n}(\mathbf{x}, t)$ is defined as the same way as in Figure 3.6. If the motion of a rigid body is induced by the fluid, the acceleration can be expressed as

$$\frac{\partial^2 \mathbf{X}_b}{\partial t^2} = -\frac{1}{M_b} \int_{\Gamma(t)} p\mathbf{n} ds, \tag{3.44}$$

where M_b is the rigid body mass. Although $\mathbf{X}_b(\mathbf{a}, t)$ is not explicitly given in this case, we can obtain it at each time level by integrating (3.44) in time.

There are two underlying issues with the moving boundary problem. First, the no-penetration condition (3.43) is prescribed in the Lagrangian specification of normal velocity. Thus in the ILW procedure we should use material derivatives of primitive variables, i.e., ρ, u, v, p, instead of Eulerian time derivatives of conservative variable $\mathbf{U}$. Secondly, in expansion flows there may be grid points which are outside $\Omega(t_{n-1})$ at the previous time level t_{n-1} but enter $\Omega(t_n)$ at the current time level t_n. Such grid points are called newly emerging points. The newly emerging points do not have any value at time level t_n. To update their values to time level t_{n+1}, we not only need to construct their values at time level t_n, but also need one extra ghost point in each direction if we assume $\Gamma(t)$ travels a distance of at most h

in each direction from t_n to t_{n+1}, i.e.,

$$\Delta t < \frac{h}{\max_{t\in[t_n,t_{n+1}]} \|\mathbf{V}_b(t)\|_\infty}. \tag{3.45}$$

See Figure 3.22 for a demonstration of newly emerging points and ghost points. If the same method is used to construct values of ghost points and newly emerging points, there is actually no need to distinguish them in implementation. We only need to construct values of four ghost points (instead of three ghost points for the static boundary problem) in each direction at time level t_n.

We start to describe a fifth order boundary treatment for the no-penetration boundary condition (3.43) in which $\mathbf{X}_b(\mathbf{a}, t)$ and thus $\mathbf{V}_b(t)$ are prescribed.

3.5.1 1D problems

We assume the right boundary is a moving rigid wall with prescribed position $X_b(t)$ and velocity $V_b(t) = X_b'(t)$. Since the boundary condition (3.43) is prescribed in velocity u, we rewrite the Euler equations in terms of primitive variables

$$\mathbf{W}_t + \mathbf{A}(\mathbf{W})\mathbf{W}_x = 0, \tag{3.46}$$

where

$$\mathbf{W} = \begin{pmatrix} W_1 \\ W_2 \\ W_3 \end{pmatrix} = \begin{pmatrix} \rho \\ u \\ p \end{pmatrix}, \quad \mathbf{A}(\mathbf{W}) = \begin{pmatrix} u & \rho & 0 \\ 0 & u & 1/\rho \\ 0 & \rho c^2 & u \end{pmatrix}.$$

At time level $t = t_n$, we have grid points $x_0 < \ldots < x_{N-3} < x_{N-2} < x_{N-1} < x_N < X_b(t_n) \le x_{N+1} < x_{N+2} < x_{N+3}$. We assume $x_N, \ldots, x_{N+3}$ are the four ghost

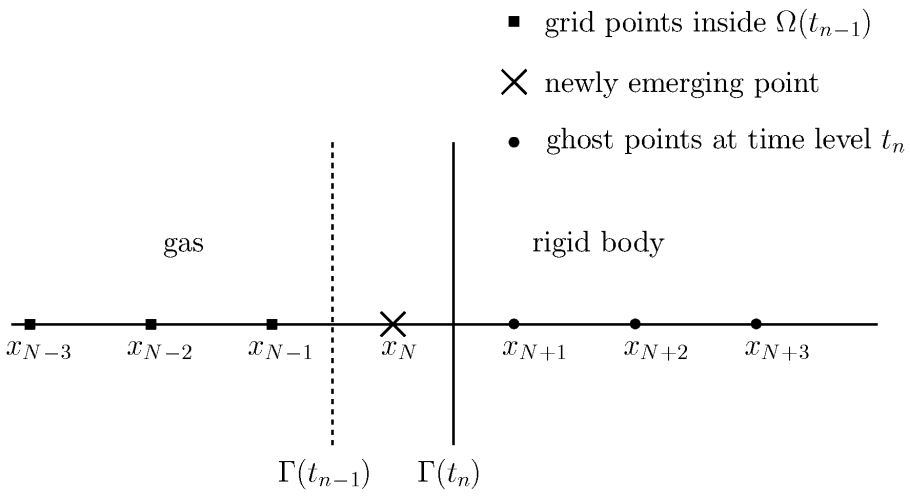

(a) 1D

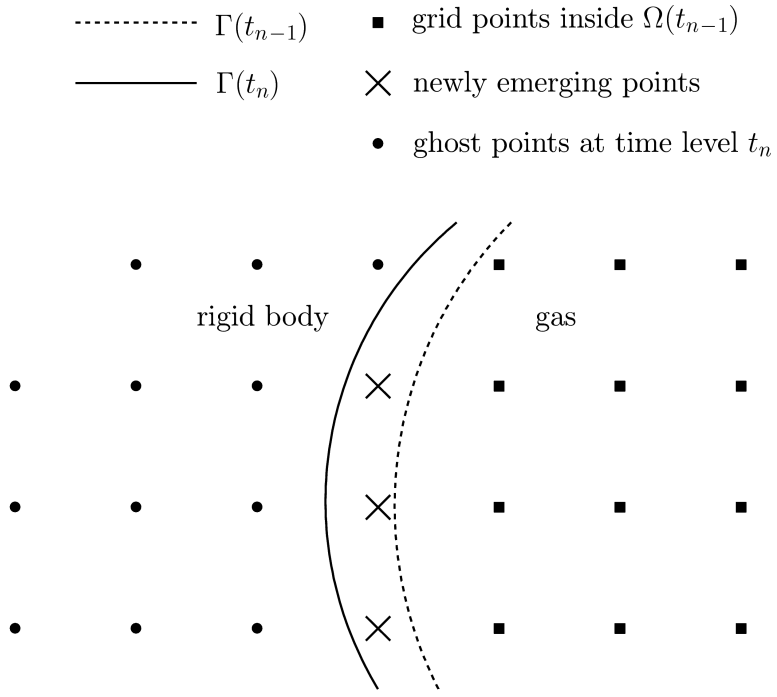

(b) 2D

Figure 3.22: Newly emerging points and ghost points at time level t_n.

points in which x_N is a newly emerging point, i.e., $X_b(t_{n-1}) < x_N < X_b(t_n)$, see Figure 3.22(a). $\mathbf{W}_1, \ldots, \mathbf{W}_{N-1}$ have been updated from time level t_{n-1} to time level t_n. We would like to construct values of ghost points $\mathbf{W}_N, \ldots, \mathbf{W}_{N+3}$ by a fourth order Taylor expansion

$$(W_m)_j = \sum_{k=0}^{4} \frac{(x_j - X_b(t_n))^k}{k!} W_m^{*(k)}, \quad m = 1, 2, 3, \quad j = N, \ldots, N+3, \tag{3.47}$$

where $W_m^{*(k)}$ is a $(5-k)$th order approximation of the spatial derivative $\frac{\partial^k W_m}{\partial x^k}\Big|_{x=X_b(t_n),\ t=t_n}$.

We first do a local characteristic decomposition of the PDEs near the boundary $x = X_b(t_n)$. $\mathbf{A}(\mathbf{W}_{N-1})$ has three eigenvalues $\lambda_{N-1} = u_{N-1} - c_{N-1}$, $\lambda_2 = u_{N-1}$, $\lambda_3 = u_{N-1} + c_{N-1}$ and a complete set of left eigenvectors $\mathbf{l}_m(\mathbf{W}_{N-1})$, $m = 1, 2, 3$, which forms a left eigenmatrix

$$\mathbf{L}(\mathbf{W}_{N-1}) = \begin{pmatrix} \mathbf{l}_1(\mathbf{W}_{N-1}) \\ \mathbf{l}_2(\mathbf{W}_{N-1}) \\ \mathbf{l}_3(\mathbf{W}_{N-1}) \end{pmatrix} = \begin{pmatrix} l_{1,1} & l_{1,2} & l_{1,3} \\ l_{2,1} & l_{2,2} & l_{2,3} \\ l_{3,1} & l_{3,2} & l_{3,3} \end{pmatrix}.$$

The local characteristic variables V_m at grid points near the boundary are defined by

$$(V_m)_j = \mathbf{l}_m(\mathbf{W}_{N-1})\mathbf{W}_j, \quad m = 1, 2, 3, \quad j = N-5, \ldots, N-1. \tag{3.48}$$

Both V_2 and V_3 can be considered as outgoing, since their relative speeds to the moving boundary are approximately 0 and $c_{N-1} > 0$ respectively. We extrapolate $(V_m)_j$, $m = 1, 2, 3$, to $x = X_b(t_n)$ with the fifth order WENO type extrapolation. The extrapolated kth order derivative of V_m at the boundary is denoted by $V_m^{*(k)}$, $k = 0, \ldots, 4$. $W_2^{*(0)}$ can be naturally imposed by $W_2^{*(0)} = V_b(t_n) = X_b'(t_n)$ according to (3.43). The other two components, $W_1^{*(0)}$ and $W_3^{*(0)}$, should be obtained by

extrapolated values $V_m^{*(0)}$. We have a linear system with $W_m^{*(0)}$ as unknowns

$$\begin{pmatrix} 0 & 1 & 0 \\ l_{2,1} & l_{2,2} & l_{2,3} \\ l_{3,1} & l_{3,2} & l_{3,3} \end{pmatrix} \begin{pmatrix} W_1^{*(0)} \\ W_2^{*(0)} \\ W_3^{*(0)} \end{pmatrix} = \begin{pmatrix} X_b'(t_n) \\ V_2^{*(0)} \\ V_3^{*(0)} \end{pmatrix}. \tag{3.49}$$

Next we try to find the spatial derivatives $W_m^{*(1)}$ with the ILW procedure for u, together with the extrapolation of V_m, $m = 2, 3$. The second equation of (3.46) can be written in Lagrangian form as

$$\frac{Du}{Dt} + \frac{1}{\rho} p_x = 0,$$

where $\frac{D}{Dt} = \frac{\partial}{\partial t} + u\frac{\partial}{\partial x}$ is the material derivative. Thus the material derivative of u, which is actually $X_b''(t_n)$, can be converted to the spatial derivative p_x at the boundary. We then have a linear system with $W_m^{*(1)}$ as unknowns

$$\begin{pmatrix} 0 & 0 & -\frac{1}{W_1^{*(0)}} \\ l_{2,1} & l_{2,2} & l_{2,3} \\ l_{3,1} & l_{3,2} & l_{3,3} \end{pmatrix} \begin{pmatrix} W_1^{*(1)} \\ W_2^{*(1)} \\ W_3^{*(1)} \end{pmatrix} = \begin{pmatrix} X_b''(t_n) \\ V_2^{*(1)} \\ V_3^{*(1)} \end{pmatrix}. \tag{3.50}$$

Higher order derivatives $W_m^{*(k)}$, $k = 2, 3, 4$, are obtained by extrapolation

$$\mathbf{L}(\mathbf{W}_{N-1}) \begin{pmatrix} W_1^{*(k)} \\ W_2^{*(k)} \\ W_3^{*(k)} \end{pmatrix} = \begin{pmatrix} V_1^{*(k)} \\ V_2^{*(k)} \\ V_3^{*(k)} \end{pmatrix}. \tag{3.51}$$

Notice that the numerical method we have described so far is for time level t_n only. We need to match the time levels when constructing values of ghost points in

the two intermediate stages $\mathbf{U}_j^{(1)}$ and $\mathbf{U}_j^{(2)}$ of the RK method (2.8). The traditional match of time $\mathbf{U}_j^{(1)} \sim t_{n+1}$, $\mathbf{U}_j^{(2)} \sim t_n + \Delta t/2$ decreases the accuracy to second order [9]. One idea is to update the position X_b and the velocity V_b at each RK stage by (2.8)

$$\begin{aligned} X_b^{(1)} &= X_b(t_n) + \Delta t X_b'(t_n), \\ V_b^{(1)} &= X_b'(t_n) + \Delta t X_b''(t_n); \end{aligned}$$

$$\begin{aligned} X_b^{(2)} &= \frac{3}{4} X_b(t_n) + \frac{1}{4} X_b^{(1)} + \frac{1}{4}\Delta t V_b^{(1)} \\ &= X_b(t_n) + \frac{1}{2}\Delta t X_b'(t_n) + \frac{1}{4}\Delta t^2 X_b''(t_n), \\ V_b^{(2)} &= X_b'(t_n) + \frac{1}{2}\Delta t X_b''(t_n) + \frac{1}{4}\Delta t^2 X_b'''(t_n). \end{aligned}$$

The updated positions $X_b^{(i)}$ and velocities $V_b^{(i)}$, $i = 1, 2$, instead of $X_b(t_n)$ and $X_b'(t_n)$, are used in the two intermediate stages. This time matching technique successfully maintains third order accuracy in Lagrangian type schemes [10]. However, it is only second order accurate if applied here. The reason is probably that our mesh does not move with the fluid.

According to (3.3), we can achieve third order accuracy by the following match of time

$$u^{(1)} \sim X_b'(t_n) + \Delta t \left.\frac{\partial u}{\partial t}\right|_{x=X_b(t_n),\ t=t_n}, \tag{3.52}$$

$$u^{(2)} \sim X_b'(t_n) + \frac{1}{2}\Delta t \left.\frac{\partial u}{\partial t}\right|_{x=X_b(t_n),\ t=t_n} + \frac{1}{4}\Delta t^2 \left.\frac{\partial^2 u}{\partial t^2}\right|_{x=X_b(t_n),\ t=t_n}. \tag{3.53}$$

The Eulerian time derivatives can be obtained by a standard Lax-Wendroff procedure, since all the necessary spatial derivatives have been obtained at time level t_n.

The expressions are

$$\frac{\partial u}{\partial t} = -u\frac{\partial u}{\partial x} - \frac{1}{\rho}\frac{\partial p}{\partial x}, \tag{3.54}$$

$$\frac{\partial^2 u}{\partial t^2} = -\frac{\partial u}{\partial t}\frac{\partial u}{\partial x} - u\frac{\partial^2 u}{\partial x \partial t} + \frac{1}{\rho^2}\frac{\partial \rho}{\partial t}\frac{\partial p}{\partial x} - \frac{1}{\rho}\frac{\partial^2 p}{\partial x \partial t}, \tag{3.55}$$

where

$$\begin{aligned}
\frac{\partial^2 u}{\partial x \partial t} &= -\left(\frac{\partial u}{\partial x}\right)^2 - u\frac{\partial^2 u}{\partial x^2} + \frac{1}{\rho^2}\frac{\partial \rho}{\partial x}\frac{\partial p}{\partial x} - \frac{1}{\rho}\frac{\partial^2 p}{\partial x^2}, \\
\frac{\partial \rho}{\partial t} &= -u\frac{\partial \rho}{\partial x} - \rho\frac{\partial u}{\partial x}, \\
\frac{\partial^2 p}{\partial x \partial t} &= -(\gamma+1)\frac{\partial p}{\partial x}\frac{\partial u}{\partial x} - \gamma p\frac{\partial^2 u}{\partial x^2} - u\frac{\partial^2 p}{\partial x^2}.
\end{aligned}$$

Our ILW procedure should also be adjusted in the two intermediate RK stages. We write spatial derivatives in terms of Eulerian time derivatives instead of material derivatives. For example, the first equation of (3.50) is replaced by

$$-W_2^{*(0)}W_2^{*(1)} - \frac{1}{W_1^{*(0)}}W_3^{*(1)} = \left.\frac{\partial u}{\partial t}\right|_{x=X_b(t_n),\ t=t_n} + \Delta t \left.\frac{\partial^2 u}{\partial t^2}\right|_{x=X_b(t_n),\ t=t_n} \tag{3.56}$$

in the first stage; replaced by

$$-W_2^{*(0)}W_2^{*(1)} - \frac{1}{W_1^{*(0)}}W_3^{*(1)} = \left.\frac{\partial u}{\partial t}\right|_{x=X_b(t_n),\ t=t_n} + \frac{\Delta t}{2}\left.\frac{\partial^2 u}{\partial t^2}\right|_{x=X_b(t_n),\ t=t_n} \tag{3.57}$$

in the second stage.

Here we summarize our algorithm. We assume $\mathbf{W}_1, \ldots, \mathbf{W}_{N-1}$ have been updated from time level t_{n-1} to time level t_n. Our goal is to impose values of ghost points $\mathbf{W}_N, \ldots, \mathbf{W}_{N+3}$ at time level t_n and at the two intermediate RK stages.

For time level t_n:

1. Do a local characteristic decomposition of the Euler equations (3.46). Form the characteristic variables $(V_m)_j$, $m = 1, 2, 3$, $j = N-5, \ldots, N-1$, as in (3.48). Extrapolate $(V_m)_j$ to the boundary to obtain $V_m^{*(k)}$, $k = 0, \ldots, 4$, with the WENO type extrapolation. Solve for $W_m^{*(0)}$, $m = 1, 2, 3$, in (3.49).

2. Use the ILW procedure with material derivatives and the extrapolation equations to form linear system (3.50). Solve for $W_m^{*(1)}$, $m = 1, 2, 3$.

3. For $k = 2, 3, 4$, form linear system (3.51). Solve for $W_m^{*(k)}$, $m = 1, 2, 3$.

4. Use the standard Lax-Wendroff procedure (3.54) and (3.55) to compute $\frac{\partial u}{\partial t}$ and $\frac{\partial^2 u}{\partial t^2}$ at the boundary respectively.

5. Impose the values of the ghost points by the Taylor expansion (3.47).

For the first and second intermediate RK stages:

6. Do Step 1 but replace $X_b'(t_n)$ in (3.49) by the right-hand side of (3.52) and (3.53) respectively.

7. Form linear system (3.50) but replace the first equation by (3.56) and (3.57) respectively. Solve for $W_m^{*(1)}$, $m = 1, 2, 3$.

8. Do Step 3 and then do Step 5.

3.5.2 2D problems

We assume the values of all the grid points inside $\Omega(t_{n-1})$ have been updated by the interior scheme from time level t_{n-1} to time level t_n. At time level t_n, we set up the local coordinate system (3.24) with origin $P_0 = \mathbf{x}_0$ for each ghost point $P = (x_i, y_j)$.

In this local coordinate system, the Euler equations are written in terms of primitive variable as

$$\frac{\partial \hat{\mathbf{W}}}{\partial t} + \mathbf{A}(\hat{\mathbf{W}})\frac{\partial \hat{\mathbf{W}}}{\partial \hat{x}} + \mathbf{B}(\hat{\mathbf{W}})\frac{\partial \hat{\mathbf{W}}}{\partial \hat{y}} = 0, \tag{3.58}$$

where

$$\hat{\mathbf{W}} = \begin{pmatrix} \hat{W}_1 \\ \hat{W}_2 \\ \hat{W}_3 \\ \hat{W}_4 \end{pmatrix} = \begin{pmatrix} \rho \\ \hat{u} \\ \hat{v} \\ p \end{pmatrix}, \ \mathbf{A}(\hat{\mathbf{W}}) = \begin{pmatrix} \hat{u} & \rho & 0 & 0 \\ 0 & \hat{u} & 0 & \frac{1}{\rho} \\ 0 & 0 & \hat{u} & 0 \\ 0 & \rho c^2 & 0 & \hat{u} \end{pmatrix}, \ \mathbf{B}(\hat{\mathbf{W}}) = \begin{pmatrix} \hat{v} & 0 & \rho & 0 \\ 0 & \hat{v} & 0 & 0 \\ 0 & 0 & \hat{v} & \frac{1}{\rho} \\ 0 & 0 & \rho c^2 & \hat{v} \end{pmatrix}.$$

Our ILW procedure is carried out by the use of (3.58).

For a fifth order boundary treatment, the value of the ghost point $P = (x_i, y_j)$ is imposed by the Taylor expansion

$$(\hat{W}_m)_{i,j} = \sum_{k=0}^{4} \frac{\Delta^k}{k!} \hat{W}_m^{*(k)}, \quad m = 1, \ldots, 4, \tag{3.59}$$

where Δ is the $\hat{x}$-coordinate of P and $\hat{W}_m^{*(k)}$ is a $(5-k)$th order approximation of the normal derivative $\left.\frac{\partial^k \hat{W}_m}{\partial \hat{x}^k}\right|_{(x,y)=\mathbf{x}_0,\ t=t_n}$. We assume $\hat{\mathbf{W}}_0$ is the value of a grid point nearest to P_0 among all the grid points inside $\Omega(t_{n-1})$. $\mathbf{A}(\hat{\mathbf{W}}_0)$ has four eigenvalues $\lambda_1 = \hat{u}_0 - c_0$, $\lambda_2 = \lambda_3 = \hat{u_0}$, $\lambda_4 = \hat{u}_0 + c_0$ and a complete set of left eigenvectors

$\mathbf{l}_m(\hat{\mathbf{W}}_0)$, $m = 1, \ldots, 4$, which forms a left eigenmatrix

$$\mathbf{L}(\hat{\mathbf{W}}_0) = \begin{pmatrix} \mathbf{l}_1(\hat{\mathbf{W}}_0) \\ \mathbf{l}_2(\hat{\mathbf{W}}_0) \\ \mathbf{l}_3(\hat{\mathbf{W}}_0) \\ \mathbf{l}_4(\hat{\mathbf{W}}_0) \end{pmatrix} = \begin{pmatrix} l_{1,1} & l_{1,2} & l_{1,3} & l_{1,4} \\ l_{2,1} & l_{2,2} & l_{2,3} & l_{2,4} \\ l_{3,1} & l_{3,2} & l_{3,3} & l_{3,4} \\ l_{4,1} & l_{4,2} & l_{4,3} & l_{4,4} \end{pmatrix}.$$

The characteristic variables V_m, $m = 1, \ldots, 4$, at grid points near P_0 can be defined by

$$(V_m)_{\mu,\nu} = \mathbf{l}_m(\hat{\mathbf{W}}_0)\hat{\mathbf{W}}_{\mu,\nu}, \quad m = 1, \ldots, 4, \quad (x_\mu, y_\nu) \in \mathcal{E}_{i,j}, \tag{3.60}$$

where $\mathcal{E}_{i,j} \subset \Omega(t_{n-1})$ is a set of grid points used for extrapolation. We extrapolate $(V_m)_{\mu,\nu}$ to P_0 and denote the extrapolated kth order $\hat{x}$-derivative of V_m by $V_m^{*(k)}$, $k = 0, \ldots, 4$. The constant term $\hat{W}_m^{*(0)}$, $m = 1, \ldots, 4$, is solved by a linear system of equations

$$\begin{pmatrix} 0 & 1 & 0 & 0 \\ l_{2,1} & l_{2,2} & l_{2,3} & l_{2,4} \\ l_{3,1} & l_{3,2} & l_{3,3} & l_{3,4} \\ l_{4,1} & l_{4,2} & l_{4,3} & l_{4,4} \end{pmatrix} \begin{pmatrix} \hat{W}_1^{*(0)} \\ \hat{W}_2^{*(0)} \\ \hat{W}_3^{*(0)} \\ \hat{W}_4^{*(0)} \end{pmatrix} = \begin{pmatrix} \mathbf{V}_b(t_n) \cdot \mathbf{n}(\mathbf{x}_0, t_n) \\ V_2^{*(0)} \\ V_3^{*(0)} \\ V_4^{*(0)} \end{pmatrix}. \tag{3.61}$$

Next, we take the first material derivative $\frac{D}{Dt} = \frac{\partial}{\partial t} + \hat{u}\frac{\partial}{\partial \hat{x}} + \hat{v}\frac{\partial}{\partial \hat{y}}$ of (3.43) and obtain

$$\frac{D\hat{u}}{Dt} + \hat{\mathbf{u}} \cdot \frac{D\mathbf{n}}{Dt} = \frac{d}{dt}\left(\mathbf{V}_b \cdot \mathbf{n}\right),$$

where $\hat{\mathbf{u}} = (\hat{u}, \hat{v})^T$. Converting the material derivative $\frac{D\hat{u}}{Dt}$ to spatial derivatives by the second equation of (3.58), we have

$$\frac{\partial p}{\partial \hat{x}} = \rho\left[\hat{\mathbf{u}} \cdot \frac{D\mathbf{n}}{Dt} - \frac{d}{dt}\left(\mathbf{V}_b \cdot \mathbf{n}\right)\right].$$

The right-hand side of the above equation is already known if evaluated at P_0. As a result, $\hat{W}_m^{*(1)}$, $m = 1, \ldots, 4$, can be solved by

$$\begin{pmatrix} 0 & 0 & 0 & 1 \\ l_{2,1} & l_{2,2} & l_{2,3} & l_{2,4} \\ l_{3,1} & l_{3,2} & l_{3,3} & l_{3,4} \\ l_{4,1} & l_{4,2} & l_{4,3} & l_{4,4} \end{pmatrix} \begin{pmatrix} \hat{W}_1^{*(1)} \\ \hat{W}_2^{*(1)} \\ \hat{W}_3^{*(1)} \\ \hat{W}_4^{*(1)} \end{pmatrix} = \mathbf{b}, \tag{3.62}$$

where

$$\mathbf{b} = \begin{pmatrix} \hat{W}_1^{*(0)} \left[\left(\hat{W}_2^{*(0)}, \hat{W}_3^{*(0)} \right)^T \cdot \frac{D\mathbf{n}}{Dt} - \frac{d}{dt} \left(\mathbf{V}_b \cdot \mathbf{n} \right) \right] \Big|_{(x,y)=\mathbf{x}_0,\ t=t_n} \\ V_2^{*(1)} \\ V_3^{*(1)} \\ V_4^{*(1)} \end{pmatrix}.$$

Higher order spatial derivatives $\hat{W}_m^{*(k)}$, $k = 2, 3, 4$, can be obtained by extrapolation

$$\mathbf{L}(\hat{\mathbf{W}}_0) \begin{pmatrix} \hat{W}_1^{*(k)} \\ \hat{W}_2^{*(k)} \\ \hat{W}_3^{*(k)} \\ \hat{W}_4^{*(k)} \end{pmatrix} = \begin{pmatrix} V_1^{*(k)} \\ V_2^{*(k)} \\ V_3^{*(k)} \\ V_4^{*(k)} \end{pmatrix}. \tag{3.63}$$

We have finished describing our approach for the time level t_n. For the two intermediate RK stages, we follow the same time matching technique as for 1D problems.

We now summarize our fifth order boundary treatment for the boundary condition (3.43) in 2D with a prescribed boundary motion. We assume the values of all

the grid points inside $\Omega(t_{n-1})$ have been updated by the interior scheme from time level t_{n-1} to time level t_n. Our goal is to impose the value of $(\hat{W}_m)_{i,j}$, $m = 1, \ldots, 4$, for each ghost point (x_i, y_j) at time level $t = t_n$ and at the intermediate RK stages.

For time level t_n:

1. Decide the local coordinate system (3.24). Do a local characteristic decomposition of the Euler equations (3.58). Form the characteristic variables $(V_m)_{\mu,\nu}$, $m = 1, \ldots, 4$, $(\mu, \nu) \in \mathcal{E}_{i,j}$, as in (3.60). Extrapolate $(V_m)_{\mu,\nu}$ to the boundary to obtain $V_m^{*(k)}$, $k = 0, \ldots, 4$, with WENO type extrapolation. Solve for $\hat{W}_m^{*(0)}$, $m = 1, \ldots, 4$, in (3.61).

2. Use the ILW procedure with material derivatives and the extrapolation equations to form linear system (3.62). Solve for $\hat{W}_m^{*(1)}$, $m = 1, \ldots, 4$.

3. For $k = 2, 3, 4$, solve for $\hat{W}_m^{*(k)}$, $m = 1, \ldots, 4$, in (3.63).

4. Use a standard Lax-Wendroff procedure to compute $\frac{\partial \hat{u}}{\partial t}\Big|_{(x,y)=P_0,\ t=t_n}$ and $\frac{\partial^2 \hat{u}}{\partial t^2}\Big|_{(x,y)=P_0,\ t=t_n}$.

5. Impose the values of the ghost points by the Taylor expansion (3.59).

For the first and second intermediate RK stages:

6. Do Step 1 but replace $\mathbf{V}_b(t_n) \cdot \mathbf{n}(\mathbf{x}_0, t_n)$ in (3.61) by

$$\mathbf{V}_b(t_n) \cdot \mathbf{n}(\mathbf{x}_0, t_n) + \Delta t \frac{\partial \hat{u}}{\partial t}\bigg|_{(x,y)=P_0,\ t=t_n}$$

and

$$\mathbf{V}_b(t_n)\cdot\mathbf{n}(\mathbf{x}_0,t_n)+\frac{\Delta t}{2}\frac{\partial\hat{u}}{\partial t}\bigg|_{(x,y)=P_0,\ t=t_n}+\frac{\Delta t^2}{4}\frac{\partial^2\hat{u}}{\partial t^2}\bigg|_{(x,y)=P_0,\ t=t_n}, \tag{3.64}$$

respectively.

7. Form linear system (3.62) but replace the first equation by

$$-\hat{W}_2^{*(0)}\hat{W}_2^{*(1)}-\frac{\hat{W}_4^{*(1)}}{\hat{W}_1^{*(0)}}=\frac{\partial\hat{u}}{\partial t}\bigg|_{(x,y)=P_0,\ t=t_n}+\Delta t\frac{\partial^2\hat{u}}{\partial t^2}\bigg|_{(x,y)=P_0,\ t=t_n}+\hat{W}_3^{*(0)}\frac{\partial\hat{u}}{\partial\hat{y}}$$

and

$$-\hat{W}_2^{*(0)}\hat{W}_2^{*(1)}-\frac{\hat{W}_4^{*(1)}}{\hat{W}_1^{*(0)}}=\frac{\partial\hat{u}}{\partial t}\bigg|_{(x,y)=P_0,\ t=t_n}+\frac{\Delta t}{2}\frac{\partial^2\hat{u}}{\partial t^2}\bigg|_{(x,y)=P_0,\ t=t_n}+\hat{W}_3^{*(0)}\frac{\partial\hat{u}}{\partial\hat{y}},$$

respectively. Solve for $\hat{W}_m^{*(1)}$, $m=1,\ldots,4$.

8. Do Step 3 and then do Step 5.

If the motion of a rigid body is not prescribed but induced by the fluid, our algorithm should be adjusted as follows. Before Step 2, we compute $\frac{d\mathbf{V}_b}{dt}=\frac{\partial^2\mathbf{X}_b}{\partial t^2}$ by (3.44), since we have obtained pressure p at P_0 on $\Gamma(t_n)$ for all the ghost points. The integral in (3.44) can be calculated by the trapezoidal rule, for example. Notice that integrating (3.44) in time by the RK method (2.8), we can obtain $\mathbf{X}_b(\mathbf{a},t_{n+1})$ and $\mathbf{V}_b(t_{n+1})$ so that our algorithm can be continued at next time level t_{n+1}.

We finally remark that the boundary treatment for moving geometries can clearly be applied to static geometries as well. This provides an alternative to the method developed in Section 3.4.

3.5.3 Numerical examples

In this section, we show some numerical examples to demonstrate that our fifth order boundary treatment is indeed high order accurate for moving geometries. Our method also performs well for problems involving interactions between shocks and moving rigid bodies. For accuracy tests, we take $\Delta t = O(h^{5/3})$ in the third order RK time integration (2.8) in order to have fifth order accuracy in time. For other cases, we take $\Delta t = O(h)$ and the CFL number as 0.6, unless otherwise indicated. (3.45) is implied by the CFL conditions in all our examples. The specific heat ratio γ in Euler equations is taken as $\gamma = 1.4$ and the power q in (3.15) or (3.34) is taken as $q = 3$, unless otherwise indicated. The L^1 error and L^∞ error are defined as $h^2 \sum_{\{(i,j):(x_i,y_j)\in\mathcal{D}\}} |e_{i,j}|$ and $\max_{\{(i,j):(x_i,y_j)\in\mathcal{D}\}} |e_{i,j}|$ respectively. Here $e_{i,j}$ denotes the pointwise error and $\mathcal{D}$ is the region where the errors are measured. $\mathcal{D} = \Omega(t)$ unless otherwise indicated.

Example 3.5.1. We consider a gas confined between two rigid walls. The right wall is fixed at $x_r = 1.0$ while the left wall is moving. We assume the left wall is positioned at $x_l(t)$. The initial conditions are

$$\begin{aligned} \rho(x,0) &= 1 + 0.2\cos\left[2\pi\left(x - 0.5\right)\right], \\ u(x,0) &= x - 1, \\ p(x,0) &= \rho(x,0)^\gamma, \end{aligned}$$

such that the initial entropy $s(x,0) = 1$. Here $\gamma = 1.4$ is the specific heat ratio. As long as the solution stays smooth, we have isentropic flow, i.e., $s(x,t) = 1$. Thus the numerical value of the entropy can be used for the analysis of convergence. This example is considered by Forrer et al. [16] and later by Arienti et al. [2] and Hu et al. [30]. Second order convergence in total entropy is reported in all three papers.

However, the error of the entropy at the left moving wall falls short of second order in [2, 30].

In our first case, we set $x_l(t) = 0.5(1-t)$ such that the wall moves with a constant speed. Our fifth order boundary treatment is used at the left moving boundary while the standard reflection technique is used at the right fixed boundary. We measure the L^1 errors and L^∞ errors in entropy at $t = 0.5$. We can see from the left part of Table 3.10 that our method achieves the designed fifth order accuracy even near the moving boundary.

Table 3.10: Entropy errors and convergence rates in Example 3.5.1. $t = 0.5$.

h	$x_l(t) = 0.5(1-t)$				$x_l(t) = 0.5(1-\sin t)$			
	L^1 error	order	L^∞ error	order	L^1 error	order	L^∞ error	order
1/40	7.47E-07		1.24E-06		7.31E-07		1.35E-06	
1/80	1.17E-08	5.99	2.88E-08	5.43	1.16E-08	5.98	2.82E-08	5.59
1/160	3.49E-10	5.07	6.36E-10	5.50	3.45E-10	5.07	6.19E-10	5.51
1/320	9.55E-12	5.19	1.72E-11	5.21	9.88E-12	5.12	3.67E-11	4.08

In our second case, we set $x_l(t) = 0.5(1-\sin t)$. Now the speed of the wall varies in time. The right part of Table 3.10 shows the entropy errors at $t = 0.5$. We can see that we still achieve the designed fifth order accuracy in the L^1 norm. However, the convergence rate of L^∞ errors decays to fourth order on refined meshes.

Example 3.5.2. This is a 1D problem involving shocks and rarefaction waves. A piston with width $10h$ is initially centered at $x = -5h$ inside a shock tube. The piston instantaneously moves with a constant velocity $u_p = 2$ into an initially quiescent fluid with $\rho = 1$ and $p = 5/7$. This problem is equivalent to two independent Riemann problems and thus the exact solution can be obtained [42]. A shock forms ahead of the piston and a rarefaction wave forms in the rear. A 3D version of this problem is considered by Murman et al. [48]. Shyue [62] tests a 2D moving piston problem with a different Mach number. We take $h = 0.25$, the same mesh size as in [48], and set

the CFL number to be 0.5. The density and pressure profiles at $t = 11$ are plotted in Figure 3.23, together with the exact solution. Our approach predicts the correct shock location on this relatively coarse mesh, indicating that the mass, momentum, and energy loss through the piston is quite small. Moreover, our numerical density does not suffer from the undershoot just ahead of the piston which appears in Figure 10(a) of [48] and in Figure 3 of [62]. The numerical solution of the rarefaction wave also agrees well with the exact solution.

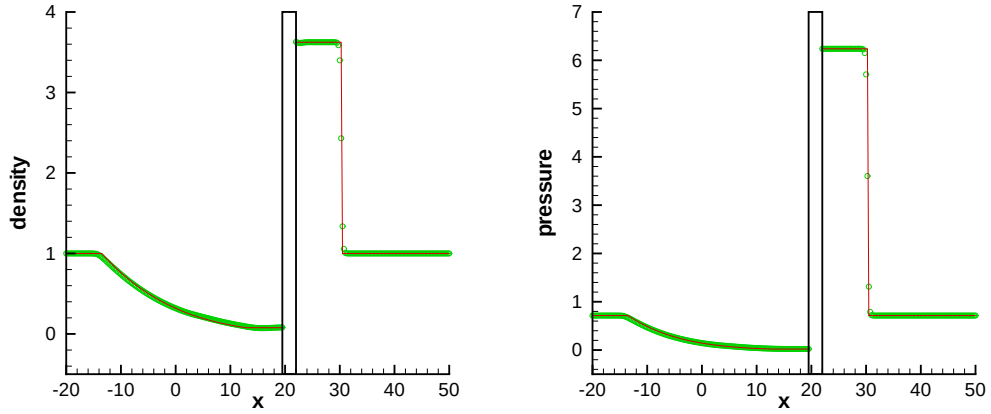

(a) Density (b) Pressure

Figure 3.23: Density and pressure profiles in Example 3.5.2. The piston is represented by the rectangle. Solid lines: exact solutions; Symbols: numerical solutions with $h = 0.25$.

Example 3.5.3. This example involves 2D flows in complex moving geometries. We follow the idea in Example 3.4.11 to construct isentropic flows such that we are able to measure the entropy errors and to analyze the rate of convergence. The computational domain is $[-4, 4] \times [-4, 4]$ with all the boundaries as rigid walls. A rigid cylinder with radius $R = 1$ is initially centered at $(0, 0)$ and starts moving. The center of the cylinder is positioned at $\mathbf{X}_c(t)$. We use our fifth order boundary treatment at the surface of the moving cylinder and the reflection technique at the fixed walls.

The initial conditions should be consistent with the no-penetration boundary

condition (3.43). For this purpose, we define

$$\tilde{u}(x,y) = \lambda_1(x,y)u_1(x,y) + \lambda_2(x,y)^2,$$
$$\tilde{v}_1(x,y) = \lambda_1(x,y)v_1(x,y) + \lambda_2(x,y)v_2(x,y),$$
$$\tilde{v}_2(x,y) = \lambda_1(x,y)v_1(x,y) + \lambda_2(x,y)^2.$$

See (3.42) for the expressions for $u_1(x,y)$, $\lambda_1(x,y)$, $\lambda_2(x,y)$, $v_1(x,y)$, and $v_2(x,y)$.

In our first case, we take $\mathbf{X}_c = (-0.5\sin t, 0)$ such that the cylinder moves horizontally. The initial conditions are $\rho(x,y,0) = 1$, $u(x,y,0) = -0.5\tilde{u}(x,y)$, $v(x,y,0) = 0.5\tilde{v}_1(x,y)$, and $p(x,y,0) = 1$. We run the test to time $t = 0.7$ when the solution keeps smooth. Figure 3.24(a) shows the density contour plot at $t = 0.7$ with $h = 1/40$. We can see that the density ahead of the cylinder is generally larger than its initial value due to the compression. A shock will start to develop shortly afterwards. The left part of Table 3.11 lists the entropy errors in the region $[-2,2] \times [-2,2]$. The designed fifth order convergence is achieved in the L^1 norm.

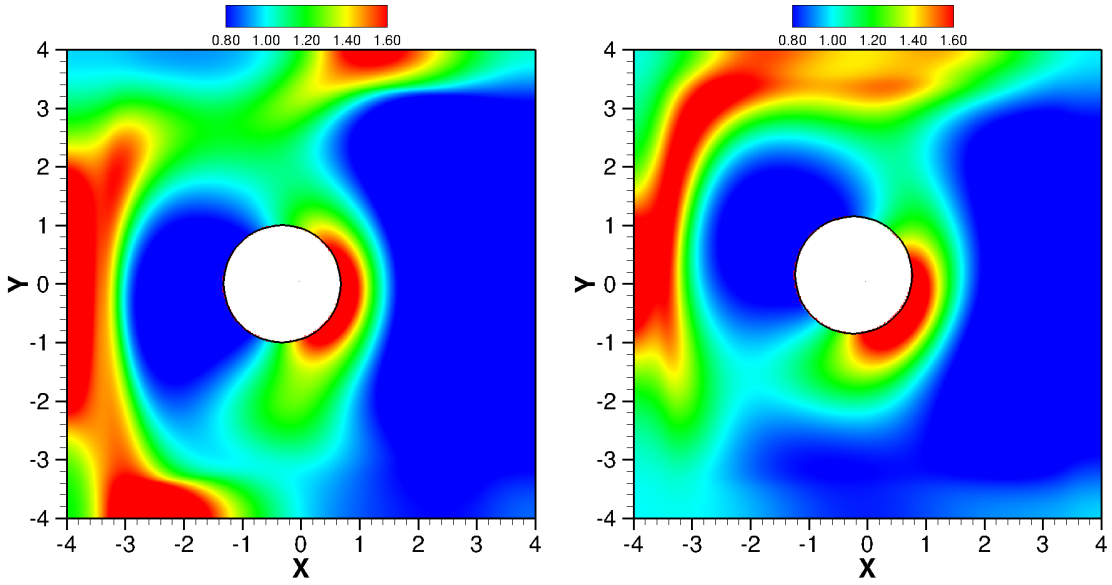

(a) $\mathbf{X}_c = (-0.5\sin t, 0)$, $t = 0.7$ (b) $\mathbf{X}_c = (-0.5\sin t, 0.3t)$, $t = 0.5$

Figure 3.24: Density contours in Example 3.5.3. $h = 1/40$.

Table 3.11: Entropy errors and convergence rates in Example 3.5.3. Errors are computed in the region $[-2,2]\times[-2,2]$.

h	$\mathbf{X}_c=(-0.5\sin t,0)$, $t=0.7$				$\mathbf{X}_c=(-0.5\sin t,0.3t)$, $t=0.5$			
	L^1 error	order	L^∞ error	order	L^1 error	order	L^∞ error	order
1/5	4.11E-03		2.47E-03		3.93E-03		1.79E-03	
1/10	3.86E-04	3.41	3.60E-04	2.78	4.05E-04	3.28	1.93E-04	3.21
1/20	1.21E-05	5.00	1.12E-05	5.00	1.20E-05	5.07	9.20E-06	4.39
1/40	2.43E-07	5.64	6.08E-07	4.21	2.21E-07	5.77	3.73E-07	4.62

In the second case, we take $\mathbf{X}_c=(-0.5\sin t,0.3t)$ such that the cylinder moves in the 2D space. The initial conditions are $\rho(x,y,0)=1$, $u(x,y,0)=-0.5\tilde{u}(x,y)$, $v(x,y,0)=0.3\tilde{v}_2(x,y)$, and $p(x,y,0)=1$. At $t=0.5$, the density contour plot with $h=1/40$ is shown in Figure 3.24(b) and the entropy errors in the region $[-2,2]\times[-2,2]$ are listed in the right part of Table 3.11. Fifth order convergence is again achieved in the L^1 norm.

Example 3.5.4. The last example shows that our high order method can also treat a rigid body whose motion is induced by the fluid. We test the so-called cylinder lift-off problem which is first proposed by Falcovitz et al. [15] and considered in [2, 16, 30, 62] later. In this problem, a rigid cylinder initially resting on the floor of a 2D channel is driven and lifted by a strong shock. The problem setup is the same as in [2, 16, 62]. The computational domain is $[0,1]\times[0,0.2]$. A rigid cylinder with radius 0.05 and density 10.77 is initially centered at $(0.15,0.05)$. A Mach 3 shock starts at $x=0.08$ moving towards the cylinder. The density and pressure of the resting gas are $\rho=1.4$ and $p=1.0$ respectively. The top and bottom of the domain are rigid walls. The left boundary is set to the post-shock state and the right boundary is supersonic outflow.

We use our fifth order boundary treatment with $q=20$ in (3.34) at the surface of the moving cylinder and the reflection technique at the top and bottom walls. Since the cylinder initially rests exactly on the floor, a stencil for high order extrapolation

may be too wide to be contained in the computational domain. We have to use low order extrapolation in this situation and turn to high order extrapolation otherwise. We list the center of the cylinder at two fixed times for different meshes in Table 3.12. The results imply convergence. We plot pressure contours at $t = 0.1641$ and $t = 0.30085$ in Figure 3.25 and Figure 3.26 respectively. The flow structures agree with those in [2, 30, 62].

Table 3.12: Center of the cylinder in Example 3.5.4.

h	$t = 0.1641$		$t = 0.30085$	
	x-coordinate	y-coordinate	x-coordinate	y-coordinate
1/320	3.5878E-01	8.4001E-02	6.4601E-01	1.4713E-01
1/640	3.5542E-01	8.3778E-02	6.3708E-01	1.4717E-01
1/1280	3.5434E-01	8.3827E-02	6.3320E-01	1.4640E-01
1/2560	3.5422E-01	8.4140E-02	6.3357E-01	1.4624E-01

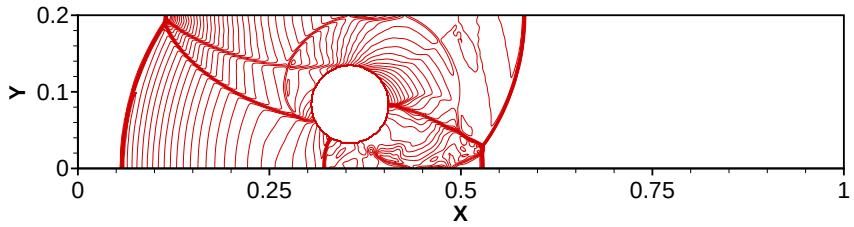

(a) $h = 1/640$

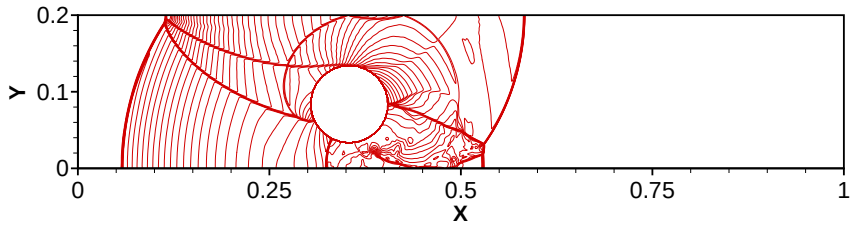

(b) $h = 1/1280$

Figure 3.25: Pressure contours of the cylinder lift-off problem in Example 3.5.4, 53 contours from 2 to 28. $t = 0.1641$.

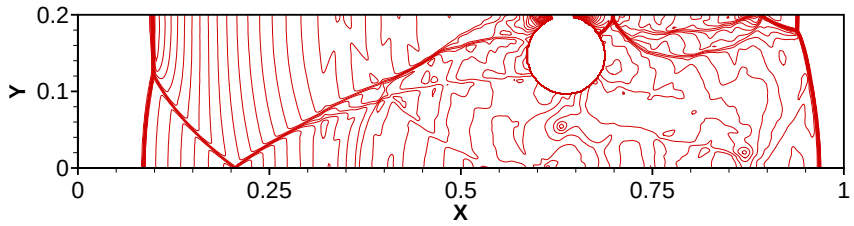

(a) $h = 1/640$

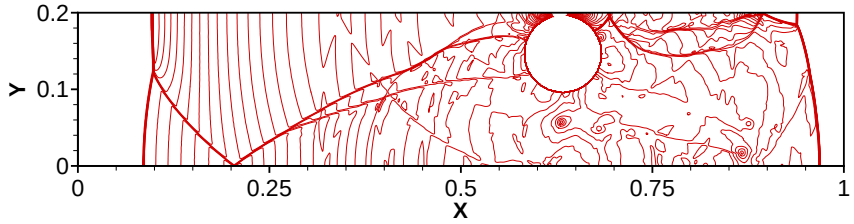

(b) $h = 1/1280$

Figure 3.26: Pressure contours of the cylinder lift-off problem in Example 3.5.4, 53 contours from 2 to 28. $t = 0.30085$.

3.6 Concluding remarks

In this chapter, we develop the ILW procedure for numerical boundary conditions of hyperbolic equations. It is based on Cartesian grids, which is very challenging for accurate and stable boundary treatment because of the wide stencil of the interior WENO scheme and the fact that the physical boundary is not necessarily aligned with the grids. Our method is high (up to fifth) order accurate, stable, and easy to implement. It has been successfully applied to simulate interactions between compressible inviscid flows and rigid (static or moving) bodies with complex geometries. Standard CFL conditions determined by the interior WENO schemes are used in our numerical experiments without any problems. A theoretical proof of the time step restriction remains to be done by the GKS analysis.

The challenge of high order boundary treatment is not limited to finite difference schemes. Even for finite element type methods, difficulties sometimes arise if

unstructured, straight-sided meshes are used to fit curved, static geometries, see [4]. Krivodonova and Berger [37] propose an accurate implementation of no-penetration boundary condition for Discontinuous Galerkin (DG) methods on such meshes. We will try to extend our boundary treatment to DG methods on *rectangular* meshes in our future work.

We have only considered the interaction between compressible inviscid flows and rigid bodies without deformation. In general fluid-structure interaction problems, the fluids can be viscous and the geometrically complicated structures are considered to be elastic or plastic. A closely related problem is the multi-fluid problem that involves internal boundaries separating different fluids. Low order coupling methods have been developed. See [2] for a coupling of compressible inviscid flows and elastic solids, and [30] for a multi-fluid coupling. Our high order boundary treatment looks promising for *more accurate* couplings in both types of problems.

Chapter Four

Simulation of the updated Buxton-Clarke model for organic photovoltaic cells

This chapter focuses on the application of finite difference WENO schemes to the simulation of organic photovoltaic (OPV) cells.

4.1 Introduction

In the past decade, OPV cells have emerged as an intensely studied alternative energy technology. However, their relatively low efficiency [55] is a major factor limiting their practical use at this time. We refer the reader to [45] for a review of device operation, materials requirements, and current technical challenges in making more efficient organic solar cells. Modeling of OPV cells can be achieved by adaptation of the classical drift-diffusion models, which are originally developed for solid-state devices [32]. Replacement of crystalline solid-state materials by organic materials leads to much slower carrier mobility and to a new carrier: the exciton, which is a bound electron-hole pair. The Buxton-Clarke (BC) model [8] includes electrons, holes, and excitons, together with generation, dissociation, and recombination mechanisms connecting these carriers, partially induced by device illumination.

We propose an updated BC model that explicitly incorporates the charge transfer (CT) state that has been shown to influence device performance. The updated model allows us to evaluate two commonly studied OPV architectures, the bilayer (BL) and blended bulk heterojunction (BHJ). Moreover, we introduce a large effective mobility to properly capture dissociation while keeping the bulk mobilities at standard values for evaluation of the continuity equations.

From a mathematical point of view, the updated BC model is represented by a system of convection-diffusion-reaction equations coupled to a Poisson's equation.

The solution is usually continuous but may contain sharp gradients. Finite difference WENO schemes are well suited for solving such problems because they allow us to use relatively coarse grids and still get very accurate results without any oscillation near sharp gradient regions.

The goals of our modeling include quantifying the efficiency losses engendered by the low mobility of the materials comprising OPV systems. We compare the BL and BHJ architectures and separately investigate the sensitivity of each architecture to mobility.

This chapter is organized as follows. We first introduce our updated BC model in Section 4.2. The equations are properly scaled for computation. Then the finite difference WENO schemes for solving the system of equations are described in Section 4.3. Three sets of simulations are presented in Section 4.4: dark current simulation for determining the value of a crucial parameter, model validation and verification, and comparison study to investigate the effect of mobility on device performance. Finally, concluding remarks are given in Section 4.5.

4.2 Updated Buxton-Clarke model

4.2.1 Continuity equations

The densities of electrons n, holes p, excitons X, and CT state I are described by continuity equations, where the electric field E is expressed by the Poisson's equation

of the electric potential ϕ:

$$n_t = D(E,I) - R(n,p) + (\mu_n E n)_x + U_T\,(\mu_n n_x)_x\,, \tag{4.1}$$

$$p_t = D(E,I) - R(n,p) - (\mu_p E p)_x + U_T\,(\mu_p p_x)_x\,, \tag{4.2}$$

$$X_t = G(x) - k_{\text{cap}}(x)X - k_{R,X}X + U_T\,(\mu_X X_x)_x\,, \tag{4.3}$$

$$I_t = -D(E,I) + k_{\text{cap}}(x)X - k_{R,I}I, \tag{4.4}$$

$$\phi_{xx} = -\frac{q(p-n)}{\varepsilon_0\varepsilon_r(x)}, \quad E = -\phi_x. \tag{4.5}$$

The quantities G, D, and R are the exciton photo-generation rate, the exciton dissociation rate, and the carrier recombination rate respectively. G is determined by the experimental photo flux; D is modeled by Braun's adaptation of Onsager's theory of geminate dissociation; and R is the traditional Langevin bimolecular recombination rate. The carrier mobilities are represented by μ_n and μ_p. The pseudo-mobility of excitons, with adjusted units of mobility, is denoted μ_X. The thermal voltage $U_T = k_B T_0/q$, where k_B is the Boltzmann constant, T_0 is the ambient temperature, and q is the unit charge. ε_0 is the vacuum permittivity whereas ε_r is the relative permittivity. The terms k_{cap}, $k_{R,X}$, and $k_{R,I}$ are introduced later.

Compared with the original BC model [8], the updated model incorporates the CT state dynamics. A recombination term $R(n,p)/4$ is removed from the equation for X, since there is no physical basis for supposing that the recombination of electrons and holes recreates excitons.

4.2.2 Expressions

1. Recombination [8]: $R(n,p) = \frac{q(\mu_n+\mu_p)}{\varepsilon_0\varepsilon_r} np$.

2. Modified Onsager-Braun dissociation:

$$D(E,I) = \frac{3\mu_{\text{Eff}} q}{4\pi\varepsilon_0\varepsilon_r a^3} \exp\left(-\frac{E_B}{k_B T_0}\right) \Phi\left(b\left(|E|\right)\right) I,$$

where

$$E_B = \frac{q^2}{4\pi\varepsilon_0\varepsilon_r a},$$

$$b\left(|E|\right) = \frac{q^3|E|}{8\pi\varepsilon_0\varepsilon_r k_B^2 T_0^2},$$

and Φ is given in terms of the Bessel function J_1 of order one by

$$\Phi(u) = J_1(2\sqrt{-2u})/\sqrt{-2u}, \quad u \mapsto b\left(|E|\right).$$

Compared with the original Onsager-Braun model [7], the sum of mobilities is replaced by a large effective mobility μ_{Eff}.

3. Exciton photo-generation [14]:

$$G(x) = \alpha_0\Gamma_0 \exp\left(-\alpha_0 x\right).$$

4. Coulomb radius [53]: $r_C = \frac{q^2}{4\pi\varepsilon_r\varepsilon_0 k_B T_0}$.

4.2.3 Geometry

We consider a 1D device with length $d = 100$nm. The illumination site is at $x = 0$ and the electron collection site is at $x = d$. The donor material occupies the region $(0, d/2)$ and the acceptor region occupies $(d/2, d)$.

The parameters $k_{\text{cap}}(x)$ and $\varepsilon_r(x)$ carry an x dependence:

$$k_{\text{cap}}(x) = \begin{cases} 0, & |x - x_I| > L_{\text{Blend}}, \\ k_{\text{cap},0}, & |x - x_I| \leq L_{\text{Blend}}; \end{cases}$$

$$\varepsilon_r(x) = \begin{cases} \varepsilon_D, & 0 < x < x_I - L_{\text{Blend}}, \\ (\varepsilon_D + \varepsilon_A)/2, & |x - x_I| \leq L_{\text{Blend}}, \\ \varepsilon_A, & x_I + L_{\text{Blend}} < x < d, \end{cases}$$

where $x_I = d/2$ is the location of the interface. The introduction of spatially dependent k_{cap} and ε_r is unique to this study. It allows us to evaluate systems in the limit of a perfect BL ($L_{\text{Blend}} = 0$) and a perfect BHJ ($L_{\text{Blend}} = d/2$).

4.2.4 Boundary conditions and initial conditions

Boundary conditions

Schottky barrier condition [53] is imposed at both $x = 0$ and $x = d$ for electron and hole. The barrier concentration is field dependent and is given as

$$\begin{aligned} n|_{x=0} &= 4\psi^2 N_0 \exp\left(-\frac{\phi_{\text{An},n}}{qU_T}\right) \exp(f^{1/2}), \\ n|_{x=d} &= 4\psi^2 N_0 \exp\left(-\frac{\phi_{\text{Cat},n}}{qU_T}\right) \exp(f^{1/2}), \\ p|_{x=0} &= 4\psi^2 N_0 \exp\left(-\frac{\phi_{\text{An},p}}{qU_T}\right) \exp(f^{1/2}), \\ p|_{x=d} &= 4\psi^2 N_0 \exp\left(-\frac{\phi_{\text{Cat},p}}{qU_T}\right) \exp(f^{1/2}), \end{aligned}$$

where

$$f = \frac{q|E|r_C}{k_B T_0}, \tag{4.6}$$

$$\psi(f) = f^{-1} + f^{-1/2} - f^{-1}(1 + 2f^{1/2})^{1/2},$$

$$\begin{aligned}
\phi_{\mathrm{An},n} &= EA_D - E_{f,\mathrm{An}}, \\
\phi_{\mathrm{Cat},n} &= EA_A - E_{f,\mathrm{Cat}}, \\
\phi_{\mathrm{An},p} &= E_{f,\mathrm{An}} + IP_D, \\
\phi_{\mathrm{Cat},p} &= E_{f,\mathrm{Cat}} + IP_A.
\end{aligned}$$

See Figure 4.1 for a schematic description of energies relevant to boundary conditions. N_0 is the surface density and is a critical parameter. Its value is obtained by fine-tuning the dark current, see Section 4.4.1.

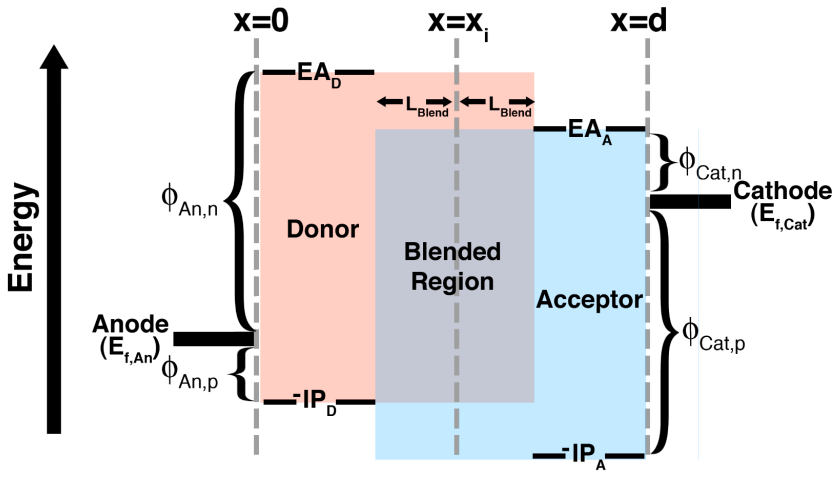

Figure 4.1: Schematic description of energies relevant to boundary conditions.

A homogeneous Dirichlet boundary condition is imposed for the exciton

$$X|_{x=0} = X|_{x=d} = 0.$$

No boundary condition is needed for the CT state I since (4.4) is actually an ODE.

The boundary condition for the electric potential is

$$\phi|_{x=0} = V_{\text{Tot}},$$
$$\phi|_{x=d} = 0,$$

where the total voltage is the sum of the built-in voltage V_{BI} and the bias V_{Ext}

$$\begin{aligned} V_{\text{Tot}} &= V_{\text{BI}} + V_{\text{Ext}} \\ &= (E_{f,\text{An}} - E_{f,\text{Cat}}) + V_{\text{Ext}}. \end{aligned} \tag{4.7}$$

Initial conditions

$n = p = X = I = 0$ at $t = 0$.

4.2.5 Parameters

We summarize the definition of parameters in Table 4.1. Representative values of the parameters are listed in Table 4.2. Some values may change in our comparison studies.

4.2.6 Scaled equations

Since the variables in the updated BC model are of different orders of magnitude and can vary considerably throughout the heterogeneous system, we scale the equations (4.1)–(4.5) before solving it numerically. The space variable x is scaled by $a_0 =$

variable	definition
q	unit charge
ε_0	vacuum permittivity
k_B	Boltzmann constant
T_0	ambient temperature
ε_A	relative permittivity of the acceptor
ε_D	relative permittivity of the donor
μ_n	electron mobility
μ_p	hole mobility
μ_X	exciton pseudo-mobility
μ_{Eff}	effective local mobility for dissociation
$k_{\mathrm{cap},0}$	rate constant for capture of excitons at interface
$k_{R,I}$	recombination rate constant of interfacial species
$k_{R,X}$	decay rate constant of exciton
a	thermalization radius
α_0	absorption coefficient
Γ_0	photon flux
x_I	location of donor-acceptor interface
L_{Blend}	region of interfacial blending
$E_{f,\mathrm{An}}$	Fermi level of the anode
$E_{f,\mathrm{Cat}}$	Fermi level of the cathode
IP_D	ionization potential of the donor
IP_A	ionization potential of the acceptor
EA_D	electron affinity of the donor
EA_A	electron affinity of the acceptor
N_0	surface density of electrons/holes

Table 4.1: Physical meaning of the parameters in the updated BC model.

variable	value	units
q	1.60×10^{-19}	C
ε_0	$8.85{\times}10^{-12}$	$\mathrm{C{\cdot}V^{-1} \cdot m^{-1}}$
k_B	1.38×10^{-23}	$\mathrm{J{\cdot}K^{-1}}$
T_0	300	K
ε_A	4	unitless
ε_D	3	unitless
μ_n	1×10^{-9}	$\mathrm{m^2 \cdot V^{-1} \cdot s^{-1}}$
μ_p	1×10^{-9}	$\mathrm{m^2 \cdot V^{-1} \cdot s^{-1}}$
μ_X	3.86×10^{-6}	$\mathrm{m^2 \cdot V^{-1} \cdot s^{-1}}$
μ_{Eff}	1×10^{-5}	$\mathrm{m^2 \cdot V^{-1} \cdot s^{-1}}$
$k_{\mathrm{cap},0}$	3×10^{12}	$\mathrm{s^{-1}}$
$k_{R,I}$	1×10^{9}	$\mathrm{s^{-1}}$
$k_{R,X}$	1×10^{9}	$\mathrm{s^{-1}}$
a	2×10^{-9}	m
α_0	2×10^{7}	$\mathrm{m^{-1}}$
Γ_0	1×10^{21}	$\mathrm{photons{\cdot}m^{-2} \cdot s^{-1}}$
x_I	50×10^{-9}	m
L_{Blend}	$0,\ 50 \times 10^{-9}$	m
$E_{f,\mathrm{An}}$	-5	eV
$E_{f,\mathrm{Cat}}$	-4	eV
IP_D	5.25	eV
IP_A	6	eV
EA_D	-3	eV
EA_A	-3.75	eV
N_0	1×10^{27}	$\mathrm{m^{-3}}$

Table 4.2: Representative values of the parameters in the updated BC model. Some values may change in our comparison studies.

1nm $= 10^{-9}$m. The carrier densities n, p, X, and I are scaled by $N = \varepsilon_0 U_T/(qa_0^2)$. The electric potential ϕ is scaled by U_T and thus the electric field E is scaled by U_T/a_0. The mobilities μ_n, μ_p, μ_X, and μ_{Eff} are scaled by $\mu_{\max} = 10^{-8}\text{m}^2/\text{V/s}$. The time t is scaled by $a_0^2/(\mu_{\max} U_T)$ and thus k_{cap}, $k_{R,X}$, and $k_{R,I}$ are scaled by $\mu_{\max} U_T/a_0^2$. The updated BC model is written in a scaled form as

$$\frac{\partial n}{\partial t} = D(E,I) - R(n,p) + \frac{\partial J_n}{\partial x}, \tag{4.8}$$

$$\frac{\partial p}{\partial t} = D(E,I) - R(n,p) - \frac{\partial J_p}{\partial x}, \tag{4.9}$$

$$\frac{\partial X}{\partial t} = G(x) - k_{\text{cap}}(x)X - k_{R,X}X + \mu_X \frac{\partial^2 X}{\partial x^2}, \tag{4.10}$$

$$\frac{\partial I}{\partial t} = -D(E,I) + k_{\text{cap}}(x)X - k_{R,I}I, \tag{4.11}$$

$$\phi_{xx} = -\frac{p-n}{\varepsilon_r(x)}, \quad E = -\phi_x, \tag{4.12}$$

where

$$J_n = \mu_n E n + \mu_n n_x, \tag{4.13}$$

$$J_p = \mu_p E p - \mu_p p_x, \tag{4.14}$$

are called charge fluxes. qJ_n and qJ_p are electron and hole current densities respectively. Charge fluxes are scaled by $\mu_{\max} U_T N/a_0$.

The scaled terms D, R, and G are given as

$$D(E,I) = \frac{3}{32\pi\varepsilon_r}\frac{\mu_{\text{Eff}}}{Na_0^3}\exp\left(-\frac{1}{8\pi\varepsilon_r}\frac{1}{Na_0^3}\right)\Phi\left(b\left(|E|\right)\right)I, \quad b\left(|E|\right) = \frac{1}{8\pi\varepsilon_r}\frac{|E|}{Na_0^3},$$

$$R(n,p) = \frac{\mu_n + \mu_p}{\varepsilon_r} np,$$

$$G(x) = \frac{\alpha_0 \Gamma_0 a_0^2}{N\mu_{\max} U_T}\exp\left[-(\alpha_0 a_0)\, x\right].$$

The scaled f in (4.6) is

$$f = \frac{1}{4\pi\varepsilon_r}\frac{1}{Na_0^3}\left|E\right|.$$

4.3 Numerical methods

We use finite difference WENO schemes to solve the *scaled* equations (4.8)–(4.12). We are mainly interested in the solutions at steady state. In particular, we would like to find the relation between the bias V_{Ext} defined in (4.7) and the total current density J_T defined as

$$\begin{aligned} J_T &= q(J_n + J_p) \\ &= q(\mu_n En + \mu_n n_x + \mu_p Ep - \mu_p p_x). \end{aligned} \tag{4.15}$$

We have a uniform mesh $x_i = i\Delta x$ with mesh size $\Delta x = 1\text{nm}$. At each time step, we first solve the Poisson's equation (4.12). We discretize the Laplacian $\frac{\partial^2}{\partial x^2}$ by a second order central scheme

$$\frac{\phi_{i-1} - 2\phi_i + \phi_{i+1}}{\Delta x^2} = -\frac{p_i - n_i}{\varepsilon_r(x_i)}.$$

Together with Dirichlet boundary conditions for ϕ, we are able to solve ϕ_i and thus $E_i = (\phi_{i+1} - \phi_{i-1})/2\Delta x$ at current time level.

We next would like to evolve the continuity equations (4.8)–(4.11) to the next time level. (4.10) has no convection term. Thus the diffusion term $\frac{\partial^2 X}{\partial x^2}$ is discretized

by the second order central difference

$$\frac{\partial^2 X}{\partial x^2} \approx \frac{X_{i+1} - 2X_i + X_{i-1}}{\Delta x^2}.$$

The approximations to the "fluxes" $-J_n$ in (4.8) and J_p in (4.9) are obtained by WENO schemes. The first derivatives involved in (4.13) and (4.14) are evaluated by a second order central difference approximation. The remaining procedure for computing the numerical "fluxes" is the same as described in Section 2.1. With the right-hand side of the equations (4.8)–(4.11) discretized, we are ready to evolve the equations to the next time level by the RK method (2.8). The whole procedure will be repeated until we reach steady state.

4.4 Numerical results

4.4.1 Fine-tuning dark current

The dark current is the total current density in the device if we turn Γ_0 off, i.e., $\Gamma_0 = 0$. In practice, its magnitude is usually in the range of several $\mathrm{mA/cm^2}$. In our model, the dark current is very sensitive to the surface parameter N_0 in the Schottky barrier condition, which is usually in the range of $10^{26} \sim 10^{27}\mathrm{m}^{-3}$. We would like to fine-tune the value of N_0 such that the dark current is in the range of $[0, 3\mathrm{mA/cm^2}]$.

We set $N_0 = 2 \times 10^{26}, 4 \times 10^{26}, \ldots, 10 \times 10^{26}\mathrm{m}^{-3}$. For each N_0, we take a series of biases $V_{\mathrm{Ext}} = -1, -0.9, \ldots, 1.5\mathrm{V}$ and compute the total current density J_T defined in (4.15). We plot the so-called J-V curves (mean value of J_T versus V_{Ext}) in Figure 4.2. We conclude that N_0 should be taken as $N_0 = 1 \times 10^{27}\mathrm{m}^{-3}$ in order to have the

dark current filled in the desired range.

4.4.2 Model validation and verification

In this section, we plot the profiles of the physical quantities to make sure our numerical method has been implemented properly. We also do some preliminary tests to see whether our model represents the behavior of the real systems.

BL system

We take the parameter values from Table 4.2 and set $L_{\text{Blend}} = 0\text{nm}$ to simulate the BL system. The bias is set to $V_{\text{Ext}} = 0.7\text{V}$. We display the electron and hole density profiles at steady state in Figure 4.3. The exciton and CT state density profiles are portrayed in Figure 4.4. The WENO schemes give excellent non-oscillatory resolutions for all profiles with sharp gradients. In the vicinity of the interface at $x = 50\text{nm}$, there is much more I than X, although the absolute magnitude of both is quite small compared to electrons and holes. The Exciton density increases rapidly as moving spatially away from the interface. This is exactly what we expect from the model.

The current densities are shown in Figure 4.5. The total current J_T is almost a constant throughout the device at steady state. It should be so, since subtracting (4.9) from (4.8) yields $\frac{\partial J_T}{\partial x} \equiv 0$. The magnitude of J_T is comparable to experimental data. Figure 4.6 shows the time evolution of the total current density. Our numerical solution indeed reaches the steady state.

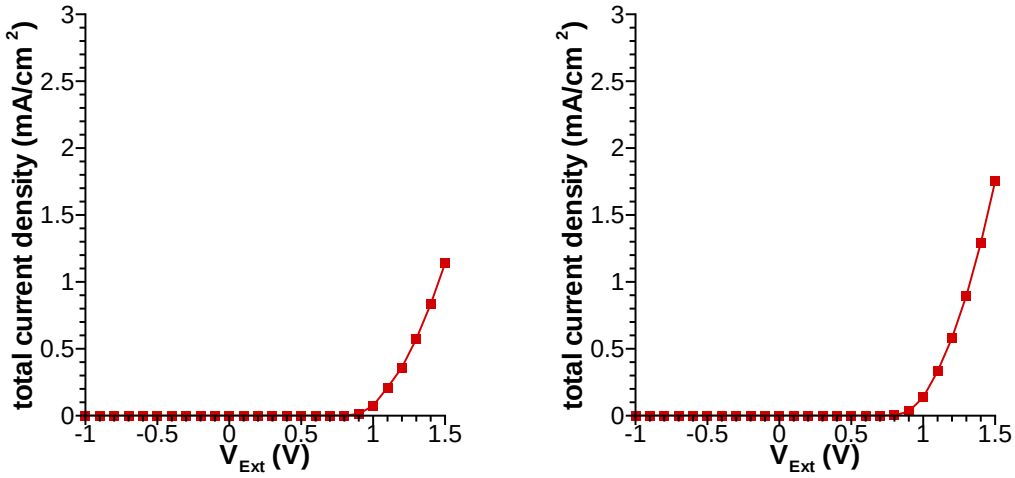

(a) $N_0 = 2 \times 10^{26}\mathrm{m}^{-3}$

(b) $N_0 = 4 \times 10^{26}\mathrm{m}^{-3}$

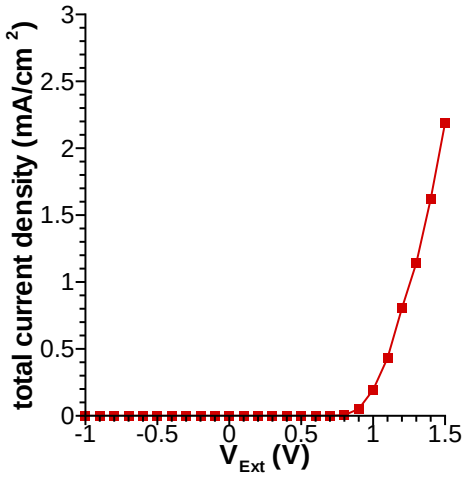

(c) $N_0 = 6 \times 10^{26}\mathrm{m}^{-3}$

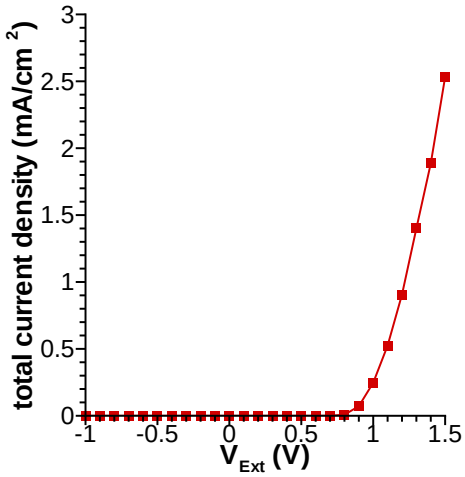

(d) $N_0 = 8 \times 10^{26}\mathrm{m}^{-3}$

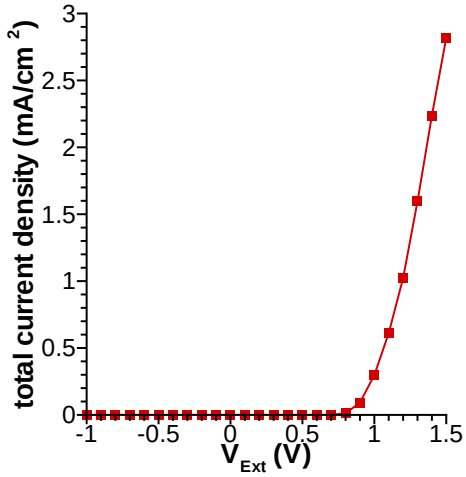

(e) $N_0 = 1 \times 10^{27}\mathrm{m}^{-3}$

Figure 4.2: J-V curves of the dark current ($\Gamma_0 = 0$) for determining the surface parameter N_0.

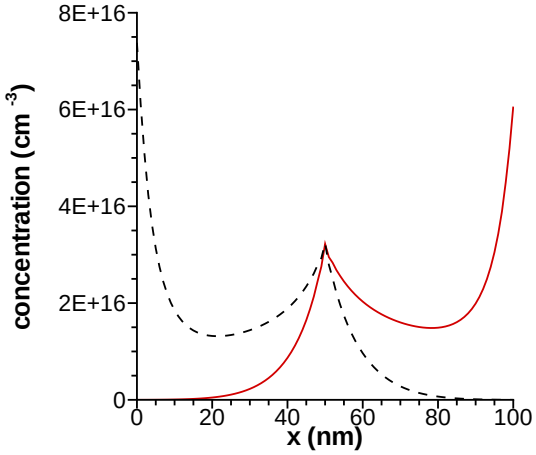

Figure 4.3: Steady-state electron and hole density profiles of the BL system. Solid line: Electron density; Dashed line: Hole density.

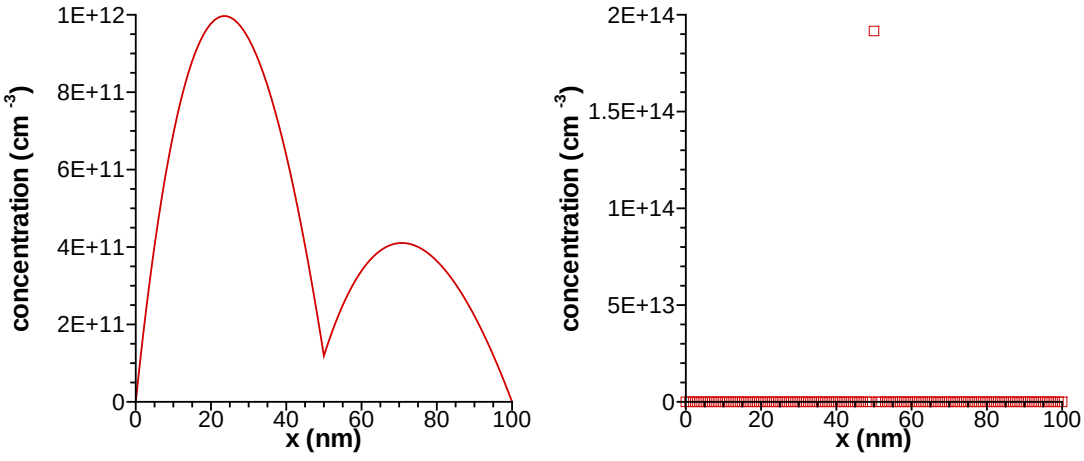

(a) Exciton (b) CT state

Figure 4.4: Steady-state exciton and CT state density profiles of the BL system.

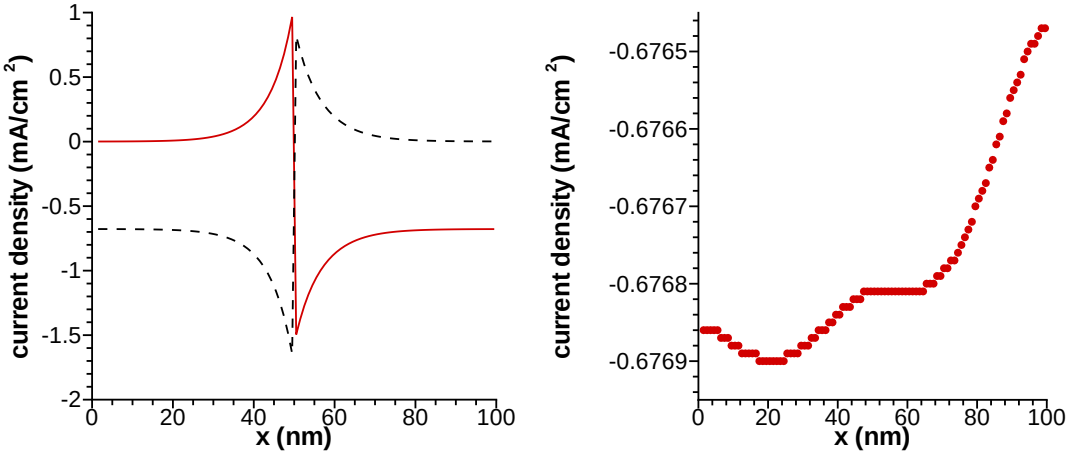

(a) Solid line: Electron current density J_n; Dashed line: Hole current density J_p

(b) Total current density $J_T = J_n + J_p$

Figure 4.5: Steady-state current density profiles of the BL system.

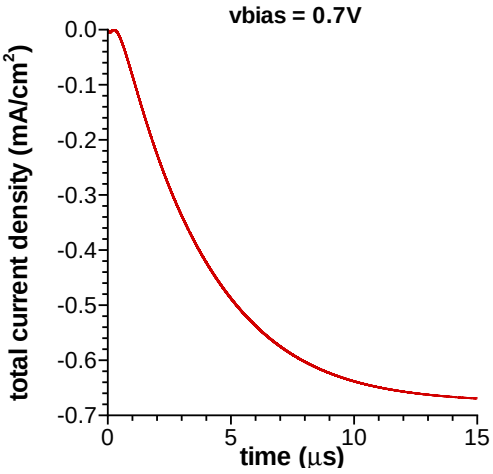

Figure 4.6: Time evolution of total current density of the BL system.

BHJ system

Same tests are done for the BHJ system by setting $L_{\text{Blend}} = 50\text{nm}$. WENO schemes again perform well on the relatively coarse mesh. We only show the pictures here since the discussions are similar.

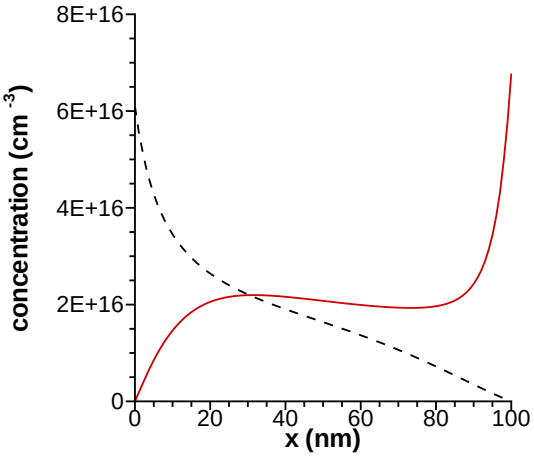

Figure 4.7: Steady-state electron and hole density profiles of the BHJ system. Solid line: Electron density; Dashed line: Hole density.

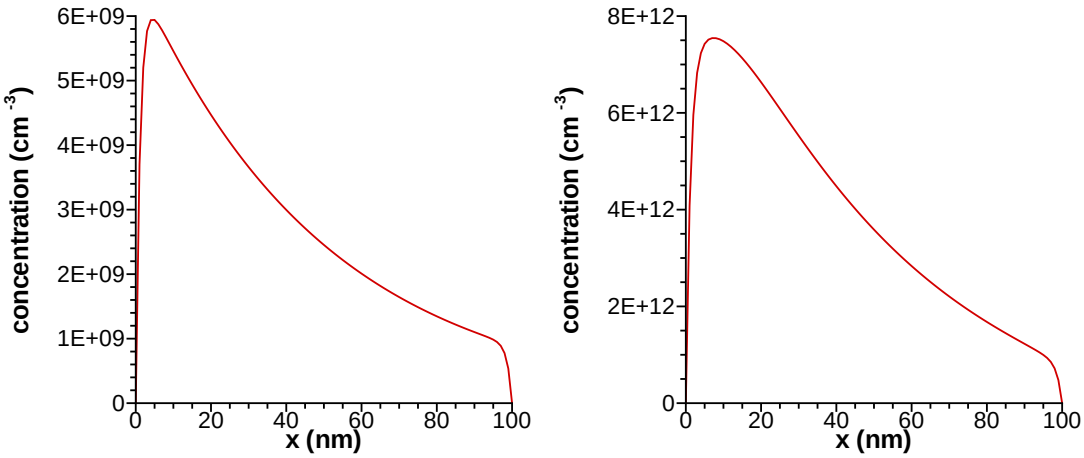

(a) Exciton (b) CT state

Figure 4.8: Steady-state exciton and CT state density profiles of the BHJ system.

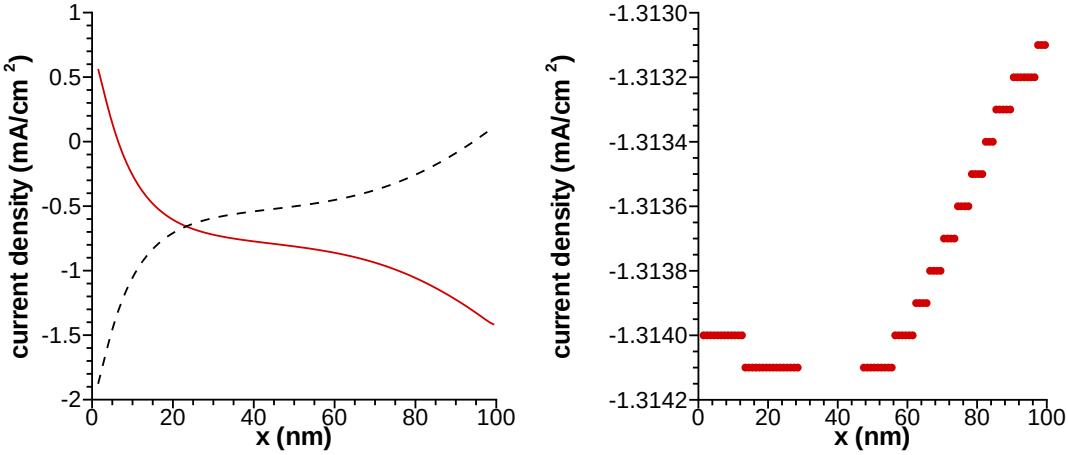

(a) Solid line: Electron current density J_n; Dashed line: Hole current density J_p

(b) Total current density $J_T = J_n + J_p$

Figure 4.9: Steady-state current density profiles of the BHJ system.

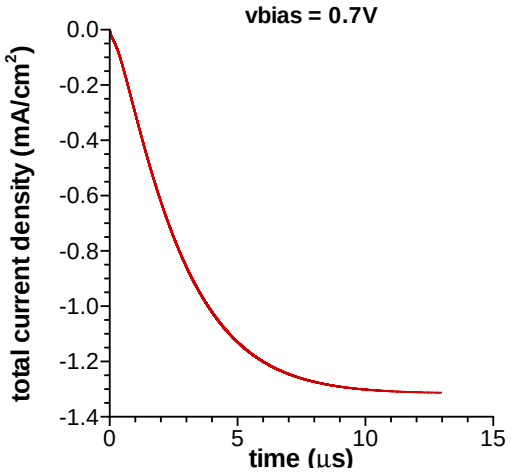

Figure 4.10: Time evolution of total current density of the BHJ system.

4.4.3 Effect of mobility on device performance

The effect of mobility on device performance is investigated by varying the electron (μ_n) and hole (μ_p) mobility from 10^{-9} to $10^{-4}\text{m}^2 \cdot \text{V}^{-1} \cdot \text{s}^{-1}$ while holding them equal. The relative performance enhancements in the BL and BHJ architectures are reported in Figure 4.11(a) and Figure 4.11(b) respectively. Figure 4.11(a) shows that optimal performance, as measured by the maximal product of $-J_T \cdot V_{\text{Ext}}$, is obtained for $\mu_n = \mu_p = 10^{-7}\text{m}^2 \cdot \text{V}^{-1} \cdot \text{s}^{-1}$. Increases in mobility above $10^{-7}\text{m}^2 \cdot \text{V}^{-1} \cdot \text{s}^{-1}$ leads to reduced open-circuit voltage (x-intercept in the J-V curve) due to dark current enhancement. The optimal mobility for the BHJ is also found to be $\mu_n = \mu_p = 10^{-7}\text{m}^2 \cdot \text{V}^{-1} \cdot \text{s}^{-1}$. The BHJ shows a pronounced photocurrent enhancement at higher mobilities, accenting the importance of Langevin recombination in this architecture.

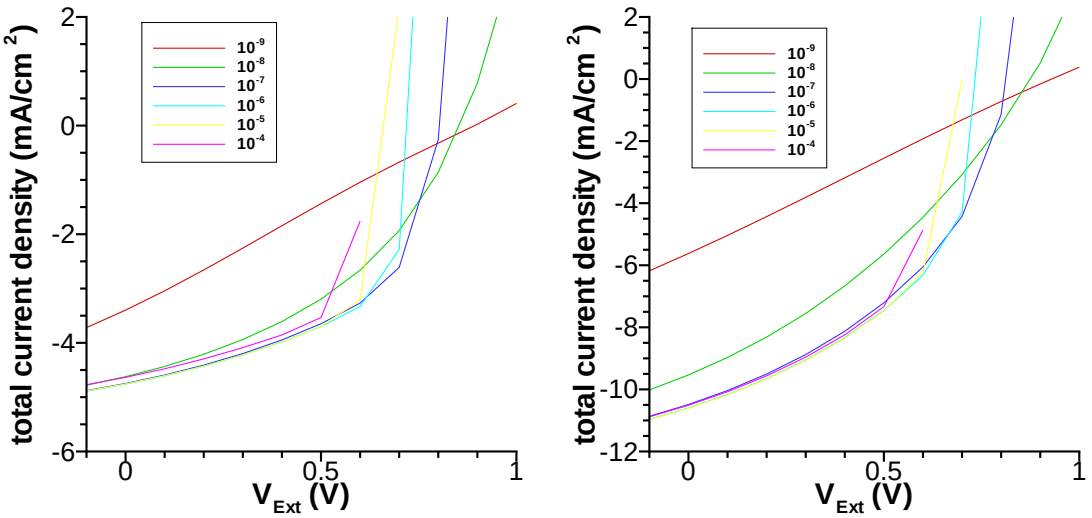

(a) BL system (b) BHJ system

Figure 4.11: J-V curves with $\mu_n = \mu_p$. The mobility is varied from 10^{-9} to $10^{-4}\text{m}^2 \cdot \text{V}^{-1} \cdot \text{s}^{-1}$.

The effect of a mobility mismatch ($\mu_n \neq \mu_p$) is also investigated by taking $\mu_n = 10^{-9}\text{m}^2 \cdot \text{V}^{-1} \cdot \text{s}^{-1}$ while keeping $\mu_p = 10^{-4}\text{m}^2 \cdot \text{V}^{-1} \cdot \text{s}^{-1}$, see Figure 4.12(a) and Figure 4.12(b). Mismatched mobility in the BL results in an improved short-

circuit current (y-intercept) but leads to a compensating reduction in open-circuit voltage (x-intercept). Mismatched mobility results in both open-circuit voltage and photocurrent losses in the BHJ, unlike the BL system that shows some current enhancement.

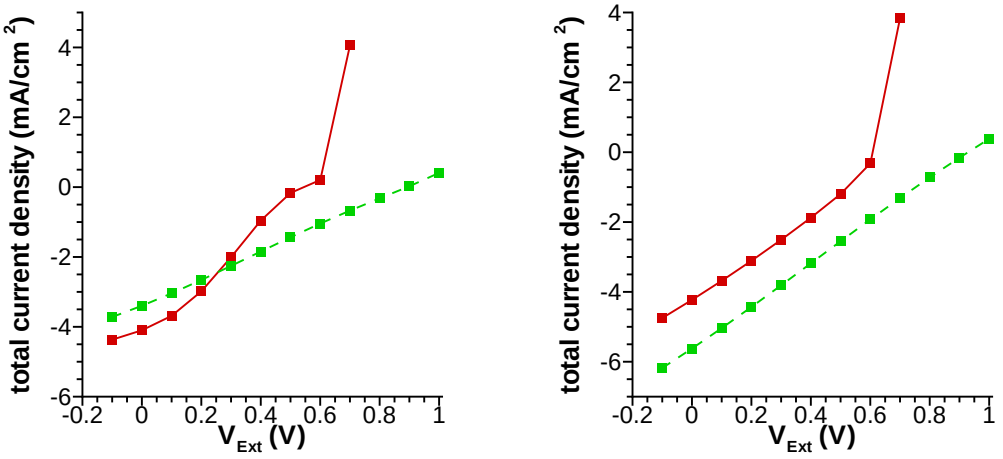

(a) BL system (b) BHJ system

Figure 4.12: J-V curves with mobility mismatch $\mu_n \neq \mu_p$. Solid (Red) lines: $\mu_n = 10^{-9}\mathrm{m}^2 \cdot \mathrm{V}^{-1} \cdot \mathrm{s}^{-1}$ and $\mu_p = 10^{-4}\mathrm{m}^2 \cdot \mathrm{V}^{-1} \cdot \mathrm{s}^{-1}$; Dashed (Green) lines: $\mu_n = \mu_p = 10^{-9}\mathrm{m}^2 \cdot \mathrm{V}^{-1} \cdot \mathrm{s}^{-1}$.

Discussion

The simulations indicate that efficiency enhancements can be achieved by using higher mobility materials. Interestingly, we observe a maximal mobility above which dark current and recombination via Langevin term results in a net reduction of performance. Finally, optimal performance is observed when the mobility of both components match, indicating that increasing the mobility of only one component may in fact hurt performance.

4.5 Concluding remarks

We develop an updated BC model for the simulation of OPV cells. The main feature is that the CT state dynamics is explicitly incorporated in our model. Finite difference WENO schemes are well suited for solving the problem since the solutions may contain sharp gradients. Numerical tests demonstrate that excellent resolutions are obtained on a relatively coarse mesh. Through the modeling, the efficiency losses due to the low mobility of the BL and BHJ systems are quantified.

Our future work is to simulate systems composed of concrete materials so that we are able to compare our numerical results with experimental data. We might need to consider field dependent carrier mobilities for some types of materials. We also plan to extend our model to multiple space dimensions.

Bibliography

[1] Appelö, D. and Petersson, N.A. *A fourth-order accurate embedded boundary method for the wave equation.* preprint.

[2] Arienti, M., Hung, P., Morano, E., and Shepherd, J.E. *A level set approach to Eulerian-Lagrangian coupling.* J. Comput. Phys. **185** (2003), 213–251.

[3] Bartenev, A.M., Khomik, S.V., Gelfand, B.E., Grönig, H., and Olivier, H. *Effect of reflection type on detonation initiation at shock-wave focusing.* Shock Waves **10** (2000), 205–215.

[4] Bassi, F. and Rebay, S. *High-order accurate discontinuous finite element solution of the 2D Euler equations.* J. Comput. Phys. **138** (1997), 251–285.

[5] Berger, M.J., Helzel, C., and LeVeque, R.J. *h-box methods for the approximation of hyperbolic conservation laws on irregular grids.* SIAM J. Numer. Anal. **41** (2003), 893–918.

[6] Bourlioux, A. and Majda, A.J. *Theoretical and numerical structure of unstable detonations.* Philos. Trans. R. Soc. Lond. Ser. A Math. Phys. Eng. Sci. **350** (1995), 29–68.

[7] Braun, C.L. *Electric field assisted dissociation of charge transfer states as a mechanism of photocarrier production.* J. Chem. Phys. **80** (1984), 4157–4161.

[8] Buxton, G.A. and Clarke, N. *Computer simulation of polymer solar cells.* Modelling Simul. Mater. Sci. Eng. **15** (2007), 13–26.

[9] Carpenter, M.H., Gottlieb, D., Abarbanel, S., and Don, W.-S. *The theoretical accuracy of Runge-Kutta time discretizations for the initial boundary value problem: a study of the boundary error.* SIAM J. Sci. Comput. **16** (1995), 1241–1252.

[10] Cheng, J. and Shu, C.-W. *A high order ENO conservative Lagrangian type scheme for the compressible Euler equations.* J. Comput. Phys. **227** (2007), 1567–1596.

[11] Colella, P. and Woodward, P.R. *The piecewise parabolic method (PPM) for gas dynamical simulations.* J. Comput. Phys. **54** (1984), 174–201.

[12] De Palma, P., de Tullio, M.D., Pascazio, G., and Napolitano, M. *An immersed-boundary method for compressible viscous flows.* Comput. & Fluids **35** (2006), 693–702.

[13] de Tullio, M.D., De Palma, P., Iaccarino, G., Pascazio, G., and Napolitano, M. *An immersed boundary method for compressible flows using local grid refinement.* J. Comput. Phys. **225** (2007), 2098–2117.

[14] Fahrenbruch, A.L. and Bube, R.H. *Fundamentals of solar cells: photovoltaic solar energy conversion.* Academic Press, 1983.

[15] Falcovitz, J., Alfandary, G., and Hanoch, G. *A two-dimensional conservation laws scheme for compressible flows with moving boundaries.* J. Comput. Phys. **138** (1997), 83–102.

[16] Forrer, H. and Berger, M. *Flow simulations on Cartesian grids involving complex moving geometries.* In: Proc. 7th Intl. Conf. on Hyperbolic Problems, Jeltsch, R. (Ed.), Birkhäuser Verlag, Basel, 1998, pp. 315–324.

[17] Forrer, H. and Jeltsh, R. *A high-order boundary treatment for Cartesian-grid methods.* J. Comput. Phys. **140** (1998), 259–277.

[18] Gamezo, V.N., Desbordes, D., and Oran, E.S. *Two-dimensional reactive flow dynamics in cellular detonation waves.* Shock Waves **9** (1999), 11–17.

[19] Gelfand, B.E., Khomik, S.V., Bartenev, A.M., Medvedev, S.P., Grönig, H., and Olivier, H. *Detonation and deflagration initiation at the focusing of shock waves in combustible gaseous mixture.* Shock Waves **10** (2000), 197–204.

[20] Ghias, R., Mittal, R., and Dong, H. *A sharp interface immersed boundary method for compressible viscous flows.* J. Comput. Phys. **225** (2007), 528–553.

[21] Goldberg, M. and Tadmor, E. *Scheme-independent stability criteria for difference approximations of hyperbolic initial-boundary value problems. I.* Math. Comp. **32** (1978), 1097–1107.

[22] Goldberg, M. and Tadmor, E. *Scheme-independent stability criteria for difference approximations of hyperbolic initial-boundary value problems. II.* Math. Comp. **36** (1981), 603–626.

[23] Gottlieb, S., Shu, C.-W., and Tadmor, E. *Strong stability-preserving high-order time discretization methods.* SIAM Rev. **43** (2001), 89–112.

[24] Guo, C., Zhang, D., and Xie, W. *The Mach reflection of a detonation based on soot track measurements.* Combust. Flame **127** (2001), 2051–2058.

[25] Gustafsson, B., Kreiss, H.-O., and Oliger, J. *Time Dependent Problems and Difference Methods.* Wiley-Interscience, New York, 1996.

[26] Gustafsson, B., Kreiss, H.-O., and Sundström, A. *Stability theory of difference approximations for mixed initial boundary value problems. II.* Math. Comp. **26** (1972), 649–686.

[27] Harten, A. *High resolution schemes for hyperbolic conservation laws.* J. Comput. Phys. **49** (1983), 357–393.

[28] Harten, A., Engquist, B., Osher, S., and Chakravarthy, S.R. *Uniformly high order accurate essentially non-oscillatory schemes, III.* J. Comput. Phys. **71** (1987), 231–303.

[29] Helzel, C., Berger, M.J., and LeVeque, R.J. *A high-resolution rotated grid method for conservation laws with embedded geometries.* SIAM J. Sci. Comput. **26** (2005), 785–809.

[30] Hu, X.Y., Khoo, B.C., Adams, N.A., and Huang, F.L. *A conservative interface method for compressible flows.* J. Comput. Phys. **219** (2006), 553–578.

[31] Huang, L., Shu, C.-W., and Zhang, M. *Numerical boundary conditions for the fast sweeping high order WENO methods for solving the Eikonal equation.* J. Comput. Math. **26** (2008), 336–346.

[32] Jerome, J.W. *Analysis of charge transport: A mathematical study of semiconductor devices.* Springer, Berlin, 1996.

[33] Jiang, G.-S. and Shu, C.-W. *Efficient implementation of weighted ENO schemes.* J. Comput. Phys. **126** (1996), 202–228.

[34] Kreiss, H.-O. and Petersson, N.A. *A second order accurate embedded boundary method for the wave equation with Dirichlet data.* SIAM J. Sci. Comput. **27** (2006), 1141–1167.

[35] Kreiss, H.-O., Petersson, N.A., and Ystrom, J. *Difference approximations for the second order wave equation.* SIAM J. Numer. Anal. **40** (2002), 1940–1967.

[36] Kreiss, H.-O., Petersson, N.A., and Ystrom, J. *Difference approximations of the Neumann problem for the second order wave equation.* SIAM J. Numer. Anal. **42** (2004), 1292–1323.

[37] Krivodonova, L. and Berger, M. *High-order accurate implementation of solid wall boundary conditions in curved geometries.* J. Comput. Phys. **211** (2006), 492–512.

[38] Lax, P.D. and Wendroff, B. *Systems of conservation laws.* Comm. Pure Appl. Math. **13** (1960), 217–237.

[39] LeVeque, R.J. and Calhoun, D. *Cartesian grid methods for fluid flow in complex geometries.* In: Computational Modeling in Biological Fluid Dynamics, Fauci, L.J. and Gueron, S. (Eds.), IMA Vol. Math. Appl., vol. 124, Springer, New York, 2001, pp. 117–143.

[40] LeVeque, R.J. and Li, Z. *The immersed interface method for elliptic equations with discontinuous coefficients and singular sources.* SIAM J. Numer. Anal. **31** (1994), 1019–1044.

[41] LeVeque, R.J. and Li, Z. *Immersed interface methods for Stokes flow with elastic boundaries or surface tensions.* SIAM J. Sci. Comput. **18** (1997), 709–735.

[42] Liepmann, H.W. and Roshko, A. *Elements of Gasdynamics.* John Wiley & Sons, New York, 1957, 62–79.

[43] Liu, X.-D., Osher, S., and Chan, T. *Weighted essentially non-oscillatory schemes.* J. Comput. Phys. **115** (1994), 200–212.

[44] Lombard, B., Piraux, J., Gélis, C., and Virieux, J. *Free and smooth boundaries in 2-D finite-difference schemes for transient elastic waves.* Geophys. J. Int. **172** (2008), 252–261.

[45] Mayer, A.C., Scully, S.R., Hardin, B.E., Rowell, M.W., and McGehee, M.D. *Polymer-based solar cells.* Materials Today **10** (2007), 28–33.

[46] Mittal, R. and Iaccarino, G. *Immersed boundary methods.* Annu. Rev. Fluid Mech. **37** (2005), 239–261.

[47] Moretti, G. *Importance of boundary conditions in the numerical treatment of hyperbolic equations.* Phys. Fluids **12** (1969), II 13–20.

[48] Murman, S.M., Aftosmis, M.J., and Berger, M.J. *Implicit approaches for moving boundaries in a 3-D Cartesian method.* AIAA Paper No. 2003-1119, 2003.

[49] Ohyagi, S., Obara, T., Nakata, F., and Hoshi, S. *A numerical simulation of reflection processes of a detonation wave on a wedge.* Shock Waves **10** (2000), 185–190.

[50] Peskin, C.S. *Flow patterns around the heart valves.* J. Comput. Phys. **10** (1972), 252–271.

[51] Qiu, J. and Shu, C.-W. *Finite difference WENO schemes with Lax–Wendroff-type time discretizations.* SIAM J. Sci. Comput. **24** (2003), 2185–2198.

[52] Roe, P. *Approximate Riemann solvers, parameter vectors and difference schemes.* J. Comput. Phys. **27** (1978), 1–31.

[53] Scott, J.C. and Malliaras, G.G. *Charge injection and recombination at the metal-organic interface.* Chem. Phys. Lett. **299** (1999), 115–119.

[54] Sebastian, K. and Shu, C.-W. *Multidomain WENO finite difference method with interpolation at subdomain interfaces.* J. Sci. Comput. **19** (2003), 405–438.

[55] Servaites, J.D., Ratner, M.A., and Marks T.J. *Practical efficiency limits in organic photovoltaic cells: Functional dependence of fill factor and external quantum efficiency.* Appl. Phys. Lett. **95** (2009), art. no. 163302.

[56] Sharpe, G.J. and Falle, S.A.E.G. *Two-dimensional numerical simulations of idealized detonations.* Philos. Trans. R. Soc. Lond. Ser. A Math. Phys. Eng. Sci. **456** (2000), 2081–2100.

[57] Shi, J., Zhang, Y.-T., and Shu, C.-W. *Resolution of high order WENO schemes for complicated flow structures.* J. Comput. Phys. **186** (2003), 690–696.

[58] Shu, C.-W. *Total-variation-diminishing time discretizations.* SIAM J. Sci. Statist. Comput. **9** (1988), 1073–1084.

[59] Shu, C.-W. *High order weighted essentially non-oscillatory schemes for convection dominated problems.* SIAM Rev. **51** (2009), 82–126.

[60] Shu, C.-W. and Osher, S. *Efficient implementation of essentially non-oscillatory shock-capturing schemes.* J. Comput. Phys. **77** (1988), 439–471.

[61] Shu, C.-W. and Osher, S. *Efficient implementation of essentially non-oscillatory shock capturing schemes, II.* J. Comput. Phys. **83** (1989), 32–78.

[62] Shyue, K.-M. *A moving-boundary tracking algorithm for inviscid compressible flow.* In: Hyperbolic Problems: Theory, Numerics, Applications, Benzoni-Gavage, S. and Serre, D. (Eds.), Springer, Berlin Heidelberg, 2008, pp. 989–996.

[63] Sjögreen, B. and Petersson, N.A. *A Cartesian embedded boundary method for hyperbolic conservation laws.* Commun. Comput. Phys. **2** (2007), 1199–1219.

[64] Tan, S. and Shu, C.-W. *Inverse Lax-Wendroff procedure for numerical boundary conditions of conservation laws.* J. Comput. Phys. **229** (2010), 8144–8166.

[65] Tan, S. and Shu, C.-W. *A high order moving boundary treatment for compressible inviscid flows.* J. Comput. Phys. **230** (2011), 6023–6036.

[66] Thomas, G.O. and Williams, R.Ll. *Detonation interaction with wedges and bends.* Shock Waves **11** (2002), 481–492.

[67] van Leer, B. *Towards the ultimate conservative difference scheme V. A second order sequel to Godunov's method.* J. Comput. Phys. **32** (1979), 101–136.

[68] Wang, G., Zhang, D., Liu, K., and Wang, J. *An improved CE/SE scheme for numerical simulation of gaseous and two-phase detonations.* Comput. & Fluids **39** (2010), 168–177.

[69] Woodward, P. and Colella, P. *The numerical simulation of two-dimensional fluid flow with strong shocks.* J. Comput. Phys. **54** (1984), 115–173.

[70] Xiong, T., Zhang, M., Zhang, Y.-T., and Shu, C.-W. *Fifth order fast sweeping WENO scheme for static Hamilton-Jacobi equations with accurate boundary treatment.* J. Sci. Comput. **45** (2010), 514–536.

[71] Zhang, Y.-T., Chen, S., Li, F., Zhao, H., and Shu, C.-W. *Uniformly accurate discontinuous Galerkin fast sweeping methods for Eikonal equations.* SIAM J. Sci. Comput. **33** (2011), 1873–1896.

[72] Zhang, Z.-C., Yu, S.T.J., He, H., and Chang, S.-C. *Direct calculations of two- and three- dimensional detonations by an extended CE/SE method.* AIAA Paper No. 2001–0476, 2001.